

# Luminescent Colloidal Semiconductor Nanocrystals

## Containing Copper:

### Synthesis, Photophysics, and Applications

Kathryn E. Knowles,\* Kimberly H. Hartstein, Troy B. Kilburn, Arianna Marchioro, Heidi D.

Nelson, Patrick J. Whitham, and Daniel R. Gamelin\*

*Department of Chemistry, University of Washington, Seattle, WA 98195-1700*

Email: kknow18@uw.edu, [gamelin@chem.washington.edu](mailto:gamelin@chem.washington.edu)

---

**Abstract.** Copper-doped semiconductors are classic phosphor materials that have been used in a variety of applications for many decades. Colloidal copper-doped semiconductor nanocrystals have recently attracted a great deal of interest because they combine the solution processability and spectral tunability of colloidal nanocrystals with the unique photoluminescence properties of copper-doped semiconductor phosphors. Although ternary and quaternary semiconductors containing copper, such as  $\text{CuInS}_2$  and  $\text{Cu}_2\text{ZnSnS}_4$ , have been studied primarily in the context of their photovoltaic applications, when synthesized as colloidal nanocrystals, these materials have photoluminescence properties that are remarkably similar to those of copper-doped semiconductor nanocrystals. This review focuses on the luminescent properties of colloidal copper-doped, copper-based, and related copper-containing semiconductor nanocrystals. Fundamental investigations into the luminescence of copper-containing colloidal nanocrystals are reviewed in the context of the well-established luminescence mechanisms of bulk copper-doped semiconductors and copper(I) molecular coordination complexes. The use of colloidal copper-containing nanocrystals in applications that take advantage of their luminescent properties, such as bio-imaging, solid-state lighting, and luminescent solar concentrators, is also discussed.

---

## Contents

1. Introduction	3
2. Synthesis and Structural Characterization of Colloidal Copper-Containing Nanocrystals	9
2.1. Size and Composition Dependence of Copper-Centered Photoluminescence	11
2.2. Concentration of Copper Dopants	19
2.3. Copper-Based Semiconductor Nanocrystals	23
2.4. Copper Oxidation State	27
3. Redox Properties	34
4. Photophysics	40
4.1. Charge-Transfer Nature of the Luminescent Excited State	40
4.2. Origin of the Broad Photoluminescence Bandshape and Large Stokes Shift	46
4.3. Mechanism of Photoluminescence in CuInS <sub>2</sub> Nanocrystals	50
4.4. The Roles of Trap States	57
5. Applications	62
5.1. Bio-Imaging	63
5.2. Light-Emitting Diodes	65
5.3. Luminescent Solar Concentrators	67
6. Outlook	72
Acknowledgments	72
Abbreviations	73
References	75
Biographies	89

## 1. Introduction

Luminescent copper-doped semiconductors played a central role in the emergence of 20th-century lighting and display technologies. In particular,  $\text{Cu}^+$ -activated ZnS and related  $\text{Cu}^+$ -containing semiconductors have been employed as integral components of many black-and-white and color display technologies, including in oscilloscopes, televisions, and electroluminescent devices. Decades of industrial and academic research dating back to the late 19th century have yielded a sophisticated understanding of the chemical, spectroscopic, physical, and electrical properties of this class of materials, culminating in their broad technological adoption.<sup>1</sup>

Several types of luminescence are observed in bulk copper-activated ZnS and related semiconductors (Figure 1D). The specific luminescence feature that is observed depends primarily on the ratio of activator ( $\text{Cu}^+$ ) to charge-compensating co-activator (*e.g.*,  $\text{Al}^{3+}$ ,  $\text{Cl}^-$ ) ions,<sup>2,3</sup> both of which are believed to be randomly distributed over substitutional lattice sites. The important luminescence in  $\text{Cu}^+$ -activated ZnS for practical applications is the so-called copper "green" (or "G-Cu") luminescence, which occurs when  $\text{Cu}^+$  and co-activator concentrations are nearly equal.<sup>3-5</sup> Although analogous G-Cu luminescence is observed with different colors in  $\text{Cu}^+$ -doped semiconductors of different compositions,<sup>4,6</sup> it is still commonly referred to by the G-Cu name given to it in  $\text{Cu}^+$ -doped ZnS. Excitation spectra for the G-Cu photoluminescence (PL) in  $\text{Cu}^+:\text{ZnS}$  show two bands.<sup>7</sup> One band ( $\sim 330$  nm) corresponds to the ZnS fundamental absorption edge and indicates that excitation of the host lattice efficiently sensitizes the G-Cu PL. The other band ( $\sim 375$  nm) is a weaker sub-bandgap feature that corresponds to direct donor-type photoionization of  $\text{Cu}^+$ . Assignment of the G-Cu luminescence as involving recombination of a co-activator-bound electron with the ionized copper, *i.e.*, a donor-acceptor pair (DAP) recombination, was established in the early 1950s.<sup>8,9</sup> Strong electron-phonon coupling at the copper dopants makes the G-Cu PL

much broader than the host's band-edge emission. In addition, contributions from many DAPs with different intra-pair distances or donor-electron binding energies causes further inhomogeneity in both the luminescence bandshape and the luminescence decay time.<sup>10,11</sup> The latter can exceed minutes in bulk and is responsible for the characteristic afterglow associated with these phosphors.<sup>12,13</sup> Color tunability for device applications has been achieved *via* cation alloying,<sup>1</sup> for example in the  $\text{Cu}^+, \text{Cl}^- : \text{Zn}_{1-x}\text{Cd}_x\text{S}$  composition series.<sup>14</sup> The very high efficiency of the G-Cu luminescence from DAP recombination in  $\text{Cu}^+$ -doped semiconductor phosphors motivated the wide application of this class of materials in cathode-ray tubes and powder-type AC electroluminescent devices.<sup>1</sup>

In recent years, tremendous advances in synthesis and materials characterization have enabled development of entirely new forms of these phosphor materials with crystallite dimensions now on the nanometer rather than micrometer length scale. Innovations in materials development often stimulate technological advances, and with exquisite control over nanocrystal (NC) size, shape, composition, hetero-interfacing, and surface chemistry, these fundamental research advances are motivating researchers to seek new applications for these classic phosphors. Many of these new applications may simply capitalize on the dispersibility of colloidal semiconductor nanocrystals, which allows solution processing and even liquid-phase applications of these phosphors for the first time, for example in bio-imaging or co-processing with polymers.<sup>15</sup> Other new applications may further exploit changes in electronic structure or photophysics resulting from crystallite size reduction to length scales that rival those of free electrons in these semiconductors, for example in quantum-dot photonics. Along with these attractive opportunities come new challenges associated with doping nanocrystals, characterizing complex nanostructures analytically, and understanding their rich physical properties at a deep fundamental level.

This review focuses on the luminescent properties of colloidal copper-containing semiconductor nanocrystals (NCs). Various parallels are drawn between copper-doped semiconductor NCs, copper-based semiconductor NCs, bulk copper-doped semiconductors, and luminescent molecular copper complexes. For example, Figure 1 compares the luminescence mechanism of copper-doped semiconductor NCs to that of the most common bulk copper-doped semiconductor phosphor,  $\text{Cu}^+, \text{Al}^{3+}:\text{ZnS}$ , and that of tetrahedral  $\text{Cu(I)}$  bis(phenanthroline) complexes. The green and pink shaded areas in Figures 1A-C illustrate the locations of the hole and electron, respectively, in the luminescent excited states of these systems.

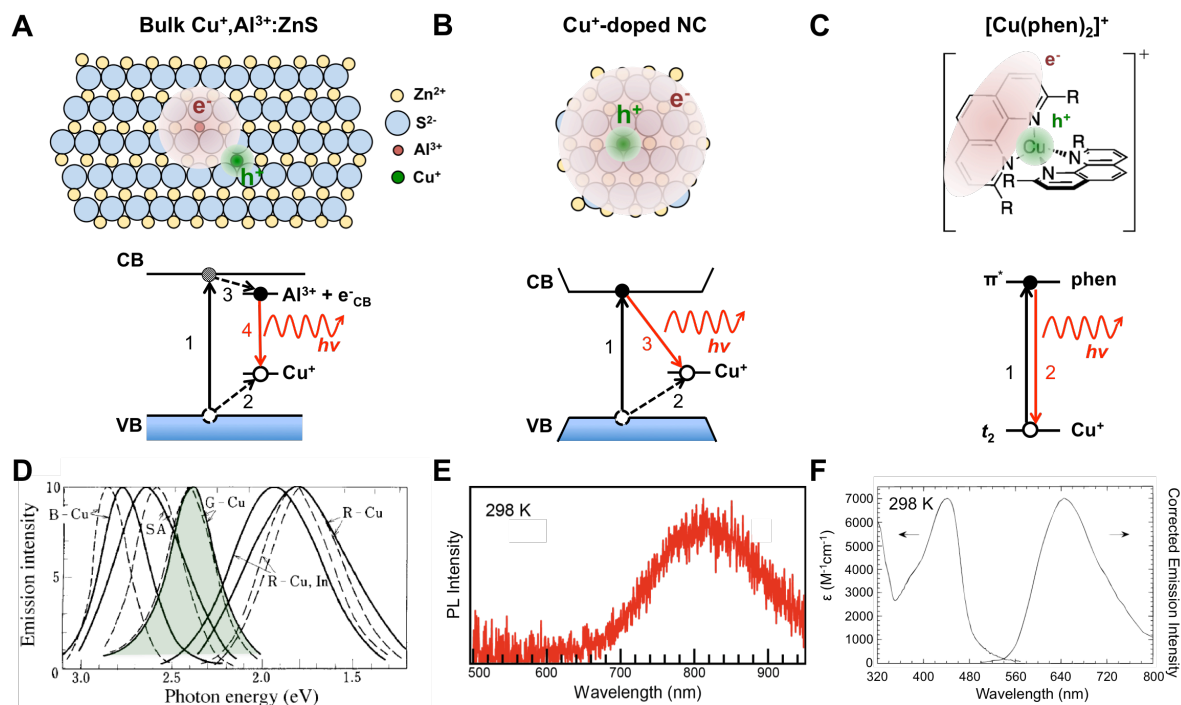


**Figure 1.** Cartoon illustrations of the spatial distribution of charges in the luminescent excited state (top) and orbital energy-level diagrams depicting the luminescence mechanism (middle) for **A)** the G-Cu PL in bulk  $\text{Cu}^+, \text{Al}^{3+}:\text{ZnS}$ , **B)** a colloidal  $\text{Cu}^+$ -doped semiconductor nanocrystal, and **C)** a substituted  $\text{Cu(I)}$  bis(phenanthroline) molecular complex. **D)** PL spectra of several different types of copper-doped bulk ZnS at room temperature (solid lines) and 4.2 K (dashed lines). The spectrum highlighted in green corresponds to the G-Cu-type DAP luminescence from  $\text{Cu}^+, \text{Al}^{3+}:\text{ZnS}$ . Adapted with permission from ref. <sup>5</sup>. Copyright 1964 Physical Society of Japan. **E)** PL spectrum of a single  $\text{Cu}^+$ -doped CdSe nanocrystal measured at room temperature. Adapted with permission from ref. <sup>16</sup>. Copyright 2015 American Chemical Society. **F)** Absorption and

emission spectra of a Cu(I) bis(phenanthroline) complex measured at room temperature. Adapted with permission from ref. <sup>17</sup>. Copyright 1999 American Chemical Society.

As described above, extensive research into the G-Cu luminescence mechanism has demonstrated that photoexcitation of a bulk Cu<sup>+</sup>-containing phosphor (arrow 1 in Figure 1A) leads to deep hole trapping at Cu<sup>+</sup> to form a Cu<sup>2+</sup>-like ion (arrow 2) and partial electron localization around an Al<sup>3+</sup> (or other co-activator) dopant (arrow 3) to form a donor-acceptor pair. Recombination of the electron and hole (arrow 4) produces the classic G-Cu luminescence shown in Figure 1D (shaded green). Figure 1D also shows luminescence spectra from Cu<sup>+</sup>-doped semiconductors containing co-dopants other than Al<sup>3+</sup>, such as Cl<sup>-</sup>, I<sup>-</sup>, or In<sup>3+</sup>, and from materials grown at off-stoichiometries that stabilize other charge-compensating defects.<sup>5</sup> As evident from Figure 1D, the G-Cu DAP luminescence from copper-doped semiconductors is characterized by a broad bandwidth (full-width at half-maximum (fwhm) ~ 300 meV), largely attributable to the strong electron-nuclear coupling of the highly localized hole.<sup>4</sup> For any given donor-acceptor pair, the distance between the donor and acceptor determines the rate of radiative DAP recombination, with smaller donor-acceptor distances leading to faster recombination.<sup>10</sup> Consequently, donor-acceptor pair luminescence in bulk copper-doped phosphors is characterized by non-exponential PL decay due to the distribution in donor-acceptor separations, and can be very slow, with timescales as long as several minutes at 10 K.<sup>12</sup>

In the molecular Cu<sup>+</sup> bis(phenanthroline) complexes represented in Figure 1C, photoexcitation of a metal-to-ligand charge transfer (MLCT) transition (arrow 1) promotes an electron from a Cu<sup>+</sup>(*t*<sub>2</sub>) orbital to a  $\pi^*$  orbital of one of the phenanthroline ligands, formally forming Cu<sup>2+</sup> in the excited state.<sup>17-22</sup> This MLCT excited state undergoes a Jahn-Teller distortion that reduces the molecular symmetry from *D*<sub>2d</sub> to *D*<sub>2</sub> within one picosecond of photoexcitation.<sup>20,23-25</sup> Radiative recombination of the electron on the phenanthroline with the hole on the copper ion (arrow 2)

regenerates the  $\text{Cu}^+$  ground state and produces the MLCT luminescence spectrum shown in Figure 1F. The broad bandshape (fwhm  $\sim 380$  meV) of this luminescence is a direct consequence of the large nuclear reorganization energy associated with the Jahn-Teller distortion of the  $\text{Cu}^{2+}$ -like MLCT excited state.<sup>24,26</sup> Luminescence decay in molecular copper complexes is faster than that in bulk copper-doped phosphors, with single-exponential lifetimes in the range  $\sim 0.05$ - $5$   $\mu\text{s}$ , depending on temperature and, for example, on the phenanthroline substituents (R).<sup>17,21-23</sup>

Figure 1B illustrates the luminescent excited state of a  $\text{Cu}^+$ -doped semiconductor nanocrystal. As in bulk copper-doped phosphors, inter-band photoexcitation (arrow 1) promotes an electron from the valence band (VB) to the conduction band (CB). Rapid localization of the VB hole to the  $\text{Cu}^+$  dopant (arrow 2) produces a  $\text{Cu}^{2+}$ -like ion. This excited state is analogous to the MLCT excited state in the molecular system of Figure 1C, except the nanocrystal CB plays the role of the ligand  $\pi^*$  orbital. We therefore refer to this as a metal-to-ligand (conduction band) charge-transfer ( $\text{ML}_{\text{CBCT}}$ ) excited state. Unlike bulk copper-doped semiconductors, copper-doped semiconductor NCs do not need a donor-like co-dopant to localize the electron near the acceptor because the CB electron is quantum confined and consequently delocalized over the entire nanocrystal volume. This confinement increases the average wavefunction overlap of the electron and the copper-localized hole in copper-doped NCs compared to the bulk phosphors, and the luminescence lifetimes are concomitantly shorter in the NCs ( $\sim 50$ - $500$  ns at room temperature, see Table 1). Also unlike the bulk phosphors,  $\text{Cu}^+$  charge compensation is always facile in the nanocrystals because of the proximity of the nanocrystal surfaces.<sup>27,28</sup> Recombination of the CB electron with the copper-localized hole produces luminescence with a single-particle bandwidth (fwhm  $\sim 350$  meV at 298 K) similar to that observed in both the bulk and molecular systems (Figure 1E).<sup>16</sup>

Table 1 summarizes the basic luminescence properties of several copper-doped and copper-based semiconductor NCs that will be discussed in this review. The entries range from doped semiconductor NCs containing copper at concentrations of a few percent of the total number of cations to quasi-stoichiometric ternary and quaternary copper-based semiconductor NCs. (Although there are also several reports of luminescence from small metallic copper nanoclusters,<sup>29-33</sup> these materials fall beyond the scope of this review and are not considered here.) The data in Table 1 were measured at room temperature, except for the PL energies of  $\text{Cu}_2\text{ZnSn}(\text{S}_{1-x}\text{Se}_x)_4$  NCs, which were measured for a series of samples with various selenium concentrations at 20 K.<sup>34</sup>  $E_{\text{PL}}$  represents the energy of the PL peak associated with copper, and  $E_{\text{abs}}$  is the energy of the first absorption peak of the host nanocrystal. We refer to the quantity  $E_{\text{abs}}-E_{\text{PL}}$  as the “effective Stokes shift” to differentiate it from the true Stokes shift, which describes the energy difference between absorption and PL transitions involving the radiative excited state, *e.g.*, the  $\text{ML}_{\text{CBCT}}$  state in copper-doped NCs. The distinction between “effective” and “true” Stokes shifts in these materials is discussed in more detail in Section 4.2. The data compiled in Table 1 demonstrate that (i)  $E_{\text{PL}}$  and the effective Stokes shift ( $E_{\text{abs}}-E_{\text{PL}}$ ) vary as the composition of the host material changes, and (ii) the fwhm and lifetime of the PL are very similar for all of the materials listed in Table 1, including the ternary and quaternary copper-based materials. This review describes in detail the origins and implications of these general observations in the context of the luminescence mechanism outlined in Figure 1B.

Section 2 briefly reviews the development of syntheses of colloidal copper-containing semiconductor NCs and discusses how these syntheses enabled the discovery of the dependence of  $E_{\text{PL}}$  on nanocrystal size and composition in both copper-doped and copper-based nanocrystals. These observations established the consensus view that the luminescence in copper-doped

nanocrystals occurs *via* recombination of a conduction-band electron with a copper-localized hole. Section 2 ends with a discussion of the oxidation state of copper in the nanocrystal ground state, which determines the nature of the luminescent excited state, and about which there have been conflicting reports. Section 3 describes how the luminescence spectrum of a copper-containing semiconductor nanocrystal changes upon applying a redox perturbation – either by addition of chemical redox reagents or *via* an applied electrochemical potential. Section 4 describes the luminescent excited states in copper-doped and copper-based NCs in more detail, and includes results from density functional theory (DFT), single-particle spectroscopy, temperature-dependent PL measurements, and magnetic circularly polarized luminescence (MCPL) spectroscopy. Finally, Section 5 describes the use of luminescent copper-containing nanocrystals in bio-imaging, light-emitting diodes (LEDs), and luminescent solar concentrators (LSCs).

**Table 1.** Luminescence Properties of Colloidal Copper-Containing Semiconductor Nanocrystals

Host	$E_{\text{PL}}$	$E_{\text{abs}}-E_{\text{PL}}$	PL fwhm	PL lifetime	Ref.
ZnS	2.3-3.0 eV	1.2-2.0 eV	0.4-0.6 eV	54-500 ns	35-41
ZnSe	2.3-2.8 eV	0.6-0.8 eV	0.3-0.5 eV	40-540 ns	41-57
CdS	1.5-2.1 eV	1.2-1.3 eV	0.5-0.6 eV	800-1000 ns	41,58-60
CdSe	1.5-1.8 eV	0.5-0.8 eV	0.3-0.4 eV	300-500 ns	16,41,61-64
CdTe	2.1 eV	0.2 eV	~0.35 eV		41
InP	1.1-1.9 eV	0.7-0.9 eV	0.2-0.4 eV	200-500 ns	64-67
CuInS <sub>2</sub>	1.3-2.5 eV	0.25-0.5 eV	0.3-0.4 eV	100-500 ns	64,68-75
CuInSe <sub>2</sub>	1.3-1.9 eV	0.14-0.18 eV	0.2-0.4 eV		76,77
Cu <sub>2</sub> ZnSn(S <sub>1-x</sub> Se <sub>x</sub> ) <sub>4</sub>	0.9-1.4 eV <sup>a</sup>	~0.1 eV <sup>b</sup>	0.2-0.3 eV <sup>b</sup>		34,78,79

<sup>a</sup>Measured at 20 K

<sup>b</sup>Measured in a PV device

## 2. Synthesis and Structural Characterization of Colloidal Copper-Containing Nanocrystals

Progress in the synthesis of luminescent copper-doped colloidal semiconductor NCs mirrors that in the synthesis of colloidal semiconductor NCs in general. The earliest reports from the mid-1980s through the 1990s describe the synthesis of copper-doped CdS and ZnS colloidal NCs by simply adding small amounts of copper salts to the aqueous-phase arrested precipitation reactions

used to make the undoped nanocrystals.<sup>35,38,39,58,59</sup> More recent approaches use a similar strategy of adding small amounts of copper precursors to hot-injection or heat-up syntheses previously developed for the undoped semiconductor host nanocrystals. In these syntheses, the copper is either present in the reaction mixture when nanocrystal nucleation occurs,<sup>43,46,62,80</sup> or it is added after growth of the host nanocrystals is complete.<sup>41,44,46,48,60,65</sup> The latter method typically involves addition of copper at a temperature lower than that used for growth of the host nanocrystals, followed by extended incubation to allow the copper ions to enter the nanocrystal lattice *via* partial cation exchange. Cluster-seeded heat-up or cluster-thermolysis methods have also been used to synthesize copper-doped semiconductor NCs, specifically copper-doped CdSe NCs.<sup>61,63</sup> Ternary and quaternary copper-based semiconductor NCs such as CuInS<sub>2</sub>, CuInSe<sub>2</sub>, and Cu<sub>2</sub>ZnSn(S<sub>1-x</sub>Se<sub>x</sub>)<sub>4</sub> are typically made by either heat-up<sup>68,69,71,75,81</sup> or hot-injection methods.<sup>70,76,82-84</sup> The heat-up methods involve adding the cation and anion precursors to the same pot and heating to a high temperature to induce nanocrystal nucleation and growth. The hot-injection methods involve rapid injection of anion precursors into a pot containing hot cation precursors, or *vice versa*. The synthesis of CuInS<sub>2</sub> NCs from pre-formed Cu<sub>2-x</sub>S NCs *via* partial cation exchange was recently reported,<sup>85,86</sup> as was a related sequential cation-exchange method used to synthesize CuInSe<sub>2</sub>/CuInS<sub>2</sub> dot-in-rod and CuInTe<sub>2</sub>/CuInSe<sub>2</sub> core/shell NCs from the corresponding CdSe/CdS dot-in-rod and CdTe/CdSe core/shell NCs, respectively.<sup>87</sup>

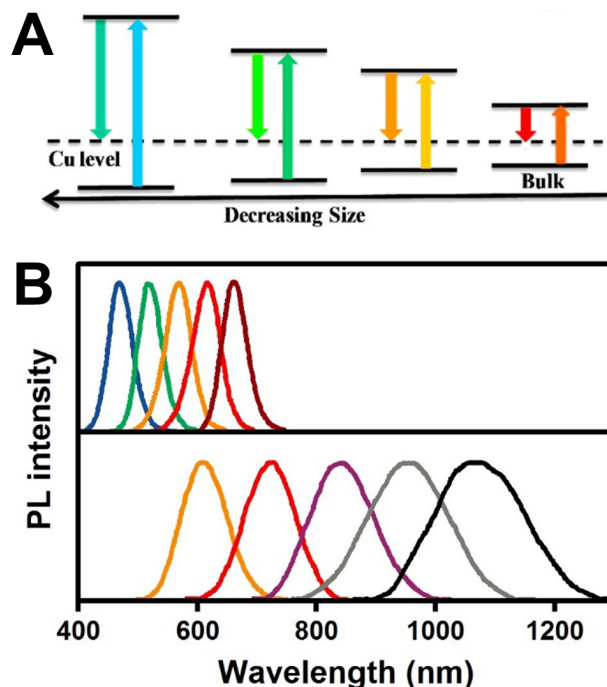
This brief overview overlooks many of the important details of these synthetic methods that enable them to successfully produce copper-doped or copper-containing nanocrystals. These details include tuning the reactivity of the copper precursor relative to the host cation precursor to promote doping, finding the right temperature to enable doping without degradation of the host nanocrystal, and several other subtleties. Exhaustive descriptions of these details are beyond the

scope of this review, and we refer the interested reader to prior reviews that are more focused on related synthetic challenges.<sup>88-93</sup> Here, we instead focus on describing experiments controlling nanocrystal sizes, host compositions, and copper concentrations that have revealed how each of these parameters affects the luminescence of copper-doped semiconductor NCs. Such data, collected for a variety of luminescent copper-doped semiconductor NCs, have ultimately substantiated the assignment of this luminescence to recombination of delocalized conduction-band electrons with copper-localized holes. Analogous experiments on other copper-containing nanocrystals are then discussed in relation to these findings.

### **2.1. Size and Composition Dependence of Copper-Centered Photoluminescence**

The effects of nanocrystal size and composition on the energy of the copper-based luminescence in copper-doped semiconductor NCs support assignment of this luminescence as  $ML_{CBCT}$  recombination of the type illustrated in Figure 1B. As discussed above, this transition involves recombination of an electron from the NC conduction band with a hole localized at a copper dopant. To first order, the energy of the copper acceptor level is pinned relative to vacuum, but the CB energy can be tuned by changing the NC size and composition. The energy-level diagrams in Figure 2A illustrate how the  $ML_{CBCT}$  PL energy is expected to change with NC size:<sup>41</sup> quantum confinement widens the bandgap and raises the CB energy as the NC size decreases, which results in a concomitant increase in the  $ML_{CBCT}$  PL energy. Figure 2B plots PL spectra for undoped InP (top) and  $Cu^+ : InP$  (bottom) NCs of varying sizes.<sup>65</sup> Both the excitonic and copper-based PL peaks shift to higher energies as the NC size decreases, consistent with the proposed  $ML_{CBCT}$  assignment. Notably, the  $Cu^+ : InP$  NC PL is broader and lower in energy than the excitonic PL of similarly sized InP NCs.<sup>65,66</sup> Size-tunability of the copper-based PL energy has

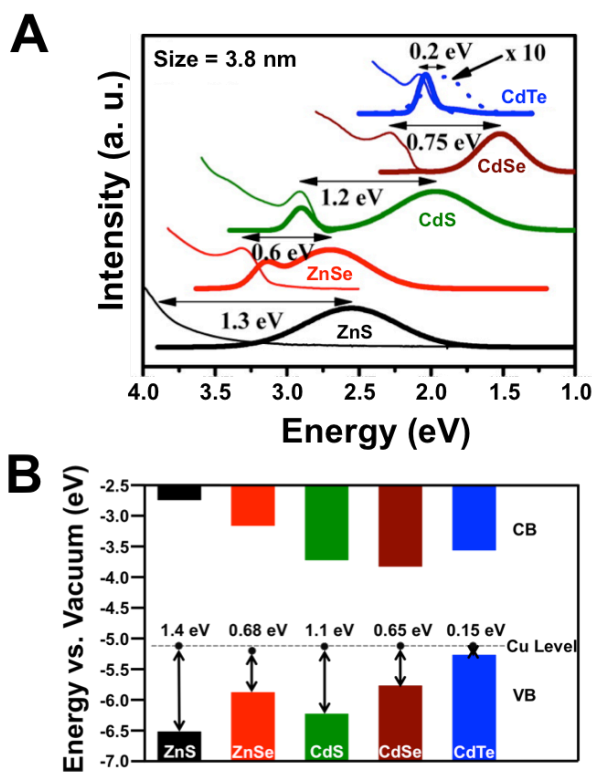
also been demonstrated in several copper-doped II-VI semiconductor NCs, including ZnS,<sup>41,94</sup> ZnSe,<sup>41,44,47,53</sup> CdS,<sup>41,60</sup> CdSe,<sup>41</sup> and CdTe.<sup>41</sup>



**Figure 2.** **A)** Energy-level diagram showing the effect of quantum confinement on excitonic absorption and MLCBCT PL energies in copper-doped NCs. The PL energy is size-dependent because the conduction-band energy increases with decreasing nanocrystal size while the energy of the copper defect level remains relatively constant. Adapted with permission from ref. <sup>41</sup>. Copyright 2012 American Chemical Society. **B)** PL spectra of undoped (top) and copper-doped (bottom) InP NCs of various sizes. Adapted with permission from ref. <sup>65</sup>. Copyright 2009 American Chemical Society.

In addition to changing with NC size, the energies of the CB and VB edges can also be tuned by changing the NC composition, similar to what has been demonstrated in bulk semiconductors.<sup>1,4,14</sup> Comparing the difference in effective Stokes shifts ( $E_{\text{abs}}-E_{\text{PL}}$ ) of different host nanocrystals containing copper dopants provides evidence that the copper acceptor level is indeed approximately pinned relative to vacuum. Figure 3A shows absorption and PL spectra of a series of 3.8-nm diameter II-VI semiconductor NCs doped with copper.<sup>41</sup> The absorption spectra all resemble the spectra of the corresponding undoped NCs, with excitonic transitions that exhibit the

same energy ordering as the bulk bandgaps shown in Figure 3B. The copper-based  $\text{ML}_{\text{CBCT}}$  bands in each PL spectrum are similarly very broad, but the difference in energy between the first excitonic absorption peak and the peak of the  $\text{ML}_{\text{CBCT}}$  PL ( $E_{\text{abs}}-E_{\text{PL}}$ ) depends on the host nanocrystal. The PL spectra for copper-doped ZnSe, CdS, and CdTe each also contain a narrower, high-energy PL peak consistent with excitonic PL, indicating the likely presence of undoped NCs in these samples.



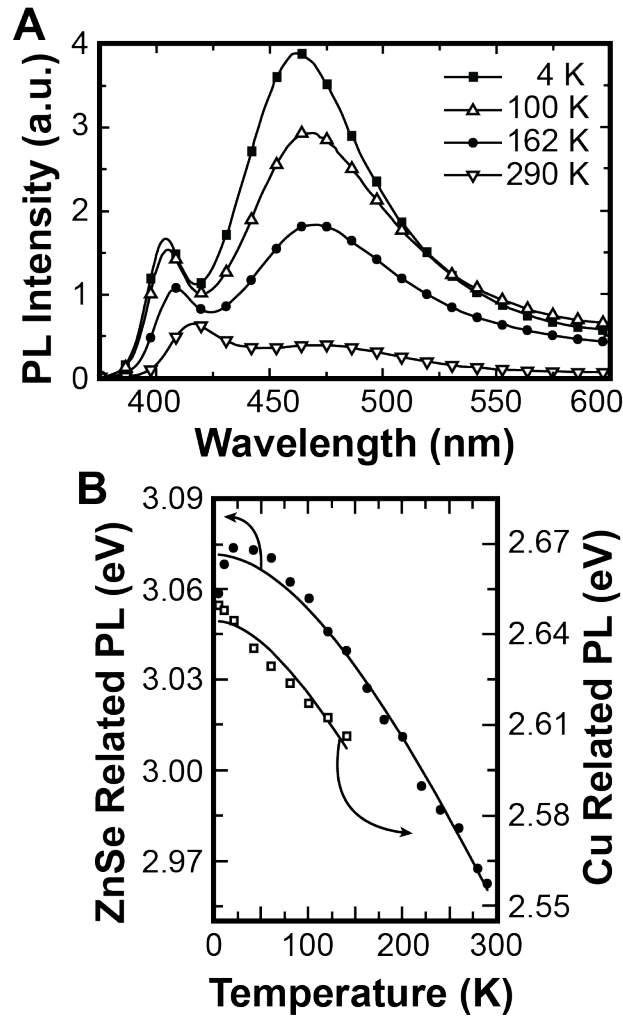
**Figure 3.** A) Absorption and emission spectra of various colloidal copper-doped II-VI semiconductor nanocrystals with  $d = 3.8$  nm. B) Band-edge alignment and copper dopant level relative to vacuum in the corresponding bulk copper-doped II-VI semiconductors. Adapted with permission from ref. <sup>41</sup>. Copyright 2012 American Chemical Society.

Figure 3B shows the bulk band-edge alignment of each of the II-VI nanocrystals shown in Figure 3A, along with a pinned copper acceptor level. This energy-level diagram demonstrates that the effective Stokes shifts shown in Figure 3A match the energy differences between the bulk VB edges and the pinned copper acceptor level fairly well, consistent with the  $\text{ML}_{\text{CBCT}}$  luminescence

mechanism and supporting the assumption of a pinned copper impurity level. DFT calculations suggest minor variations in the absolute energy of the copper acceptor level with NC size and composition due to changes in hybridization between the copper  $3d$  orbitals and the anion  $p$  orbitals that dominate at the VB edge.<sup>95</sup> The influence of such variations in hybridization on the copper-based PL energy is expected to be small relative to the impact of NC size and composition. This interpretation is supported by the PL spectra of alloyed NCs such as  $\text{Zn}_{1-x}\text{Cd}_x\text{S}$ ,<sup>91</sup>  $\text{Zn}_{1-x}\text{Cd}_x\text{Se}$ ,<sup>96</sup>  $\text{Zn-In-Se}$ ,<sup>97</sup> and  $\text{Zn-In-S}$ <sup>98</sup> that have been doped with copper. Tuning the CB energy by alloying alters the energy of the  $\text{ML}_{\text{CBCT}}$  luminescence. For example, the luminescence of  $\text{Cu}^+$ -doped  $\text{Zn-In-S}$  alloyed nanocrystals shifts to lower energy as the CB energy decreases with increasing indium concentration. The resulting samples have emission that is tunable throughout the visible spectrum.<sup>98</sup>

Variable-temperature PL measurements on copper-doped NCs can provide further insight into the nature of the luminescence under investigation. Figure 4 details the temperature dependence of both excitonic and  $\text{ML}_{\text{CBCT}}$  PL features in a sample of copper-doped  $\text{ZnSe}$  NCs.<sup>43</sup> Both features increase in intensity and shift to higher energy with decreasing temperature, as shown in Figure 4A. Figure 4B plots the energies of the peak maxima versus temperature for both emission bands. The solid lines represent fits of these temperature-dependent peak energies to the Varshni equation.<sup>99</sup> Both data sets produce fit parameters similar to those obtained for bulk  $\text{ZnSe}$ . Upon cooling from 300 K to 4 K, the excitonic PL energy increases by 116 meV, and an extrapolation of the Varshni fit yields an increase of  $\sim 92$  meV for the copper-based PL. Given the assignment of the copper-based PL to an  $\text{ML}_{\text{CBCT}}$  transition in which the energy of the copper-bound hole is fixed, this 92 meV shift can be interpreted in terms of the temperature dependence of the conduction-band energy alone. The ratio of the change in conduction-band energy (from the

copper-based PL temperature dependence) to the total bandgap shift (from the excitonic PL temperature dependence) is 0.79. Based on the effective masses of the electron and hole in ZnSe, the expected value for this ratio is  $(m_e^*)^{-1}/[(m_e^*)^{-1} + (m_h^*)^{-1}] \approx 0.82$  in the limit of a deeply localized hole in the luminescent  $ML_{CBCT}$  excited state.<sup>43</sup> The good agreement between these values provides strong support for the  $ML_{CBCT}$  assignment of the copper-based PL.



**Figure 4.** **A)** Temperature-dependent PL spectra of  $r = 3.4$  nm copper-doped ZnSe NCs. **B)** Plot of the energies of the ZnSe excitonic (closed circles) and copper-based (open squares) PL peaks versus temperature. The solid lines represent fits of the data to the Varshni equation. Adapted with permission from ref. <sup>43</sup>. Copyright 2001 American Institute of Physics.

Given luminescence from recombination of a CB electron with a copper-localized hole (Figures 2-4) and the pinning of the copper acceptor level (Figures 3, 4), the change in the position of the  $ML_{CBCT}$  PL with NC size can be used to quantify the change in the CB-edge energy with size for a variety of NC host materials.<sup>41,66</sup> Similarly, the change in the effective Stokes shift of the  $ML_{CBCT}$  PL with size can be used to map out the size-dependence of the VB-edge energy. The closed red circles in Figure 5A plot the size-dependence of the difference between the CB- and VB-edge energies of colloidal copper-doped CdSe NCs and those of bulk CdSe as determined by the positions of the  $ML_{CBCT}$  PL peak and the excitonic absorption peak.<sup>41</sup> The solid black lines represent values predicted from a tight-binding theoretical model<sup>100</sup> and the half-filled circles plot the results of calculations using a many-body pseudo-potential method.<sup>101</sup> The red experimental data have been offset such that the VB energy of the largest NCs matches that predicted by the theoretical calculations. This vertical shift accounts for the absolute energies of the band edges. The experimental variations of the band-edge energies with size agree well with the theoretical predictions and also with experimental trends obtained from X-ray absorption spectroscopy (XAS, open black circles) of undoped CdSe NCs.<sup>102</sup>

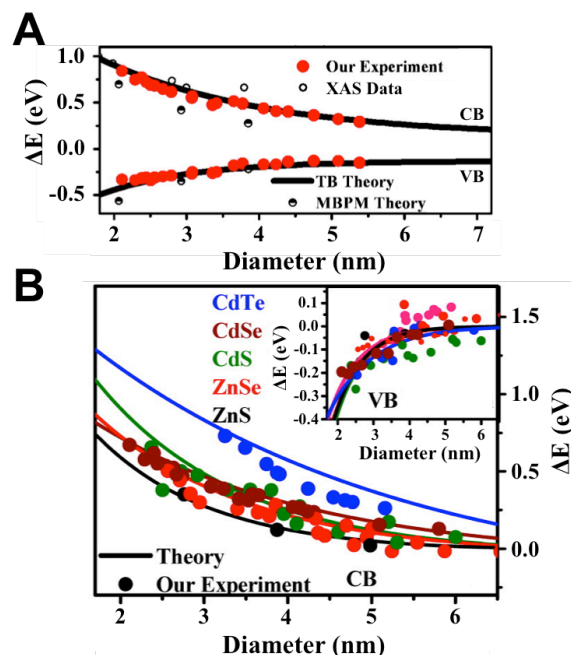


**Figure 5.** **A)** Plot of the difference between the CB- and VB-edge energies of colloidal copper-doped CdSe NCs and those of bulk CdSe versus nanocrystal diameter determined experimentally using the position of the copper PL relative to the optical bandgap (solid red circles) and from X-ray absorption spectroscopy<sup>102</sup> (open black circles). The experimental data are consistent with values predicted from a tight-binding theoretical model<sup>100</sup> (solid black lines) and from a many-body pseudopotential method<sup>101</sup> (half-filled black circles). **B)** Plot of the energies of the CB and VB (inset) edges relative to those predicted for a 9-nm NC versus NC diameter, determined from the position of the copper PL relative to the optical bandgap for copper-doped ZnS (black), ZnSe (red), CdS (green), CdSe (maroon), and CdTe (blue). The solid lines are the results from calculations using a tight-binding model. Adapted with permission from ref. <sup>41</sup>. Copyright 2012 American Chemical Society.

ML<sub>CBCT</sub> PL has also been used to determine the band-edge energies of several other copper-doped II-VI semiconductor NCs and also of copper-doped InP NCs.<sup>41,66</sup> Figure 5B plots the energies of the CB- and VB-edges determined by the position of the ML<sub>CBCT</sub> PL peak and the effective Stokes shift, respectively, versus NC diameter for various copper-doped II-VI semiconductor NCs. The data in Figure 5B are plotted relative to the energies predicted for a  $d = 9$ -nm NC. These data are consistent with results predicted by a tight-binding theoretical model, and demonstrate the general use of ML<sub>CBCT</sub> PL in copper-doped NCs to map out band-edge energies.<sup>41</sup> Furthermore, these data verify experimentally that the size dependence of the VB-edge

energy is roughly the same for all II-VI metal-chalcogenide semiconductor NCs examined here, but the size dependence of the CB-edge energy depends on the material, with CdTe having the steepest size dependence.

The introduction of different co-dopants along with copper offers another mechanism for tuning the PL energy and effective Stokes shift of copper-doped NCs, as well as providing more deliberate charge compensation of  $\text{Cu}^+$  ions (discussed further in Section 2.4).<sup>39,103-108</sup> Figure 6A shows absorption and PL spectra of copper-doped ZnSe NCs containing various  $\text{M}^{3+}$  co-dopants.<sup>107</sup> The undoped ZnSe NCs have a bandgap of 2.97 eV, with excitonic emission centered at 2.84 eV. After copper is introduced into the lattice, the  $\text{ML}_{\text{CBCT}}$  emission peak appears at 2.40 eV. Incorporation of certain aliovalent co-dopants such as  $\text{Ga}^{3+}$  or  $\text{In}^{3+}$  shifts the luminescence to lower energy and increases the luminescence lifetime, attributed to introduction of localized donor states within the bandgap that trap electrons (Figure 6B).<sup>107</sup> These observations suggest that these co-doped NCs luminesce by a DAP mechanism that is closely analogous to that observed in bulk  $\text{Cu}^+$ -doped semiconductors co-doped with  $\text{Al}^{3+}$  or  $\text{In}^{3+}$ .<sup>5,12</sup> DAP luminescence has also been proposed in  $\text{Cu}^+, \text{Br}^-:\text{ZnS}$  NCs<sup>105</sup> and  $\text{Cu}^+, \text{Al}^{3+}:\text{ZnS}$  nanostructures.<sup>103</sup> In contrast with  $\text{Ga}^{3+}$  or  $\text{In}^{3+}$ , the 3s and 3p orbitals of  $\text{Al}^{3+}$  co-dopants are proposed to hybridize with the conduction-band orbitals of the ZnSe NC, rather than form a mid-gap donor state, and thereby shift the energy of the  $\text{ML}_{\text{CBCT}}$  PL to slightly higher energies.<sup>107</sup> The incorporation of  $\text{Al}^{3+}$  co-dopants also improved the PL quantum yield of copper-doped ZnSe NCs.<sup>106</sup> This effect was attributed to the replacement of charge-compensating mid-gap electron traps with  $\text{Al}^{3+}$  co-dopants that provide charge compensation without quenching PL.<sup>106,107</sup> These findings demonstrate the use of co-dopants to tune the luminescence of copper-doped semiconductor NCs.

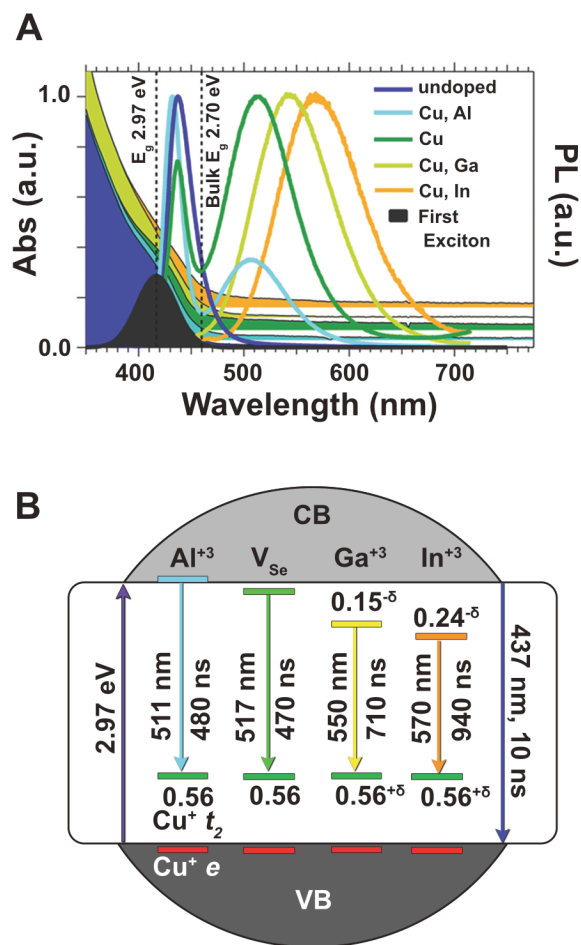


**Figure 6. A)** Absorption and PL spectra of undoped ZnSe nanocrystals and copper-doped ZnSe nanocrystals containing a variety of co-dopants. **B)** Energy-level diagram depicting the luminescence transitions in Cu<sup>+</sup>-doped ZnSe nanocrystals co-doped with Al<sup>3+</sup> (cyan), Ga<sup>3+</sup> (yellow), and In<sup>3+</sup> (orange). The energy of the luminescence depends on the identity of the co-dopant. Adapted with permission from ref. <sup>107</sup>. Copyright 2015 American Chemical Society.

## 2.2. Concentration of Copper Dopants

Figure 7 plots PL spectra of a series of Cu<sup>+</sup>:CdSe nanocrystal samples synthesized by a hot-injection method in which a solution of selenium in trioctylphosphine (TOP) was injected into a mixture of cadmium oleate and copper stearate.<sup>62</sup> The amount of copper stearate used in the reaction increases as the sample number increases from 1 to 7. The spectra show two PL features: a narrow peak centered at ~560 nm corresponding to excitonic emission from undoped CdSe NCs,

and a broad peak centered at  $\sim 780$  nm due to copper-based  $ML_{CBCT}$  emission from  $Cu^+ : CdSe$  NCs. As the amount of copper stearate increases, the excitonic PL intensity decreases and the  $ML_{CBCT}$  PL intensity increases, indicating increased  $Cu^+$  doping and a concomitant decrease in the population of undoped nanocrystals within the ensemble. Quantification of the copper dopant concentrations using the relative excitonic and copper-based PL intensities in Figure 7, assuming a Poisson distribution of copper dopants among the NCs in the ensemble and exclusively copper-based PL from copper-doped NCs, agreed well with direct measurements of the copper concentrations by inductively coupled plasma atomic emission spectroscopy (ICP-AES).<sup>62</sup> This agreement supports association of the higher-energy, excitonic PL peak with a subset of undoped CdSe NCs. Similarly, the intensity of copper PL also increased relative to that of the trap PL associated with undoped ZnS NCs as the copper precursor concentration was increased in the synthesis of copper-doped ZnS NCs.<sup>38</sup>

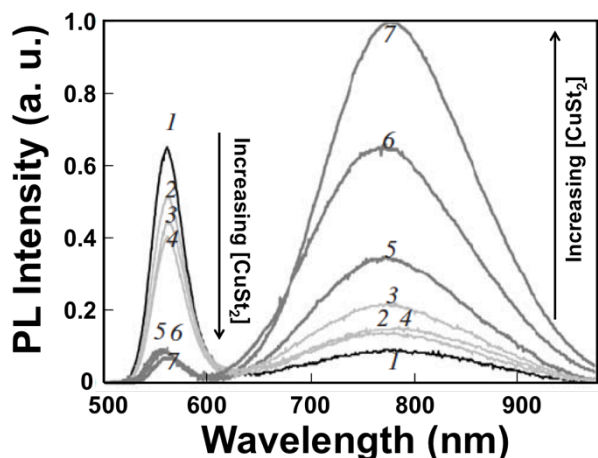


**Figure 7.** PL spectra measured at room temperature of solutions of colloidal  $Cu^+ : CdSe$  NCs made with increasing amounts of copper stearate. The narrow PL peak at  $\sim 560$  nm is due to excitonic recombination from undoped subsets of CdSe NCs, and the broad PL peak centered at  $\sim 780$  nm is the copper-based  $ML_{CBCT}$  PL of copper-doped CdSe NCs. Adapted with permission from ref. <sup>62</sup>. Copyright 2009 Springer.

Reaction time and temperature also determine the extent of copper incorporation, and hence the relative excitonic and  $ML_{CBCT}$  PL intensities. For example, Figure 8A shows the temporal

evolution of the PL spectrum of ZnSe NCs in the presence of copper oleate in octadecene at 40 °C.<sup>46</sup> The feature at ~410 nm corresponds to excitonic PL. The intensity of this feature decreases and reaches a plateau after about 45 min, but the overall bandshape is maintained and ML<sub>CBCT</sub> PL is not observed. When the temperature is raised to 60 °C and the reaction is allowed to run for 100 min, the lower energy ML<sub>CBCT</sub> PL band appears (Figure 8B, dotted red line). Notably, excitonic PL is still observed and remains more intense than the ML<sub>CBCT</sub> PL under these conditions, indicating a significant subset of undoped ZnSe NCs. The relative intensity of the ML<sub>CBCT</sub> PL grows with increasing reaction temperature, dominating the PL spectrum for reactions run at 100 °C. The majority of NCs formed under these reaction conditions are thus doped with copper. Similar effects of reaction temperature and time on final copper concentrations are observed in the syntheses of other copper-doped semiconductor NCs.<sup>65,94</sup>

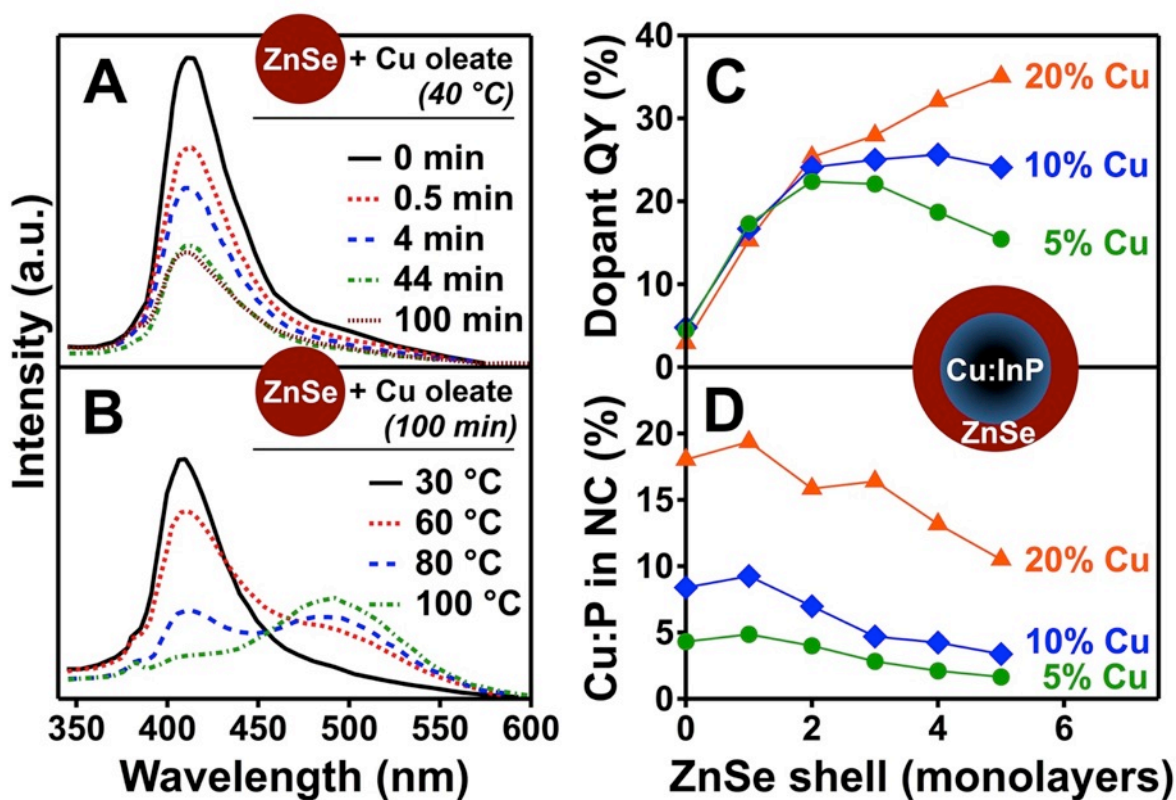


**Figure 8.** **A)** Temporal evolution of the PL spectra of ZnSe NCs upon the addition of copper oleate at 40 °C. **B)** PL spectra of ZnSe NCs after reacting with copper oleate for 100 min at various temperatures. Adapted with permission from ref. <sup>46</sup>. Copyright 2009 American Chemical Society. **C)** MLCBCT PL quantum yield and **D)** copper concentration as determined by EDS of Cu<sup>+</sup>:InP/ZnSe core/shell NCs plotted versus ZnSe shell thickness for Cu:P precursor ratios of 5% (green circles), 10% (blue diamonds), and 20% (orange triangles). Adapted with permission from ref. <sup>65</sup>. Copyright 2009 American Chemical Society.

Similar to many other luminescent semiconductor NCs, epitaxial growth of shells of other semiconductors can mitigate the effects of surface traps and improve the MLCBCT PL quantum yield (QY) in copper-doped semiconductor NCs.<sup>65,107,109</sup> Copper concentrations in the core nanocrystals often decrease during shell growth, however. Figure 8C-D illustrates attempts to grow ZnSe shells on Cu<sup>+</sup>:InP NCs by alternating injections of zinc and selenium precursors followed by thermal cycling.<sup>65</sup> The percentages of copper noted in Figure 8C-D represent the amounts of copper stearate used in the syntheses of the Cu<sup>+</sup>:InP core NCs relative to the phosphorus precursor, which is the limiting reagent in the formation of InP nanocrystals in this particular synthesis.<sup>65,110</sup> As shown in Figure 8C, the first two monolayers of ZnSe shell growth improved the MLCBCT luminescence QY in all cases, but continued shell growth had varying consequences depending on the initial amount of copper precursor. The MLCBCT QY increased through five monolayers of shell growth to reach a maximum of nearly 35% for the sample in which the initial Cu:P ratio was 0.2, whereas it started to decrease after just three monolayers of shell growth for the sample in which the initial Cu:P ratio was 0.05. These observations were supplemented by elemental analysis *via* energy-dispersive spectroscopy (EDS), which indicated copper loss during shell growth (Figure 8D). Similar “self-purification” at elevated temperatures has been suggested for some Mn<sup>2+</sup>-doped NCs.<sup>46,111-113</sup> The extremely high mobility of copper in II-VI and III-V semiconductors facilitates its removal from the NCs during shell growth.<sup>114</sup> Although some copper

loss could not be avoided, the data in Figure 8D show that large amounts of copper in the initial nanocrystal cores allow successful formation of copper-doped core/shell NCs.

In addition to changing the synthesis conditions, some reports describe how addition of excess ligands, such as phosphines or thiols, during or after synthesis of copper-doped semiconductor NCs can change the relative intensities of excitonic and  $ML_{CBCT}$  PL.<sup>41,109</sup> Unlike the study of Figure 7, these reports present a vastly different interpretation. Specifically, the data have been interpreted assuming divalent copper ( $Cu^{2+}$ ) in the nanocrystal ground state, and the presence of both excitonic and  $ML_{CBCT}$  PL is attributed to competition between recombination of a CB electron with a VB hole and with a “permanent” hole on the  $Cu^{2+}$ .<sup>109</sup> In this interpretation, the same NC can thus emit *via* excitonic recombination or  $ML_{CBCT}$  recombination, with the relative probabilities of these two recombination processes controlled by the NC surface ligands. According to this interpretation, addition of phosphines or thiols changes the probability that the VB hole will be trapped by surface states before it has a chance to recombine with the CB electron, thereby changing the ratio of excitonic to  $ML_{CBCT}$  PL. This interpretation hinges on the existence of prominent excitonic luminescence from  $Cu^{2+}$ -doped nanocrystals, however, and therefore merits some skepticism. Scenarios involving the co-existence of undoped and doped NCs within the same ensemble may be more likely given the electronic structures of  $Cu^{2+}$ -doped semiconductors. The properties of copper dopants in different ground-state oxidation states are discussed in more detail in Section 2.4.

### 2.3. Copper-Based Semiconductor Nanocrystals

Colloidal semiconductor nanocrystals that incorporate copper quasi-stoichiometrically, such as  $CuInS_2$  (CIS),  $CuInSe_2$  (CISE),  $Cu_2ZnSnS_4$  (CZTS), and  $Cu_3S$ , in some cases exhibit luminescence spectra with energies or bandshapes that are very similar to those observed in copper-doped

semiconductor nanocrystals (See Table 1). This section compares the optical properties of these copper-based NCs with those of the copper-doped NCs discussed above, with a particular focus on CuInS<sub>2</sub> and Cu<sub>2</sub>ZnSnS<sub>4</sub> NCs. Cu<sub>2</sub>S NCs are discussed briefly in Section 3, and the mechanism of PL in CuInS<sub>2</sub> NCs is discussed in more detail in Section 4.3.

CuInS<sub>2</sub> is a direct-bandgap semiconductor with a bulk bandgap of ~1.5 eV.<sup>115-118</sup> Rapid increases in band-gap energy with decreasing size are observed for CuInS<sub>2</sub> NCs with diameters below ~8 nm,<sup>70,119,120</sup> and a weaker size dependence is reported for diameters between 10 and 16 nm.<sup>70</sup> In general, CuInS<sub>2</sub> NCs exhibit broad, featureless absorption spectra (Figure 9A)<sup>70,88</sup> that contrast with the highly structured absorption spectra of II-VI semiconductor nanocrystals.<sup>121,122</sup> The PL spectra of CuInS<sub>2</sub> NCs are also broad, with reported bandwidths ranging from ~300 to 400 meV (fwhm), and large Stokes shifts that range from ~250 to 500 meV (see Table 1).<sup>68-71,75</sup> As with copper-doped semiconductor NCs, the broad bandshapes and large Stokes shifts are retained throughout the quantum-confined size regime.<sup>69,70,123</sup> Figures 9A and 9B show absorption and PL spectra from a set of CuInS<sub>2</sub> NCs of various sizes ( $d = 2.5$ -16 nm). The energy of the absorption edge ranges from 1.65 to 3.55 eV and the PL peak energy ranges from 1.3 to 2.5 eV.<sup>70</sup> Attempts to narrow the absorption and PL peaks of CuInS<sub>2</sub> NCs through size-selective precipitation have been unsuccessful, prompting the suggestion that inhomogeneity in size distribution is not the primary origin of the broad absorption and emission bands.<sup>70</sup> Additionally, surface treatments that alter the size distributions of CuInS<sub>2</sub> NCs, as measured by transmission electron microscopy (TEM), have been shown to leave the large absorption and PL bandwidths unchanged.<sup>74</sup> The origin of the broad PL bandwidth of CuInS<sub>2</sub> NCs is discussed in Section 4.3. CuInSe<sub>2</sub> NCs have absorption and PL properties that are very similar to those of CuInS<sub>2</sub> NCs, but for a given NC size their absorption and PL spectra are shifted to lower energies,<sup>89,119,124</sup> consistent with the difference in the bulk

bandgaps of these materials<sup>15</sup> and attributable primarily to the higher energy of the VB-edge in CuInSe<sub>2</sub> compared to CuInS<sub>2</sub>.

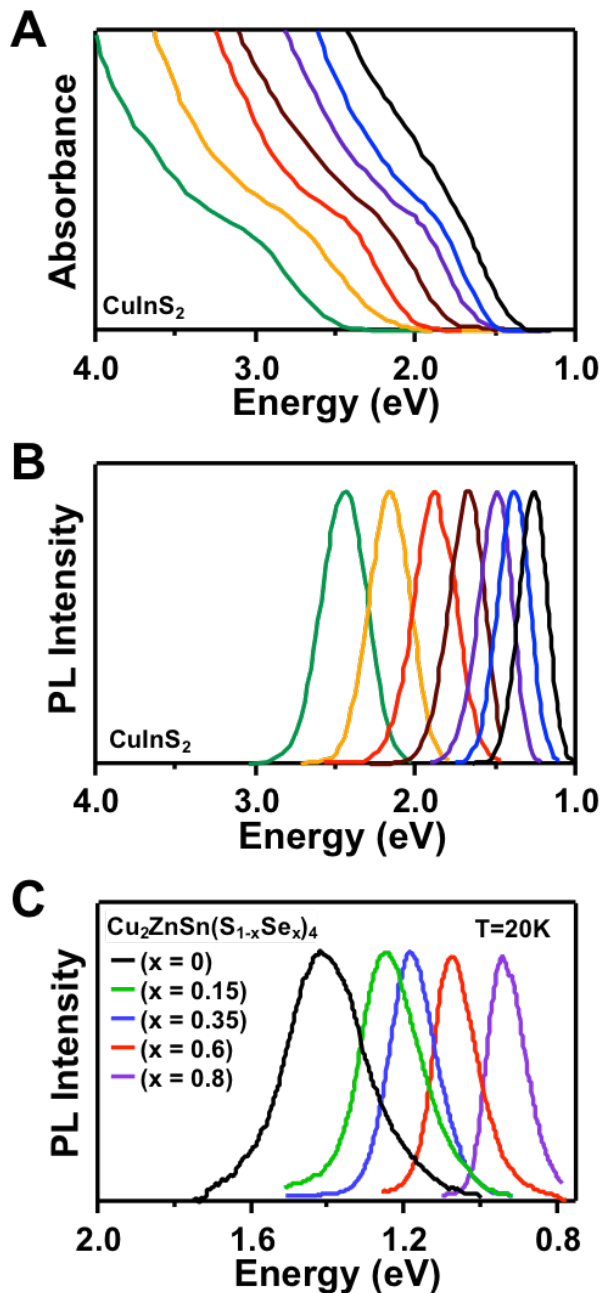


**Figure 9.** Room-temperature A) absorption and B) PL spectra of colloidal CuInS<sub>2</sub> nanocrystals with diameters ranging from ~2.5-16 nm. As the nanocrystal diameter increases, both the absorption onset and PL peak shift to lower energies. Adapted with permission from Ref. <sup>70</sup>. Copyright 2009 American Chemical Society. C) PL spectra of Cu<sub>2</sub>ZnSn(S<sub>1-x</sub>Se<sub>x</sub>)<sub>4</sub> nanocrystals measured at 20 K with values of x ranging from 0 to 0.8.

The broad emission band shifts to lower energy and narrows as the percentage of selenium ( $x$ ) increases. Adapted with permission from Ref. <sup>34</sup>. Copyright 2013 Wiley.

The energy of the PL peak in  $\text{CuInS}_2$  NCs is also somewhat tunable with composition. For copper-deficient  $\text{CuInS}_2$  NCs, the absorption and PL both shift slightly to higher energy as the copper concentration decreases, but retain similar bandshapes.<sup>74,125</sup> This blue-shift has been attributed to lowering of the VB energy upon removal of copper. A red-shift in absorption and PL has been reported for copper-rich  $\text{CuInS}_2$  NCs, but it is unclear from the data whether the NC size remained constant, so the observed red-shift may not be purely due to changes in composition.<sup>126</sup> Interestingly, several groups report that the PL quantum yield is optimized for a copper-deficient  $\text{CuInS}_2$  composition, with the brightest samples having Cu:In ratios from 0.4 to 0.8.<sup>74,125-127</sup> ZnS and CdS shell growth are also found to increase PL QYs in  $\text{CuInS}_2$  NCs.<sup>65,71,128</sup>

The first syntheses of colloidal  $\text{Cu}_2\text{ZnSnS}_4$  NCs yielded NCs with diameters greater than 10 nm, too large to exhibit quantum confinement effects.<sup>81-83</sup>  $\text{Cu}_2\text{ZnSnS}_4$  NCs with diameters below 10 nm were subsequently prepared and quantum confinement effects were observed by absorption spectroscopy at diameters below  $\sim 6$  nm.<sup>84,129-131</sup> Similarly, small  $\text{Cu}_2\text{ZnSnSe}_4$  NCs ( $d \sim 3-4$  nm) also exhibit confinement effects in their absorption spectra.<sup>132</sup> Unlike  $\text{CuInS}_2$  NCs, PL in  $\text{Cu}_2\text{ZnSnS}_4$  NCs is typically very weak, and often is not observed at all.<sup>84,131</sup> Figure 9C shows PL spectra measured at 20 K of  $\text{Cu}_2\text{ZnSn}(\text{S}_{1-x}\text{Se}_x)_4$  nanocrystals prepared by hot injection, with values of  $x$  ranging from 0 to 0.8.<sup>34</sup> As the selenium concentration increases, the PL band shifts to lower energy and becomes narrower. This PL redshift is consistent with previous reports demonstrating a shift of the absorption edge to lower energy with increasing  $\text{Se}^{2-}$  content.<sup>133,134</sup> Despite interest in colloidal  $\text{Cu}_2\text{ZnSnS}_4$  and  $\text{Cu}_2\text{ZnSn}(\text{S}_{1-x}\text{Se}_x)_4$  NCs as potential precursors for solution-processed PVs made of non-toxic and earth-abundant elements, detailed photophysical studies of  $\text{Cu}_2\text{ZnSnS}_4$  and  $\text{Cu}_2\text{ZnSn}(\text{S}_{1-x}\text{Se}_x)_4$  nanocrystals are rather scarce. There are reports of PL from sintered

$\text{Cu}_2\text{ZnSn}(\text{S}_{1-x}\text{Se}_x)_4$  nanocrystal films and  $\text{Cu}_2\text{ZnSn}(\text{S}_{1-x}\text{Se}_x)_4$  solar cells,<sup>78,79,135</sup> but the data in Figure 9C appear to be the only PL spectra of colloidal  $\text{Cu}_2\text{ZnSn}(\text{S}_{1-x}\text{Se}_x)_4$  NCs published to date.

## 2.4. Copper Oxidation State

The literature contains conflicting claims about copper oxidation states in copper-doped semiconductor NCs. Most synthetic procedures use  $\text{Cu}^{2+}$  precursors for copper doping.<sup>39,41,46,59,60,62,65,91</sup> Many groups have suggested that  $\text{Cu}^{2+}$  is reduced to  $\text{Cu}^+$  during nanocrystal synthesis, yielding  $\text{Cu}^+$ -doped nanocrystals as the product.<sup>16,39,59,62,91</sup> Addition of CdS NCs to a solution of a  $\text{Cu}^{2+}$  salt causes a decrease of the electron paramagnetic resonance (EPR) signal associated with  $\text{Cu}^{2+}$ , consistent with reduction of  $\text{Cu}^{2+}$  to  $\text{Cu}^+$  by the CdS NCs,<sup>59</sup> although the microscopic details remain unclear. Most syntheses of copper-doped nanocrystals are also carried out under anaerobic conditions at high temperatures ( $> 200\text{ }^\circ\text{C}$ ) in the presence of electron-rich solvents and ligands, such as olefins, phosphines, and amines, that may be capable of reducing other precursors during the reaction.<sup>41,44,46,60,62,65,91</sup> For example, octadecene, which is perhaps the most common solvent for nanocrystal synthesis, reduces  $\text{SeO}_2$  to  $\text{Se}^{2-}$  at high temperatures in the "heat-up" synthesis of CdSe nanocrystals.<sup>136</sup> Trioctylphosphine, a very common ligand in nanocrystal syntheses, also reacts with copper (II) stearate, which is bright blue, to form a pale yellow product consistent with reduction to  $\text{Cu}^+$ .<sup>62</sup>

These observations provide circumstantial indication that  $\text{Cu}^{2+}$  precursors are likely reduced to  $\text{Cu}^+$  during nanocrystal synthesis, but they do not provide enough evidence to assign the oxidation state of copper in the final copper-doped nanocrystal product. Many reports cite the lack of a  $\text{Cu}^{2+}$  EPR signal when concluding that the dopants are  $\text{Cu}^+$ ,<sup>16,39,48,91,137,138</sup> while others assume that the oxidation state of the  $\text{Cu}^{2+}$  precursors is preserved during the nanocrystal synthesis.<sup>41,47,60,109</sup> Although the absence of a  $\text{Cu}^{2+}$  EPR signal is consistent with copper in its  $\text{Cu}^+$  oxidation state, it is

insufficient to make a definitive assignment. This section compares the optical properties of copper-doped semiconductor NCs to those of  $\text{Cu}^+$ - and  $\text{Cu}^{2+}$ -doped bulk semiconductors and presents data from X-ray measurements on copper-doped NCs to address the copper oxidation state in copper-doped semiconductor NCs.

$\text{Cu}^+$  and  $\text{Cu}^{2+}$  can both act as luminescence activators in bulk II-VI semiconductors, but their different electronic structures result in very different absorption and luminescence spectra. Figure 10 summarizes key spectroscopic differences between  $\text{Cu}^+$ - and  $\text{Cu}^{2+}$ -doped ZnS (bulk). Figure 10A shows PL spectra of  $\text{Cu}^+, \text{Al}^{3+}:\text{ZnS}$  measured at different temperatures between 4 and 373 K.<sup>5</sup> The G-Cu PL is observed, centered at  $\sim 2.4$  eV. Figure 10B shows absorption and PL spectra of  $\text{Cu}^{2+}$ -doped ZnS (bulk) measured at 4.2 and 4.8 K, respectively.<sup>139</sup> In contrast with  $\text{Cu}^+$  in ZnS,  $\text{Cu}^{2+}$  dopants do not produce any luminescence in the visible range and instead show only near-infrared (NIR) luminescence centered at  $\sim 0.75$  eV. This NIR luminescence originates from transitions within the  $3d$  shell of the  $\text{Cu}^{2+}$  ion. The  $\text{Cu}^{2+}(3d)$  orbitals are split by the tetrahedral crystal field of the host semiconductor to form a lower-energy doubly degenerate  $e$  set and a higher-energy triply degenerate  $t_2$  set. In the ground-state  $3d^9$  configuration, the unpaired electron resides in the  $t_2$  orbital set, forming a  ${}^2T_2$  ground state. The absorption spectrum in Figure 10B arises from promotion of an  $e$  electron to the  $t_2$  set to form a  ${}^2E$  excited state, and the luminescence comes from the corresponding radiative  ${}^2E \rightarrow {}^2T_2$  relaxation. Spin-orbit splittings within the  ${}^2T_2$  and  ${}^2E$  terms and vibronic coupling combine to produce the rich structure shown in Figure 10B. This fine structure has been analyzed to yield a deep understanding of the electronic structure of  $\text{Cu}^{2+}$  in II-VI semiconductor lattices, including detailed descriptions of Jahn-Teller, spin-orbit, and Zeeman splittings of this NIR luminescence.<sup>139-142</sup>

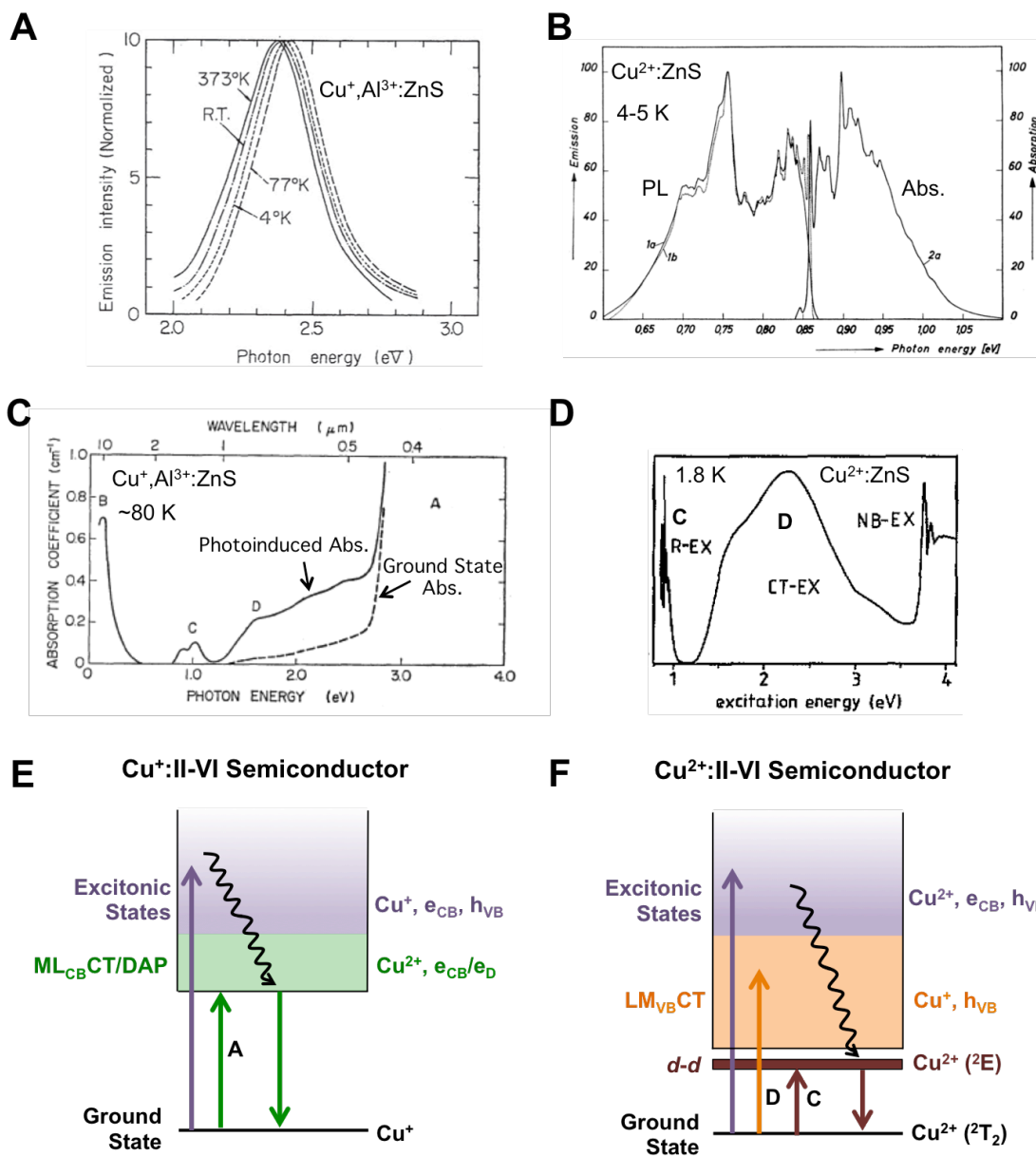


**Figure 10.** **A)** PL spectra of  $\text{Cu}^+, \text{Al}^{3+}:\text{ZnS}$  (bulk) measured at temperatures from 4 to 373 K. Adapted with permission from ref. <sup>5</sup>. Copyright 1964 Physical Society of Japan. **B)** Absorption (right) and PL (left) spectra of  $\text{Cu}^{2+}:\text{ZnS}$  (bulk) measured at 4.8 K and 4.2 K, respectively. The solid and dotted lines represent data collected from two different samples. The luminescence intensity maximum occurs at  $\sim 0.75$  eV. Adapted with permission from ref. <sup>139</sup>. Copyright 1965 American Physical Society. **C)** Ground-state (dashed line) and photoinduced (solid line) absorption spectra of  $\text{Cu}^+, \text{Al}^{3+}:\text{ZnS}$  (bulk), measured at liquid nitrogen temperature. Adapted with permission from ref. <sup>12</sup>. Copyright 1971 Physical Society of Japan. **D)** Photoluminescence excitation spectrum of the near-infrared  $\text{Cu}^{2+}:\text{ZnS}$  luminescence shown in (B), measured at 1.8 K. The peaks labeled C and D correspond to the same transitions labeled C and D in the photoinduced absorption spectrum shown in (C). Adapted with permission from ref. <sup>143</sup>. Copyright 1992 IOP Publishing. **E, F)** State

diagrams illustrating the absorption and photoluminescence transitions shown in (A-D) for  $\text{Cu}^+, \text{Al}^{3+}:\text{ZnS}$  (E) and  $\text{Cu}^{2+}:\text{ZnS}$  (F). The black curly arrows illustrate nonradiative decay from the initially prepared excited state to the luminescent excited state. The absorption transitions labeled A, C, and D correspond to the spectroscopic features with the same labels in (C) and (D).

In bulk  $\text{Cu}^+$ -doped phosphors, the existence of very slow DAP recombination enables the measurement, on slow timescales, of the absorption spectrum of the metastable charge-separated (DAP) state formed upon photoexcitation. Figure 10C shows ground-state (dashed line) and photoinduced (solid line) absorption spectra of  $\text{Cu}^+, \text{Al}^{3+}:\text{ZnS}$  (bulk) measured at  $\sim 80$  K.<sup>12</sup> The ground-state absorption spectrum is dominated by the "characteristic"  $\text{ML}_{\text{CBCT}}$  band, which corresponds to promotion of an electron from  $\text{Cu}^+$  to the conduction band (transition A). The photoinduced absorption spectrum contains the same  $d-d$  transitions characteristic of  $\text{Cu}^{2+}$  shown in Figure 10B (transition C), and also reveals broad charge-transfer absorption corresponding to excitation of VB electrons to fill the copper-localized hole (ligand-(VB)-to-metal charge transfer,  $\text{L}_{\text{VB}}\text{MCT}$ , transition D). The sharp feature at  $\sim 0.1$  eV (transition B) in the photoinduced absorption spectrum has been assigned to excitation of shallow  $\text{Al}^{3+}$ -bound electrons into the conduction band. These spectra clearly demonstrate that  $\text{Cu}^{2+}$  ions form upon photoexcitation of  $\text{Cu}^+, \text{Al}^{3+}:\text{ZnS}$ . DFT calculations on  $\text{Cu}^+$ - and  $\text{Cu}^{2+}$ -doped CdSe NCs predict absorption spectra for these two oxidation states that are similar to the ground-state and photoinduced absorption spectra of Figure 10C, respectively.<sup>95</sup>

Figure 10D shows a photoluminescence excitation (PLE) spectrum measured at 1.8 K for the near-infrared  $\text{Cu}^{2+}$  luminescence shown in Figure 10B.<sup>143</sup> This excitation spectrum contains the same  $d-d$  and  $\text{L}_{\text{VB}}\text{MCT}$  features shown in the photoinduced absorption spectrum of Figure 10C (labeled C and D, respectively), as well as a feature associated with excitation across the bandgap

(NB-EX). This PLE spectrum demonstrates that inter-band excitation in  $\text{Cu}^{2+}$ -doped ZnS leads to rapid nonradiative internal conversion followed by near-infrared  $d-d$  luminescence.

Figures 10E and 10F show qualitative state diagrams illustrating the absorption and PL transitions summarized in Figures 10A-D for  $\text{Cu}^+$  and  $\text{Cu}^{2+}$  dopants in bulk ZnS, respectively. For  $\text{Cu}^+$ -doped ZnS, excitonic (10E, purple arrow) or  $\text{ML}_{\text{CBCT}}$  (10E, green arrow) excitation formally ionizes  $\text{Cu}^+$  to form a  $\text{Cu}^{2+}$ -like ion, which exhibits the characteristic  $\text{Cu}^{2+}$   $d-d$  (10F, maroon arrow) and  $\text{L}_{\text{VBMCT}}$  (10F, orange arrow) absorptions shown in Figure 10C for the duration of the charge separation. Recombination of an electron from the conduction band ( $e_{\text{CB}}$ ) or a shallow donor state ( $e_{\text{D}}$ ) with this  $\text{Cu}^{2+}$  ion produces the G-Cu PL (10E, green arrow) shown in Figure 10A, and regenerates the  $\text{Cu}^+$  ground state. For  $\text{Cu}^{2+}$ -doped ZnS, excitonic (10F, purple arrow) or  $\text{L}_{\text{VBMCT}}$  (10F, orange arrow) excitation leads to nonradiative relaxation through the broad manifold of  $\text{L}_{\text{VBMCT}}$  excited states to populate the lowest energy  ${}^2\text{E}$  ( $3d^9$ ) ligand-field excited state of  $\text{Cu}^{2+}$ , which produces the near-infrared  $d-d$  luminescence (10F, maroon arrow) shown in Figure 10B. Importantly, the large density of  $\text{L}_{\text{VBMCT}}$  excited states, which directly reflects the valence-band density of states, facilitates rapid nonradiative internal conversion to the  ${}^2\text{E}$  ( $3d^9$ )  $\text{Cu}^{2+}$  excited state and precludes luminescence from excited states with higher energies. Very similar spectroscopy has been reported for  $\text{Cu}^+$ - and  $\text{Cu}^{2+}$ -doped CdS (bulk),<sup>139,143</sup> and the above description appears to be generally applicable to other chalcogenide lattices,<sup>4</sup> bearing in mind that for some chalcogenides the  $\text{L}_{\text{VBMCT}}$  excited states may actually extend to energies lower than the  $d-d$  excited states. In part because of its very deep VB edge,  $\text{Cu}^{2+}$ -doped ZnO is unique among II-VI semiconductors in that it shows  $\text{L}_{\text{VBMCT}}$  (transient shallow acceptor) luminescence in addition to  $d-d$  luminescence.<sup>143,144</sup>

The luminescence of copper-doped semiconductor NCs resembles the broad, visible G-Cu-type  $ML_{CBCT}$  luminescence of the corresponding  $Cu^+$ -doped bulk semiconductors. Near-infrared luminescence arising from  $d-d$  transitions of  $Cu^{2+}$  has not been reported for any copper-doped NCs. Furthermore, the near-infrared  $d-d$  and  $L_{VB}MCT$  transitions associated with ground-state  $Cu^{2+}$  should be readily detectable by absorption and particularly magnetic circular dichroism (MCD) spectroscopies, but near-infrared and visible MCD spectra of copper-doped NCs show no sign of either of these transitions.<sup>16,64</sup> The optical properties of copper-doped NCs are therefore consistent with the presence of  $Cu^+$  ions in the ground state. The above comparisons furthermore suggest that the electronic structures of  $Cu^{2+}$ -doped chalcogenide semiconductor NCs preclude the observation of long-lived excitonic PL from such NCs.

Beyond optical spectroscopies, the copper oxidation states in various semiconductor NCs have been probed by X-ray absorption and X-ray photoelectron spectroscopies.<sup>42,61,63,106,138,145</sup> These measurements universally support assignment of a  $Cu^+$  oxidation state in the ground state. For example, Figure 11A compares the Cu  $L$ -edge X-ray absorption near-edge spectrum (XANES) of copper-doped CdSe NCs to that of copper metal ( $Cu(0)$ ) deposited on Si, CuI ( $Cu^+$ ), and CuSe ( $Cu^{2+}$ ), normalized at the  $L_3$  maximum.<sup>61</sup> The X-ray absorption onset energy in the copper-doped CdSe NCs is most similar to that of CuI, indicating that copper incorporates into these NCs in the +1 oxidation state. Similarly, Figure 11B presents results of  $K$ -edge XANES measurements of copper-doped CdSe NCs alongside spectra of Cu foil ( $Cu(0)$ ), CuCl ( $Cu^+$ ), and CuCl<sub>2</sub> ( $Cu^{2+}$ ) standards.<sup>63</sup> Again, the copper-doped CdSe NC data are consistent with a  $Cu^+$  oxidation state. Cu  $K$ -edge XANES<sup>106</sup> and X-ray photoelectron spectroscopy (XPS)<sup>42</sup> measurements performed on copper-doped ZnSe NCs also indicate incorporation of copper in the +1 oxidation state.

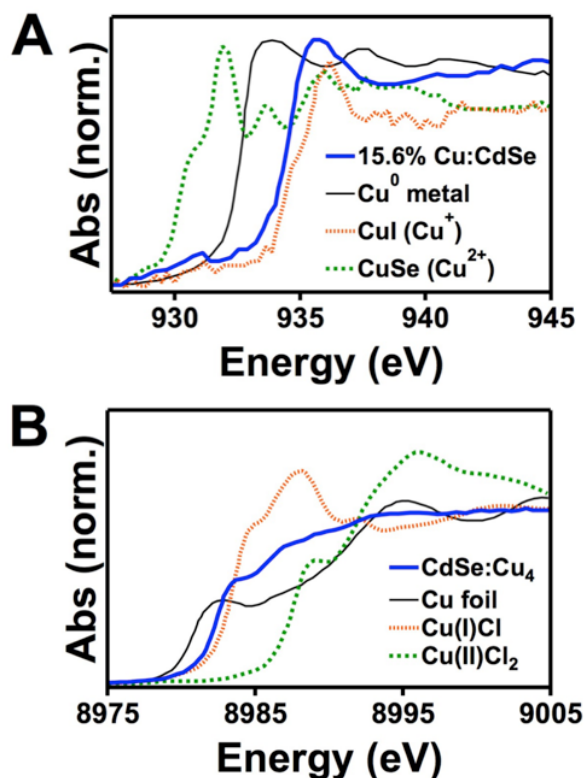


**Figure 11.** A) Cu *L*-edge XANES spectra of Cu<sup>+</sup>:CdSe nanocrystals, Cu metal, CuI, and CuSe. Adapted with permission from ref. <sup>61</sup>. Copyright 2004 American Chemical Society. B) Cu *K*-edge XANES of CdSe:Cu<sub>4</sub>, Cu foil, CuCl, and CuCl<sub>2</sub>. Adapted with permission from ref. <sup>63</sup>. Copyright 2013 American Chemical Society.

Extended X-ray absorption fine structure (EXAFS) data indicate that Cu<sup>+</sup> is a substitutional dopant in II-VI NCs.<sup>39,63,138</sup> The +1 oxidation state means that copper requires a positive countercharge to compensate for its substitution of a +2 lattice cation. Some reports have described the use of cationic substitutional co-dopants, such as Al<sup>3+</sup>, In<sup>3+</sup>, or Ga<sup>3+</sup> (see Figure 8),<sup>103,106-108</sup> or anionic substitutional co-dopants, such as Cl<sup>-</sup> or Br<sup>-</sup>,<sup>39,104,105</sup> to provide the compensating charge. Even in the absence of a co-dopant, however, the excess charge of a substitutional Cu<sup>+</sup> impurity can be easily compensated at the nanocrystal surface through the loss of a negatively charged ligand or through a surface non-stoichiometry.<sup>27,28</sup> The charges of up to 95% of aliovalent Al<sup>3+</sup> dopants in Al<sup>3+</sup>:ZnO nanocrystals are compensated at the NC surfaces, for example.<sup>27</sup> Although Cu<sup>+</sup> is often a *p*-dopant in bulk chalcogenides, Cu<sup>+</sup>-doped chalcogenide NCs do not exhibit the

excitonic bleach or intra-band absorption features characteristic of charge-compensating delocalized *p*-type carriers,<sup>28</sup> indicating negligible charge compensation by this route. EXAFS data collected on copper-doped ZnS NCs suggest that some copper dopants may be compensated by adjacent anion vacancies.<sup>138</sup> In bulk systems, first-coordination-sphere anion vacancies are responsible for the "red" copper ("R-Cu") luminescence,<sup>4,5,146</sup> and such dopant-vacancy complexes do not contribute to the G-Cu luminescence that is almost exclusively observed in nanocrystals. Only one example of potential R-Cu PL in Cu<sup>+</sup>-doped NCs could be found (see Figure 22, Section 4.4).<sup>37</sup> Furthermore, the very small zero-field splittings observed by MCPL in Cu<sup>+</sup>:CdSe and Cu<sup>+</sup>:InP NCs<sup>64</sup> are consistent with those observed for four-coordinate Cu<sup>+</sup> centers in bulk II-VI and III-V semiconductors.<sup>147-149</sup> A three-coordinate Cu<sup>+</sup> center formed by an adjacent anion vacancy would likely have a much larger zero-field splitting due to its greater structural anisotropy. Therefore, the Cu<sup>+</sup> centers compensated by anion vacancies observed by EXAFS likely do not contribute to the observed luminescence. It is intriguing to consider the possibility that such dopant-vacancy pairs might actually exist but not luminesce, perhaps contributing to the low PL QYs frequently observed in Cu<sup>+</sup>-doped NCs, but at this time such an interpretation would be purely speculative.

### **3. Redox Properties**

The previous section established that the characteristic broad luminescence of copper-doped nanocrystals arises from Cu<sup>+</sup> dopants rather than from Cu<sup>2+</sup> dopants. Under many conditions, Cu<sup>+</sup> ions may be easily oxidized to Cu<sup>2+</sup> by addition of a suitable oxidant or application of an appropriate electrochemical potential. This section describes how redox experiments have been used to affect the optical properties of copper-containing nanocrystals.

In stoichiometric  $\text{Cu}_2\text{E}$  ( $\text{E} = \text{S}, \text{Se}, \text{Te}$ ), lattice copper adopts the +1 oxidation state. X-ray diffraction (XRD) and XPS studies on  $\text{Cu}_2\text{Se}$  nanocrystals indicate oxidation of surface copper to form  $\text{CuO}$ .<sup>150</sup> Various oxidizing and reducing reagents have been used to reversibly tune the surface chemistry and localized surface plasmon resonances (LSPRs) of these materials,<sup>151</sup> but most reports do not discuss their luminescence. Compared to other copper-containing nanocrystals, the high inherent defect concentrations of even the quasi-stoichiometric copper chalcogenides likely hinder observation of their luminescence by introducing rapid carrier trapping or nonradiative Auger recombination pathways.

Although rarely observed,  $\text{Cu}_{2-x}\text{S}$  nanocrystals have been reported to exhibit a broad luminescence band similar to those of the copper-doped and copper-based nanocrystals described in Section 2, provided they are kept in inert atmosphere.<sup>152</sup> Figure 12A shows PL spectra of  $\text{Cu}_{2-x}\text{S}$  NCs at increasing values of  $x$ , collected during  $\text{Cu}^+$  oxidation and  $\text{Cu}_{2-x}\text{S}$  vacancy formation caused by exposure to ambient atmosphere.<sup>152</sup> With oxidation, the PL intensity decreases markedly until it is nearly unobservable. The inset shows that an intense NIR absorption band grows in simultaneously with the decrease in PL intensity, attributed to a LSPR involving charge-compensating holes in the  $\text{Cu}_{2-x}\text{S}$  valence band.<sup>152-154</sup> Time-resolved PL measurements of  $\text{Cu}_{2-x}\text{S}$  NCs (Figure 12B) reveal bi-exponential decay curves with fast and slow components that have time constants of roughly 10 ps (instrument-response limited) and 100 ps, respectively. As the nanocrystals oxidize and the LSPR grows, the fast decay component becomes more prominent and the longer-time component is suppressed, likely reflecting nonradiative Auger recombination facilitated by the introduction of extra charge carriers into the valence band.<sup>152</sup> Both the PL intensity and LSPR absorption features are reversibly tunable using redox reagents. After exposure to  $\text{O}_2$  and complete quenching of the PL, addition of the reductant diisobutylaluminum hydride

leads to recovery of the PL intensity, attributed to reduction of valence-band holes as indicated by the simultaneous suppression of the LSPR.<sup>152</sup> Upon re-oxidation (*i.e.*, by re-exposure to air), the PL intensity decreases again and the LSPR re-emerges. These data illustrate facile redox control of the absorption and luminescence of copper-based semiconductor nanocrystals.

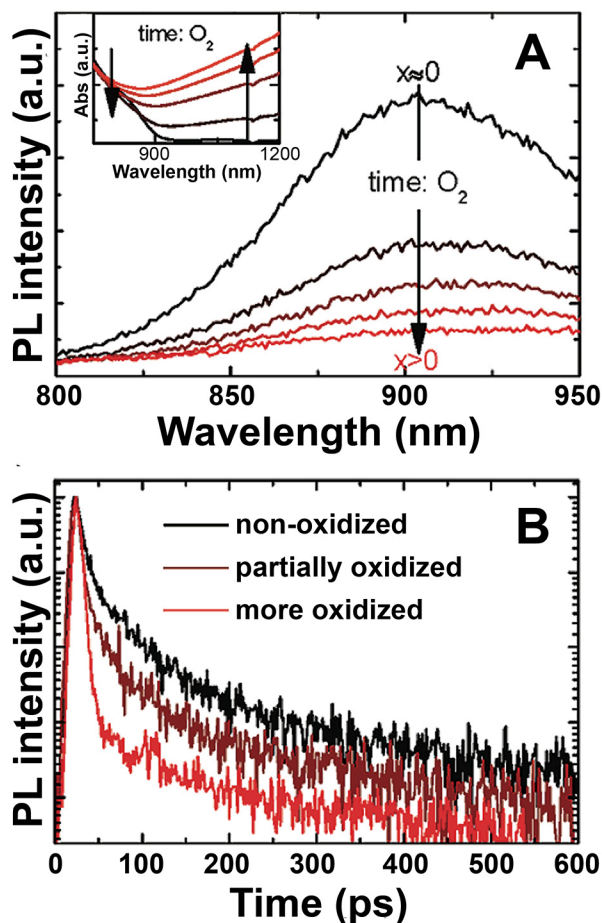


**Figure 12.** **A)** PL spectra of colloidal  $\text{Cu}_{2-x}\text{S}$  NCs ( $d = 5$  nm) in toluene measured at varying times of exposure to  $\text{O}_2$ . Inset: Corresponding increase in LSPR intensity upon oxidation. **B)** Time-resolved PL measurements ( $\lambda_{\text{exc}} = 400$  nm) of  $\text{Cu}_{2-x}\text{S}$  nanocrystals before oxidation, and at various degrees of oxidation. Adapted with permission from ref. <sup>152</sup>. Copyright 2012 American Chemical Society.

As with the  $\text{Cu}_{2-x}\text{E}$  NCs, redox chemistry has also been used to tune the optical properties of copper-doped semiconductor NCs. Figure 13A shows absorption spectra of ZnS NCs and copper-doped ZnS NCs before and after addition of the reductant sodium borohydride ( $\text{NaBH}_4$ ).<sup>40</sup> The

spectra of both the undoped and doped NCs show excitonic absorption at  $\sim 320$  nm, and the doped NCs appear to remain intact after treatment with  $\text{NaBH}_4$ . Figure 13B shows PL spectra of these copper-doped ZnS NCs at various times after addition of  $\text{NaBH}_4$ . The as-synthesized doped nanocrystals exhibit a PL peak associated with surface traps centered around 420 nm; the undoped ZnS NC PL spectrum contains a similar PL peak. Upon addition of  $\text{NaBH}_4$ , a second, broader luminescence peak grows in at 540 nm. When undoped ZnS NCs were treated similarly, no new luminescence peaks appeared. The dopant-related peak at 540 nm is reversibly removed upon adding potassium peroxodisulfate ( $\text{K}_2\text{S}_2\text{O}_8$ ), an oxidizing agent. Within 15 minutes, the re-oxidation is complete and the PL peak at 540 nm has disappeared (Figure 13C). Figure 13D shows the EPR spectrum of the as-synthesized copper-doped ZnS NCs. A signal attributed to paramagnetic  $\text{Cu}^{2+}$  is observed at 330 mT, which is unusual for copper-doped nanocrystals. When  $\text{NaBH}_4$  is added, the EPR signal disappears (Figure 13E) as  $\text{Cu}^{2+}$  is reduced to  $\text{Cu}^+$ . The EPR signal returns (Figure 13F) when  $\text{K}_2\text{S}_2\text{O}_8$  is added to oxidize  $\text{Cu}^+$  back to  $\text{Cu}^{2+}$ . These results suggest that the dopant-related PL centered at 540 nm in copper-doped ZnS NCs, which is likely the  $\text{ML}_{\text{CBCT}}$  luminescence, is associated with copper dopants in the +1 oxidation state, rather than the +2 oxidation state. Curiously, the EPR resonance in Figure 13D corresponds to a  $g$  value close to 2.0, which would be unexpectedly large for substitutional  $\text{Cu}^{2+}$  within ZnS. Spin-orbit interactions shift ground-state  $g$  values to well below 2.0 in bulk  $\text{Cu}^{2+}$ -doped ZnS.<sup>140,141</sup> It is unclear how to reconcile these observations, and the possibility that this EPR signal arises from some extrinsic copper in the nanocrystal sample must be considered.

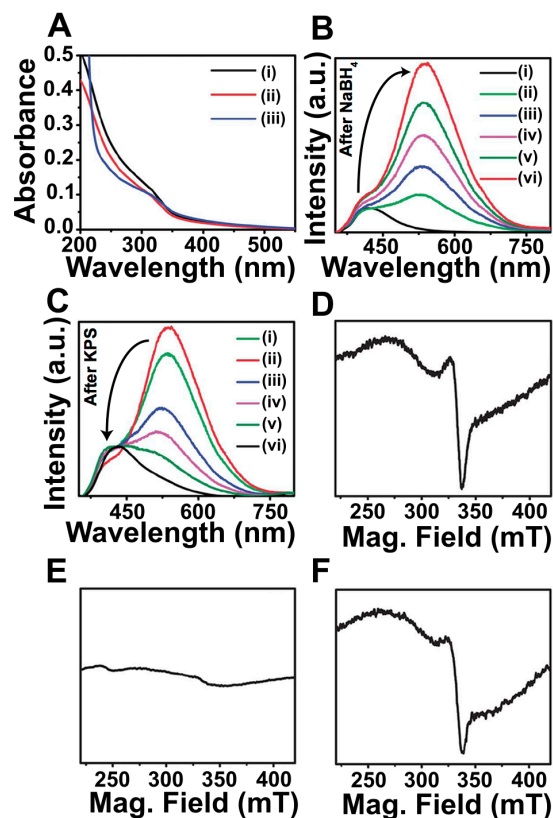


**Figure 13.** **A)** Absorption spectra of (i) ZnS (black), (ii)  $\text{Cu}^{2+}:\text{ZnS}$  (red) and (iii)  $\text{NaBH}_4$ -treated  $\text{Cu}^{2+}:\text{ZnS}$  (blue) nanocrystals. **B)** PL spectra of  $\text{Cu}^{2+}:\text{ZnS}$  (i) prior to treatment with  $\text{NaBH}_4$  and (ii) 10 min, (iii) 20 min, (iv) 30 min, (v) 40 min, and (vi) 60 min after  $\text{NaBH}_4$  treatment. **C)** PL spectra of  $\text{Cu}^{2+}:\text{ZnS}$  NCs (i) treated with  $\text{NaBH}_4$ , (ii) following pH adjustment by adding dilute HCl acid, (iii) immediately after treatment with  $\text{K}_2\text{S}_2\text{O}_8$ , and (iv) 5 min, (v) 10 min and (vi) 15 min after  $\text{K}_2\text{S}_2\text{O}_8$  treatment. The arrows in **(B)** and **(C)** indicate the increase and decrease of the copper-based PL with time after addition of  $\text{NaBH}_4$  and  $\text{K}_2\text{S}_2\text{O}_8$ , respectively. **D-F)** EPR spectra of **(D)** as synthesized  $\text{Cu}^{2+}:\text{ZnS}$  nanocrystals, **(E)**  $\text{Cu}^{2+}:\text{ZnS}$  nanocrystals treated with  $\text{NaBH}_4$ , and **(F)**  $\text{Cu}^{2+}:\text{ZnS}$  nanocrystals after subsequent addition of  $\text{K}_2\text{S}_2\text{O}_8$ . Adapted with permission from ref. <sup>40</sup>. Copyright 2014 Royal Society of Chemistry.

Electrochemical methods have also been explored for tuning the optical properties of copper-doped semiconductor NCs. Figure 14 shows luminescence spectra of copper-doped ZnSe/CdSe core/shell NCs measured as a function of applied potential.<sup>155</sup> As in Figures 4 and 7, both band-edge excitonic PL (centered at  $\sim 2.0$  eV) and copper-based PL (centered at  $\sim 1.5$  eV) are observed. As the applied potential is swept negative, the intensity of the copper-based PL increases by a factor of 2.2. Simultaneously, the intensity of the band-edge emission decreases by  $\sim 20\%$ .

Accounting for the different bandshapes of the two PL features, the change in copper-based PL is ~3 times as large as that in the band-edge PL. Both changes are reversible upon sweeping the applied potential back to zero volts.

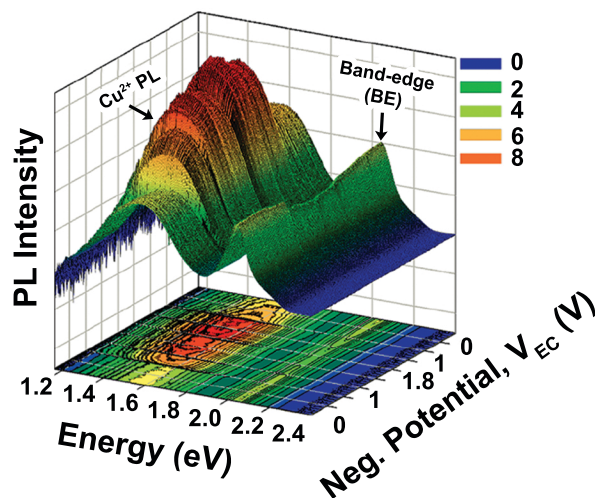


**Figure 14.** Three-dimensional plot of PL spectra (x and y axes) of a film of copper-doped ZnSe/CdSe core/shell NCs on Sn<sup>4+</sup>:In<sub>2</sub>O<sub>3</sub> (ITO) measured under various magnitudes of negative applied potentials (z axis) in a spectroelectrochemical cell using propylene carbonate as an electrolyte and a silver wire reference electrode. Adapted with permission from ref. <sup>155</sup>. Copyright 2012 American Chemical Society.

Although the presence of both band-edge and copper-based PL could suggest that a significant fraction of the nanocrystals do not contain copper dopants (see Section 2.2), the authors here have proposed that both features actually arise from competing radiative recombination processes in the *same* copper-doped nanocrystals. Moreover, the broad ML<sub>CBCT</sub> luminescence was interpreted as originating from Cu<sup>2+</sup> dopants,<sup>155</sup> which appears unlikely given the electronic structures of Cu<sup>2+</sup>-doped chalcogenide semiconductors discussed in Section 2.4. Nevertheless, the data do illustrate that the copper-based and band-edge PL respond differently to the applied potential. These changes in PL intensity with applied potential are most likely due to electrochemical modulation of the oxidation states of mid-gap surface traps,<sup>156</sup> because the range of applied potentials used is far below the conduction band-edge.<sup>155</sup> According to the authors of ref. <sup>155</sup>, applying a negative

potential adds electrons to surface states, which has the dual effect of passivating electron traps while simultaneously activating hole traps. The copper PL is described as almost exclusively sensitive to electron traps because the hole is localized at a copper site in the  $ML_{CBCT}$  excited state.<sup>16</sup> The copper PL therefore increases in intensity upon reduction of surface electron traps.<sup>155</sup> On the other hand, the electron-trap passivation and hole-trap activation are described as largely offsetting one another, resulting in a relatively small decrease in the band-edge PL intensity. The results presented in Figure 14 demonstrate how the electronic structure of the  $ML_{CBCT}$  excited state, which contains a delocalized electron and a localized hole, causes the copper-based PL to respond differently to a change in the surface redox state than a luminescent excited state in which both the electron and hole are delocalized.

## 4. Photophysics

### 4.1. Charge-Transfer Nature of the Luminescent Excited State

Several spectroscopic and computational studies have been carried out to investigate the nature of the luminescent excited state in copper-doped NCs. DFT calculations on copper-doped semiconductors have provided insight into the position of the copper dopant levels relative to the band edges, and the extent to which the electron and hole are delocalized in the luminescent excited states.<sup>95,106,107</sup> Figure 15A shows the energies of the molecular orbitals calculated for a discrete  $Cu^+ : Cd_{33}Se_{34}$  NC using an atomic basis set and the hybrid PBE0 functional, with surface passivation from fractionally charged pseudo-hydrogen atoms.<sup>95</sup> This calculation shows five doubly occupied orbitals with significant copper  $3d$  character in the CdSe bandgap. Visualization of the natural transition orbitals (NTOs) for the lowest-energy excited state of a  $Cu^+ : Cd_{76}Se_{77}$  NC indicates that the hole is localized at the copper while the electron is delocalized over the entire NC

volume, *i.e.*, in the conduction band (Figure 15B). This result is consistent with the assignment of the luminescent excited state as a  $ML_{CBCT}$  state discussed above.

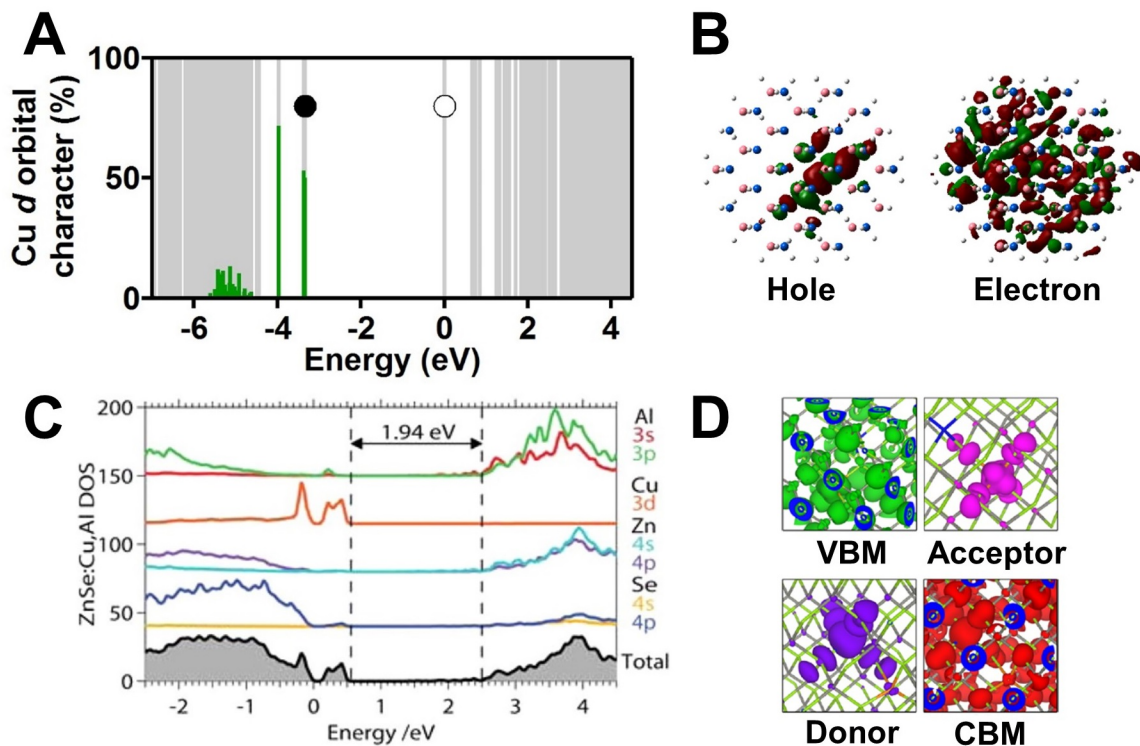


**Figure 15.** **A)** Calculated molecular-orbital energies for a  $Cu^+ : Cd_{33}Se_{34}$  NC. The  $Cu(3d)$  atomic orbital character is highlighted in green and the highest occupied and lowest unoccupied molecular orbitals (HOMO and LUMO) are indicated by closed and open circles, respectively. Five doubly occupied orbitals with significant  $Cu(3d)$  character are located in the bandgap, near the VB edge. Adapted with permission from ref. <sup>95</sup>. Copyright 2016 American Chemical Society. **B)** Natural transition orbitals (NTOs) calculated for the lowest-energy singlet excited state of a  $Cu^+ : Cd_{76}Se_{77}$  NC, showing the excited-state hole and electron wavefunctions. The hole is localized around the copper dopant, while the electron is delocalized in the conduction band. Adapted with permission from ref. <sup>95</sup>. Copyright 2016 American Chemical Society. **C)** Partial density of states calculated for bulk  $Cu^+, Al^{3+}$ -codoped ZnSe (colored lines). The shaded black area represents the total density of states, and the contributions of the  $Cu 3d$  orbitals and  $Al 3s$  and  $3p$  orbitals are shown in orange, red, and green, respectively. Reprinted with permission from ref. <sup>107</sup>. Copyright 2015 American Chemical Society. **D)** Integrated local density of states calculated for bulk  $Cu^+, Ga^{3+}$ -codoped ZnSe, showing the spatial occupation of the density of states for the valence-band maximum (VBM),  $Cu^+$ -related acceptor state,  $Ga^{3+}$ -related donor state, and conduction-band minimum (CBM). Although the valence-band and conduction-band orbitals are delocalized, the acceptor and donor orbitals are localized around the  $Cu^+$  and

Ga<sup>3+</sup> dopants, respectively. Adapted with permission from ref. <sup>107</sup>. Copyright 2015 American Chemical Society.

Several DFT calculations on Cu<sup>+</sup>:ZnSe containing additional trivalent cationic co-dopants (M<sup>3+</sup>) have also shown copper-based acceptor levels in the ZnSe bandgap.<sup>106,107</sup> Figure 15C shows the density of states for Cu<sup>+</sup>,Al<sup>3+</sup>:ZnSe (bulk) calculated using a plane-wave basis set and 64-atom supercell with the PBE functional.<sup>107</sup> In these calculations, the Cu<sup>+</sup> 3d(*e*) orbitals contribute to the valence band (sharp peak at -0.15 eV in Figure 15C), while the Cu<sup>+</sup> 3d(*t*<sub>2</sub>) orbitals fall inside the bandgap (two peaks at 0.1-0.4 eV in Figure 15C). The 3s and 3p orbitals of the Al<sup>3+</sup> co-dopant hybridize with CB orbitals largely comprising Zn<sup>2+</sup> 4s and 4p orbitals, but with some anion contribution. In contrast, some M<sup>3+</sup> co-dopants, such as Ga<sup>3+</sup>, are predicted to introduce localized donor states below the CB edge. Figure 15D depicts the relevant orbitals computed for Cu<sup>+</sup>,Ga<sup>3+</sup>:ZnSe (bulk): delocalized CB- and VB-edge orbitals, a localized acceptor orbital at Cu<sup>+</sup>, and a localized donor orbital at Ga<sup>3+</sup>. In this system, the calculations are interpreted as suggesting that PL in Cu<sup>+</sup>,Ga<sup>3+</sup>:ZnSe NCs stems from DAP recombination of a Ga<sup>3+</sup>-bound electron with a Cu<sup>+</sup>-bound hole. Importantly, all of the DFT results shown in Figure 15, regardless of host lattice, co-dopant, DFT method, or semiconductor dimensionality (NC or bulk) display localized copper acceptor levels within the bandgap, and significant hole localization at copper in the excited state.

As shown in Figure 10C, bulk copper-doped semiconductors exhibit a broad, sub-bandgap "characteristic" absorption band corresponding to direct excitation of the Cu<sup>+</sup> ML<sub>CB</sub>CT excited state.<sup>12</sup> A weak, broad sub-bandgap absorption "foot" has also been reported for several copper-doped semiconductor NCs.<sup>59,64,65</sup> In copper-doped CdS NCs, this absorption foot was attributed to the formation of ultra-small Cu<sub>2-x</sub>S particles during copper doping.<sup>59</sup> In copper-doped InP NCs, the sub-bandgap absorption was shown to increase with increasing copper concentration, and the foot was attributed to electronic doping from charge carriers that compensate the aliovalent Cu<sup>+</sup> or Cu<sup>2+</sup>

ions.<sup>65</sup> CdS NCs co-doped with  $\text{In}^{3+}$  and  $\text{Cu}^+$  also displayed a similar feature at high dopant concentrations.<sup>108</sup> This result was attributed to the formation of alloyed  $\text{Cu}_x\text{In}_x\text{Cd}_{2-2x}\text{S}_2$ , which has a band structure similar to  $\text{CuInS}_2$  and typically displays a low-energy shoulder in the absorption. More recently, this absorption foot was examined in  $\text{Cu}^+:\text{CdSe}$  and  $\text{Cu}^+:\text{InP}$  NCs (Figure 16),<sup>64</sup> where it was attributed to direct  $\text{ML}_{\text{CBCT}}$  excitation promoting a  $\text{Cu}^+$  electron to the conduction band, as it is assigned in bulk  $\text{Cu}^+$ -doped ZnS.<sup>12</sup> DFT calculations on small  $\text{Cu}^+:\text{CdSe}$  NCs also predict a similar broad sub-bandgap absorption foot arising from  $\text{ML}_{\text{CBCT}}$  excitation.<sup>95</sup> The spectra in Figure 16 are plotted in terms of the per-copper extinction coefficient,  $\epsilon_{\text{Cu}}$ , thereby normalizing for the copper concentrations of each sample. Both copper-doped samples show similar values of  $\epsilon_{\text{Cu}}$  ( $\epsilon_{\text{Cu}} < 1000 \text{ M}_{\text{Cu}}^{-1}\text{cm}^{-1}$ ). Figure 16 also includes the low-energy absorption spectrum of  $\text{CuInS}_2$  NCs, again plotted as  $\epsilon_{\text{Cu}}$ . Interestingly, the absorption spectrum of  $\text{CuInS}_2$  NCs bears a striking resemblance to the  $\text{ML}_{\text{CBCT}}$  absorption foot in the  $\text{Cu}^+$ -doped semiconductor NCs, suggesting that the broad absorption onset of  $\text{CuInS}_2$  NCs may be due to an analogous  $\text{ML}_{\text{CBCT}}$ -type transition that generates copper-localized holes, rather than excitonic absorption involving delocalized holes.<sup>64</sup>

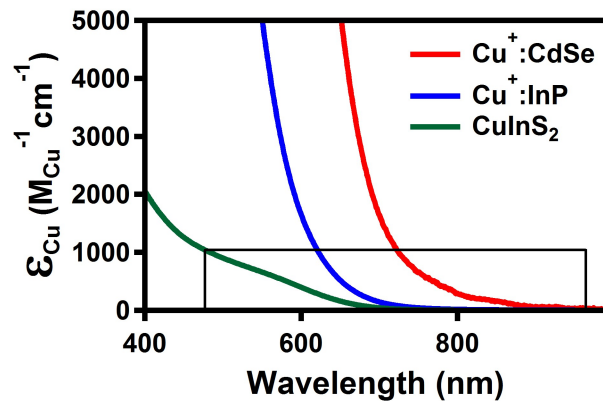


**Figure 16.** Absorption spectra of  $\text{Cu}^+:\text{CdSe}$  (red),  $\text{Cu}^+:\text{InP}$  (blue), and  $\text{CuInS}_2$  (green) NCs, plotted in units of per-copper extinction coefficient ( $\epsilon_{\text{Cu}}$ ). The box highlights the sub-

bandgap absorption, which is attributed to the  $\text{Cu}^+$   $\text{ML}_{\text{CBCT}}$  transition. Adapted with permission from ref. <sup>64</sup>. Copyright 2015 American Chemical Society.

Analysis of the temperature dependence of the PL lifetime and MCPL for  $\text{Cu}^+$ -doped and  $\text{CuInS}_2$  NCs has revealed very similar singlet-triplet splittings in the luminescent excited states of all of these materials.<sup>64</sup> Copper is in the +1 oxidation state in these materials, and no evidence for ground-state  $\text{Cu}^{2+}$  was observed.<sup>64</sup> Figure 17A plots PL lifetimes versus temperature for  $\text{Cu}^+:\text{CdSe}$ ,  $\text{Cu}^+:\text{InP}$ , and  $\text{CuInS}_2$  NCs. The lifetimes of all three materials show a remarkably similar dependence on temperature: at temperatures above 60 K, the lifetimes are fairly constant with temperature, but at temperatures below 60 K they increase steeply with decreasing temperature, although the PL QY is relatively constant.<sup>64</sup> A previous report of nearly identical temperature-dependent PL lifetimes in  $\text{CuInS}_2$  NCs attributed this behavior to carrier trapping and de-trapping processes.<sup>157</sup> Figure 17A also plots the MCPL polarization ratio versus temperature, measured at an applied magnetic field of 6 T. A temperature-dependent MCPL signal is observed that is consistent with excited-state magnetic exchange coupling between the unpaired conduction-band spin and the unpaired copper-localized spin. This exchange interaction introduces an energy splitting between singlet and triplet luminescent excited states (Figure 17B). Analogous excited-state singlet-triplet splittings were established for luminescent  $\text{Cu}^+$  molecular coordination complexes<sup>19,20,158</sup> and bulk  $\text{Cu}^+$ -doped semiconductors<sup>159,160</sup> many years ago. Emission from the triplet excited state is formally spin-forbidden, and therefore has a smaller radiative rate constant ( $k_{\text{T}}$ ) than emission from the singlet excited state ( $k_{\text{S}}$ ). The observation that the PL lifetimes increase with decreasing temperature (Figure 17A) indicates that the triplet excited state is lower in energy than the singlet excited state, and hence that the exchange coupling between the CB-electron and the copper-localized spin is ferromagnetic in the  $\text{ML}_{\text{CBCT}}$  excited states of these NCs (Figure 17C).

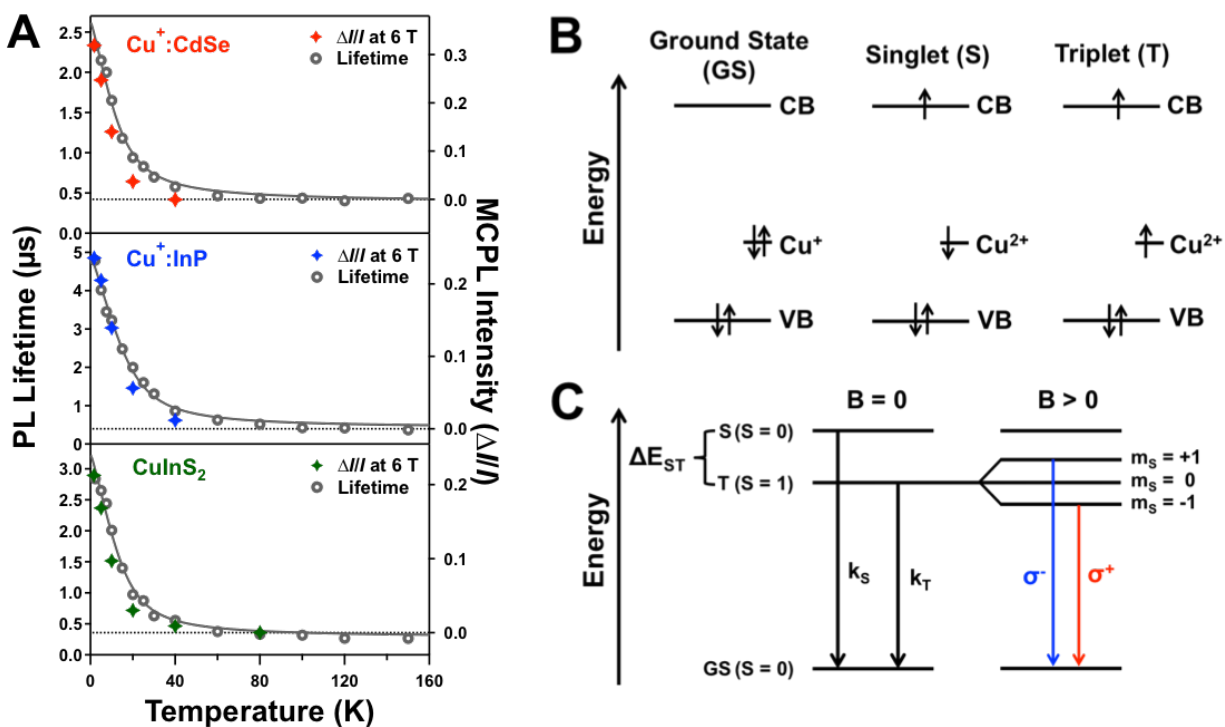


**Figure 17.** **A**) MCPL intensities (6 T, closed crosses) and PL lifetimes (0 T, open circles) plotted versus temperature for Cu<sup>+</sup>:CdSe (red), Cu<sup>+</sup>:InP (blue), and CuInS<sub>2</sub> (green) NCs. The solid gray lines are fits of the temperature-dependent lifetimes to a model that accounts for a distribution of singlet-triplet splittings in the luminescent excited state. **B**) Orbital energy level diagram depicting the ground-state and singlet and triplet luminescent excited-state configurations of a copper-doped semiconductor nanocrystal. “CB” and “VB” denote the lowest- and highest-energy conduction- and valence-band orbitals, respectively. For simplicity, only the highest-energy copper 3*d* orbital is shown. **C**) Qualitative energy level diagrams illustrating the energies of the singlet and triplet luminescent excited states from **(B)** and their splitting in an applied magnetic field ( $B > 0$ ), which gives rise to MCPL intensity. Adapted with permission from ref. <sup>64</sup>. Copyright 2015 American Chemical Society.

MCPL in the copper-doped NCs arises from a Zeeman splitting of the triplet ML<sub>CB</sub>CT excited state that decreases the energy of the  $m_s = -1$  sublevel, which emits right circularly polarized light ( $\sigma^+$ ), and increases the energy of the  $m_s = +1$  sublevel, which emits left circularly polarized light ( $\sigma^-$ , Figure 17C).<sup>64</sup> This splitting increases the  $m_s = -1$  population relative to the  $m_s = +1$  population at low temperatures and large applied magnetic fields, and thereby gives rise to the observed MCPL signal. Because the singlet excited state does not split under an applied magnetic

field, MCPL selectively probes the triplet excited state to first order. Figure 17A demonstrates that the MCPL polarization ratio has the same temperature dependence as the PL lifetimes, confirming the interpretation of both in terms of a singlet-triplet splitting within the luminescent  $ML_{CBCT}$  excited state. Fits of the lifetime data in Figure 17A to a kinetic model that accounts for a distribution in singlet-triplet splitting energies within the ensemble of NCs yielded average singlet-triplet energies of  $\sim 1$  meV for  $Cu^+ : CdSe$ ,  $Cu^+ : InP$ , and  $CuInS_2$  NCs.<sup>64</sup> DFT calculations on  $Cu^+ : CdSe$  NCs predict the experimental singlet-triplet splitting with the correct sign and magnitude.<sup>95</sup> A non-linearity observed in the low-field field dependence ( $< 1$  T) of the MCPL measured for copper-doped ZnSe/CdSe core/shell and  $CuInS_2$  NCs at low temperatures has been interpreted in terms of complex ground-state splittings of the  $Cu^{2+}$  acceptor.<sup>72</sup> The singlet-triplet splitting diagram of Figure 17C suggests interpretation of this non-linearity, which was also observed in  $Cu^+ : CdSe$  and  $Cu^+ : InP$  NCs,<sup>64</sup> in terms of a zero-field splitting of the luminescent triplet excited state.

#### **4.2. Origin of the Broad Photoluminescence Bandshape and Large Stokes Shift**

All of the copper-doped and copper-based semiconductor nanocrystals listed in Table 1 display broad PL with ensemble fwhm  $\sim 0.2$ - $0.6$  eV, much larger than the fwhm typically observed for excitonic luminescence (*e.g.*, ensemble fwhm  $< \sim 0.1$  eV for CdSe NCs).<sup>161-163</sup> For both excitonic and copper-based PL, the ensemble fwhm can be inhomogeneously broadened by the NC size distribution, but if the ensemble size distribution is narrow enough, then the ensemble fwhm approaches the single-NC fwhm. The latter may still be inhomogeneously broadened due to spectral diffusion.<sup>164-166</sup> For undoped CdSe NCs, the time-averaged single-particle excitonic fwhm is typically  $\sim 50$  meV at room temperature.<sup>16,161,166,167</sup> For copper-doped NCs, all indications are that the single-particle PL bands are nearly as broad as the ensemble values reported in Table 1,

with time-averaged fwhm values almost an order of magnitude greater than those typical of excitonic PL.<sup>16,155,168</sup> These PL bandwidths have been investigated by optical microscopic studies of  $\text{Cu}^+, \text{Al}^{3+}:\text{ZnS}$  nanostructures formed by ion implantation<sup>168</sup> and single colloidal  $\text{Cu}^+:\text{CdSe}$  NCs,<sup>16</sup> and also by luminescence line narrowing in ensembles of copper-doped  $\text{ZnSe}/\text{CdSe}$  core/shell NCs.<sup>155</sup> Each measurement leads to the same conclusion: the copper-based luminescence in these materials is intrinsically broad.

The luminescence of  $\text{Cu}^+, \text{Al}^{3+}:\text{ZnS}$  nanostructures has been measured using scanning near-field optical microscopy (Figure 18A), revealing the room-temperature PL bandwidth of a single nanostructure to be  $\sim 350$  meV.<sup>168</sup> The PL spectrum narrows with decreasing temperature, possibly suggesting some vibronic contribution to the bandwidth, but the observed low-temperature fwhm of  $\sim 275$  meV is still quite large. Here, the broad bandshape was attributed to strong electron-phonon coupling and a distribution of donor-acceptor pair distances within the  $\text{Cu}^+, \text{Al}^{3+}$ -codoped ZnS nanostructures. PL spectra of single colloidal  $\text{Cu}^+:\text{CdSe}$  NCs in the low-doping (single  $\text{Cu}^+$  per NC) limit have also been measured, from which a room-temperature fwhm of  $\sim 325$  meV is obtained (Figure 18B).<sup>16</sup> The broad bandshape in this case was attributed primarily to strong electron-phonon coupling, which leads to a large nuclear distortion around the copper in the luminescent excited state.<sup>16</sup> Low-temperature fluorescence line narrowing measurements of an ensemble of colloidal copper-doped  $\text{CdSe}/\text{ZnSe}$  core/shell NCs (Figure 18C) show copper-based PL bandwidths of 350-400 meV.<sup>155</sup> This technique uses a narrow excitation source centered below the average bandgap energy of the ensemble to selectively excite a small subset of the nanocrystals, thereby minimizing inhomogeneous broadening due to size distribution. The observation that the bandwidth of the copper PL is not much smaller in the fluorescence line-narrowing measurement compared to the ensemble PL measurement suggests that the ensemble

bandwidth is largely unaffected by the NC size distribution. The authors attributed the broad bandshape to a distribution of energies of mid-gap copper levels due to differences in local environments, especially at the core/shell interface.<sup>155</sup>

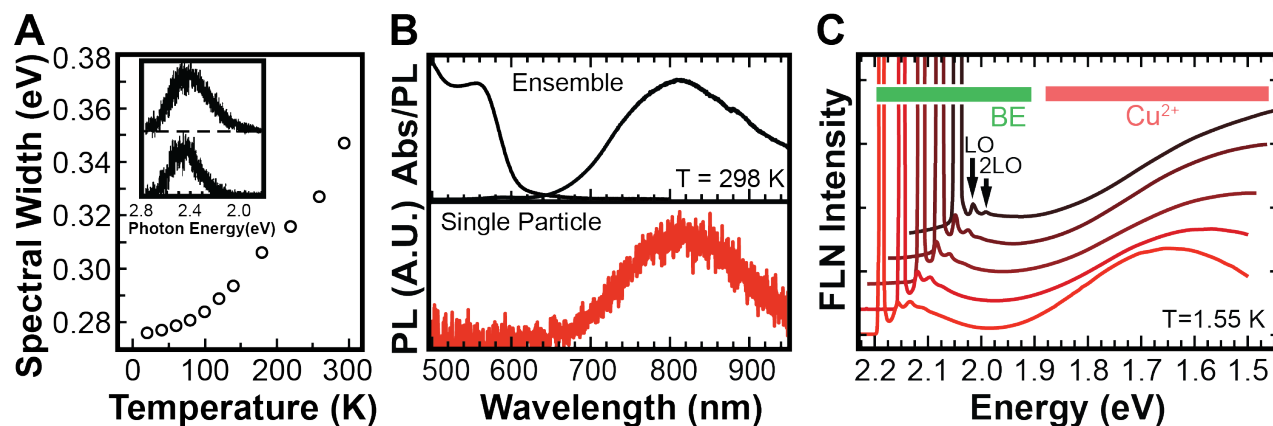


**Figure 18.** Bandshapes of copper-based PL measured in single nanostructures and an ensemble of colloidal NCs. **A)** Temperature dependence of the PL bandwidth of nanostructured  $\text{Cu}^+, \text{Al}^{3+}:\text{ZnS}$ . Inset: PL spectra of individual  $\text{Cu}^+, \text{Al}^{3+}:\text{ZnS}$  nanostructures measured at room temperature (top) and at 20 K (bottom). Adapted with permission from ref. <sup>168</sup>. Copyright 2004 American Institute of Physics. **B)** Ensemble absorption and PL and single particle PL spectra collected at 298 K in  $\text{Cu}^+:\text{CdSe}$  NCs. Adapted with permission from ref. <sup>16</sup>. Copyright 2015 American Chemical Society. **C)** Fluorescence line narrowing measurement of copper-doped core/shell  $\text{ZnSe}/\text{CdSe}$  NCs at 1.55 K. Adapted with permission from ref. <sup>155</sup>. Copyright 2012 American Chemical Society.

DFT calculations support association of the broad bandshapes and large Stokes shifts observed in the  $\text{ML}_{\text{CBCT}}$  PL of  $\text{Cu}^+$ -doped NCs with large excited-state nuclear reorganization at copper.<sup>95</sup> Figure 19 illustrates the relationship between excited-state nuclear reorganization and PL bandshape and Stokes shift. As illustrated in the single-configurational-coordinate diagram of Figure 19A, excited-state distortion along some nuclear coordinate that is coupled to the electronic transition results in vibronic broadening of the associated absorption and PL bands. The broadening also generates a Stokes shift that is related to the nuclear reorganization energies of all relevant distortion coordinates. Figure 19B illustrates such vibronic broadening and the resulting

Stokes shift schematically. For copper-doped semiconductor NCs, the true Stokes shift describes the energy difference between the  $ML_{CBCT}$  absorption “foot” (Figure 16) and the  $ML_{CBCT}$  PL, not the energy difference between the excitonic absorption and  $ML_{CBCT}$  PL, which is defined as the “effective” Stokes shift in Table 1 ( $E_{abs}-E_{PL}$ ). In molecular  $Cu^+$  complexes, MLCT excitation induces a large Jahn-Teller distortion that relieves the orbital degeneracy of the MLCT excited state.<sup>21,25,169,170</sup> DFT calculations suggest that  $Cu^+ : CdSe$  NCs undergo an analogously large nuclear reorganization of a  $CuSe_4$  unit upon  $ML_{CBCT}$  excitation, which further strains the surrounding lattice.<sup>95</sup> The distortion around copper is dominated by contributions from a totally symmetric Cu-Se bond-length contraction with  $A_1$  symmetry (in the  $T_d$  point group) and a symmetry-breaking Jahn-Teller distortion of  $T_2$  symmetry.<sup>95</sup> The computed distortion coordinates and their distortion phases are shown in Figure 19C. Figure 19D shows the simulated vibronic bandshape expected from the  $A_1$  and  $T_2$  distortions calculated by DFT. This spectrum has fwhm  $\sim 175$  meV (at  $T = 0$  K), accounting for a major portion of the experimental PL bandwidths discussed above. These calculations thus explain the microscopic origins of the intrinsically broad  $ML_{CBCT}$  PL bandshapes and large Stokes shifts observed in  $Cu^+$ -doped semiconductor NCs, indicating that both features originate from strong electron-phonon coupling in the  $ML_{CBCT}$  excited state.

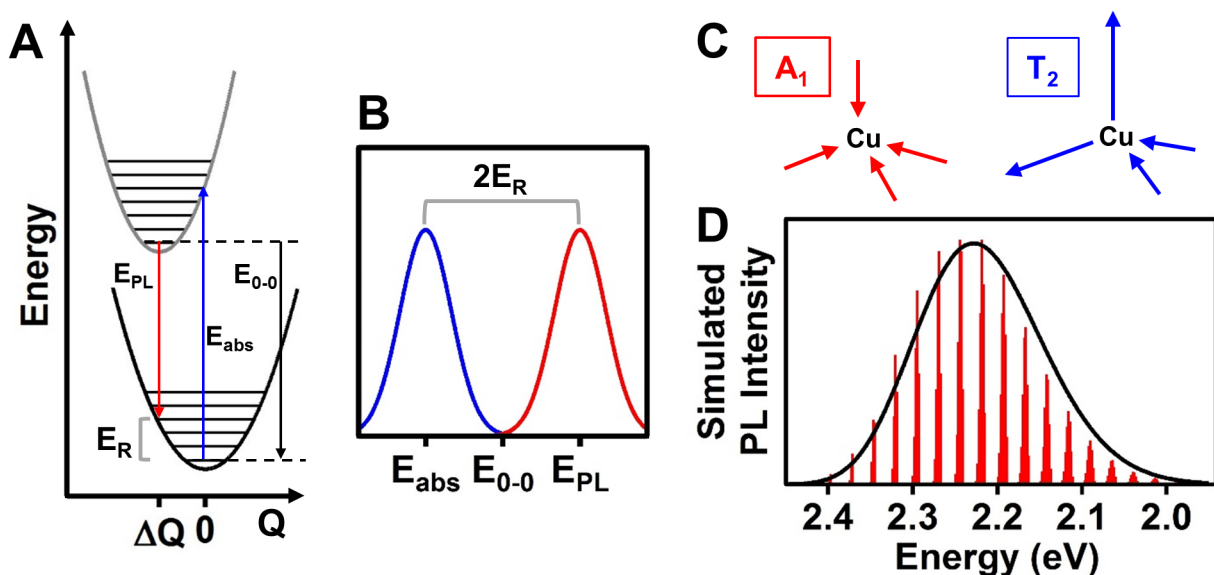


**Figure 19.** **A)** Single-configurational-coordinate diagram for a hypothetical electronic transition coupled to a totally symmetric nuclear distortion, relating the excited-state geometric distortion ( $\Delta Q$ ) to the PL Stokes shift ( $2E_R$ ) and the absorption and PL Frank-Condon band profiles (e.g., related to  $E_{0-0} - E_{PL}$ ). **B)** Schematic absorption (blue) and PL (red) spectra for the transition shown in **(A)**, illustrating the relationship between the reorganization energy  $E_R$  and the Stokes shift. **C)** Illustration of the two major distortions that contribute to the excited-state reorganization around the copper dopant in  $\text{Cu}^+:\text{CdSe}$  NCs, calculated by DFT. **D)** Simulated PL spectrum (black) based on vibronic progressions for the two modes shown in **(C)** (red) and reorganization energies calculated by DFT. The smooth bandshape plotted in black comes from summing Gaussian functions for the individual vibronic transitions shown in red ( $\sigma_{\text{vib}} = 0.0243$  eV). Adapted with permission from ref. <sup>95</sup>. Copyright 2016 American Chemical Society.

#### 4.3. Mechanism of Photoluminescence in $\text{CuInS}_2$ Nanocrystals

It is interesting to note that the spectroscopic properties of many copper-based NCs such as  $\text{CuInS}_2$  appear strikingly similar to those of the copper-doped semiconductor NCs.<sup>64,72</sup> Not just the absorption spectra (Figure 16), but also the PL spectra (Figure 9B), PL lifetimes and temperature dependence (Figure 17), and even MCPL (Figure 17) data are similar. The PL of  $\text{CuInS}_2$  and related NCs is typically interpreted in the same way as bulk  $\text{CuInS}_2$ , by invoking various point defects,<sup>68,69,71,73,74,77,92,116,126,127,157,171-183</sup> but these spectroscopic similarities suggest that similar microscopic descriptions of the luminescent excited states of  $\text{Cu}^+$ -doped and  $\text{Cu}^+$ -based

semiconductor NCs likely apply. Importantly, the PL of CuInS<sub>2</sub> NCs is qualitatively very different from that of bulk CuInS<sub>2</sub>. Bulk CuInS<sub>2</sub> has been studied extensively,<sup>116,171</sup> primarily in relation to its photovoltaic (PV) applications.<sup>184-188</sup> Figure 20 compares absorption and PL spectra of bulk and nanocrystalline CuInS<sub>2</sub>. Bulk CuInS<sub>2</sub> is described as having a direct bandgap at ~1.5 eV.<sup>115-118</sup> It typically displays sharp (fwhm ~ 2 meV) near-band-edge emission around 1.53 eV and broader (fwhm ~ 20 meV) deep-trap emission between 1.4 eV and 1.3 eV.<sup>116</sup> The deep-trap PL is sensitive to preparation conditions, and it has been assigned as DAP recombination involving a deep acceptor level identified as either a copper vacancy (V<sub>Cu</sub>, formed under In<sup>3+</sup>-rich growth conditions) or V<sub>In</sub> or Cu<sub>In</sub> defects (formed under Cu<sup>+</sup>-rich growth conditions), and a relatively shallow donor level identified as In<sub>Cu</sub>, V<sub>S</sub>, or an interstitial In (In<sub>i</sub>).<sup>116,171,189,190</sup>

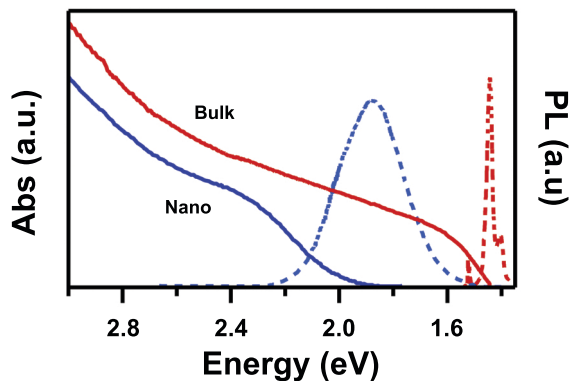


**Figure 20.** Absorption and PL spectra of bulk and nanocrystalline CuInS<sub>2</sub>. The bulk absorption (solid red line, thin-film sample, adapted with permission from ref. <sup>117</sup>, copyright 2006 IOP publishing) and luminescence (dashed red line, adapted with permission from ref. <sup>116</sup>, copyright 1982 Elsevier) spectra have intrinsically different bandshapes than colloidal nanocrystalline CuInS<sub>2</sub> absorption (solid blue) and PL (dashed blue) spectra. Colloidal spectra adapted with permission from ref. <sup>71</sup>. Copyright 2011 American Chemical Society.

Like other semiconductor NCs, nanocrystalline CuInS<sub>2</sub> has a size-tunable bandgap (Figure 9A), but the absorption spectrum does not display a clearly defined excitonic maximum. Instead CuInS<sub>2</sub> NC absorption spectra generally exhibit a broad first absorption band (centered at ~2.35 eV in Figure 20) that tails extensively to lower energies.<sup>70,75</sup> The PL of CuInS<sub>2</sub> NCs is considerably

broader than any of the PL bands of the bulk material, with fwhm  $\sim$ 200-500 meV (Table 1). The Stokes shifts of CuInS<sub>2</sub> NCs are typically reported to be between 180 meV and 500 meV,<sup>64,69,71</sup> although the lack of a distinct absorption feature makes this value difficult to determine accurately. Overall, the PL of CuInS<sub>2</sub> NCs is very different from that of bulk CuInS<sub>2</sub>. A similar conclusion also applies for CuInSe<sub>2</sub>.<sup>191,192</sup>

The broad luminescence and large Stokes shifts in CuInS<sub>2</sub> and CuInSe<sub>2</sub> NCs are often explained by invoking a DAP recombination mechanism, analogous to the deep-trap emission of the corresponding bulk materials.<sup>68,69,172,175,176</sup> As in the bulk materials, these donor and acceptor states have been associated with In<sub>Cu</sub> or anion vacancy (V<sub>S</sub> or V<sub>Se</sub>) defects, and copper vacancies (V<sub>Cu</sub>), respectively.<sup>126,127,177</sup> One of the strongest pieces of evidence for the DAP mechanism is the observation of a PL redshift on the 100-nanosecond timescale in gated PL measurements,<sup>69,157</sup> although some reports attribute this redshift to size-dependent surface trapping kinetics.<sup>73,178</sup> With DAP recombination, the distribution of donor-acceptor distances generates a distribution of PL energies and rate constants,<sup>10</sup> which causes an apparent redshift in the PL peak energy over time.<sup>193</sup> The strong size dependence of CuInS<sub>2</sub> and CuInSe<sub>2</sub> NC PL energies does not appear to be compatible with a DAP model, however.<sup>77,127,179</sup> Instead, the size-dependent PL energy was proposed to originate from a “free-to-bound” recombination mechanism in which one of the carriers is delocalized in the CB or VB and the other carrier is localized at a defect.<sup>77,127,179</sup>

The excitation-power-dependent saturation of the photoinduced bleach of the first absorption peak in CuInS<sub>2</sub> NCs, as measured by transient absorption spectroscopy, is consistent with a “free-to-bound” PL mechanism in which the electron is in the CB and the hole is localized.<sup>71,73,180</sup> Other ultrafast transient absorption and time-resolved PL measurements also support a “free-to-bound” recombination model in which the hole is the deeply trapped carrier.<sup>181,194</sup> This proposed “free-to-

bound” recombination of a CB electron with a localized hole is similar to the PL mechanism of copper-doped semiconductor NCs, except that the hole in CuInS<sub>2</sub> and CuInSe<sub>2</sub> NCs is proposed to localize at a point defect.<sup>77,127</sup> As in the DAP mechanism, some reports have suggested copper vacancies (V<sub>Cu</sub>) as the likely hole traps based on the similarity between the depth of the V<sub>Cu</sub> acceptor state in bulk and the depth of the hole trap in the NCs, as well as the observation that the PL QY is generally higher for copper-deficient CuInS<sub>2</sub> NCs compared to stoichiometric CuInS<sub>2</sub> NCs.<sup>73,77,127</sup> It has also been proposed that the DAP and “free-to-bound” mechanisms coexist as competitive recombination pathways in CuInS<sub>2</sub> NCs, with the dominant mechanism determined by the NC stoichiometry and whether the NC is shelled.<sup>127,173,177</sup> Overall, several studies agree upon the general description of CuInS<sub>2</sub> and CuInSe<sub>2</sub> NC PL as a “free-to-bound” recombination involving a delocalized CB electron and a hole localized at a point defect.<sup>71,73,77,174,181,194</sup>

A few reports assign the PL in CuInS<sub>2</sub> NCs to a “free-to-bound” recombination in which the electron is localized at a point defect and the hole is delocalized in the VB.<sup>92,179,182,183</sup> One of these studies bases the assignment of the electron as the localized carrier on DFT calculations of the energies of defect states in wurtzite CuInS<sub>2</sub> NCs that identify In<sub>i</sub> as an appropriate donor defect.<sup>182</sup> Another study assigns the electron as the localized carrier based on ultrafast transient absorption measurements in which a ~0.5-ps decay component was observed in a broad excited-state absorption feature centered at a lower energy than the PL, but was not observed in the recovery dynamics of the ground-state bleach.<sup>183</sup> Three-pulse “pump-dump-probe” experiments confirmed that this excited-state absorption is not associated with the emissive excited state.<sup>183</sup> Although the authors attributed this 0.5-ps decay to formation of the emissive excited state *via* nonradiative electron trapping to a donor defect (In<sub>Cu</sub>),<sup>183</sup> the alternative assignment to hole localization also appears consistent with all of the reported observations, including the lack of a corresponding 0.5-

ps component in the ground-state-bleach recovery, a spectral feature known to reflect the population of CB electrons.<sup>71,180,181</sup> In summary, studies that assign the PL in CuInS<sub>2</sub> and CuInSe<sub>2</sub> NCs to “free-to-bound” recombination generally suggest the same point defects as found in bulk,<sup>116,171</sup> particularly V<sub>Cu</sub>, as the site of hole localization and In<sub>i</sub> or In<sub>Cu</sub> as the site of electron localization.

A theoretical study of the band structure of small CuInS<sub>2</sub> NCs based on the multi-band effective-mass approximation proposes a different PL mechanism that does not invoke defects.<sup>195</sup> From these calculations, the authors account for the large Stokes shift and long PL lifetimes in quantum-confined CuInS<sub>2</sub> NCs by noting that the first inter-band electronic transition is formally symmetry forbidden and only becomes weakly allowed due to the low-symmetry crystal structure. In this scenario, the first allowed inter-band absorption transition occurs between a deeper VB level and the lowest-energy CB level, while PL occurs *via* the lower-energy weakly allowed excitonic recombination, accounting for the large intrinsic Stokes shift.<sup>195</sup> The distinguishing feature of this description is that it does not invoke carrier trapping, although the authors still associate the PL of large CuInS<sub>2</sub> NCs (which extends to energies below the bulk bandgap) to recombination involving copper vacancies.<sup>195</sup> This model does not directly account for the large intrinsic PL bandwidths observed experimentally, however.

The striking similarities in PL bandwidths, Stokes shifts, lifetimes, and MCPL between CuInS<sub>2</sub> and copper-doped semiconductor NCs has led to suggestions that a similar microscopic mechanism is responsible for the PL of both classes of materials. One possibility suggested recently is that both classes of NCs possess the same lattice defects (*e.g.*, ground-state Cu<sup>2+</sup> defects in both),<sup>72,174</sup> allowing both to show the same free-to-bound recombination. The similarity in the absorption spectra of the copper-doped and copper-based NCs points to an alternative suggestion,

namely that CuInS<sub>2</sub> NCs behave like heavily copper-doped NCs, showing MLCBCT recombination of CB electrons with holes localized at Cu<sup>+</sup> lattice sites rather than defects.<sup>64</sup> In this interpretation, holes localize at lattice Cu<sup>+</sup> ions despite the translational crystallographic symmetry of the lattice in the process referred to as exciton self-trapping (see Figure 21).<sup>64,196-199</sup> Exciton self-trapping has been studied extensively in several bulk and nanoscale semiconductors, particularly AgCl.<sup>198,200,201</sup> Self-trapping is induced by strong electron-phonon coupling that allows one of the exciton's carriers (the hole in the case of CuInS<sub>2</sub> NCs) to be stabilized dramatically by a local lattice distortion. Like in the copper-doped NCs, large electron-phonon coupling in CuInS<sub>2</sub> NCs likely involves Jahn-Teller coupling, which is particularly strong for Cu<sup>2+</sup>, in addition to a strong coupling with a totally symmetric local distortion (see Figure 19). As illustrated in Figure 21, the large excited-state nuclear distortion associated with hole self-trapping in CuInS<sub>2</sub> NCs leads directly to the broad PL bandshape and large Stokes shift that characterize these NCs. Notably, this proposed self-trapping mechanism does not require lattice defects (vacancies, interstitials),<sup>64</sup> which differentiates it from previous interpretations.<sup>72,92,116,189,190</sup> The ability of all lattice copper ions to participate similarly in hole trapping is reflected in the similar per-copper extinction coefficients at the absorption edges of CuInS<sub>2</sub> and Cu<sup>+</sup>-doped NCs (Figure 16), as well as in the robustness of the characteristic PL properties across a range of lattice copper concentrations spanning the stoichiometric CuInS<sub>2</sub> and dilute Cu<sup>+</sup>-doped NC limits. The relatively large low-energy extinction coefficients of CuInS<sub>2</sub> NCs are otherwise difficult to reconcile with proposals of PL involving rare point defects.

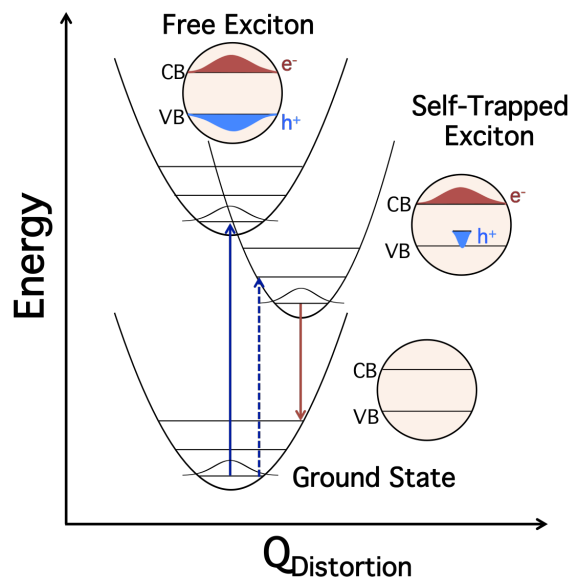


**Figure 21.** Qualitative single-configuration-coordinate diagram illustrating absorption, exciton self-trapping, and luminescence in CuInS<sub>2</sub> NCs. Absorption of a photon (blue arrow) excites a CuInS<sub>2</sub> NC from its ground state to a delocalized excitonic state. This “free” excitonic state rapidly relaxes to a self-trapped excitonic state *via* hole localization at a Cu<sup>+</sup> site induced by strong vibronic coupling and a resulting nuclear distortion. Luminescence from this self-trapped excitonic state to the ground state (solid red arrow) is characterized by a large Stokes shift and a vibronically broadened bandshape. Direct excitation of the self-trapped excitonic state (dashed blue arrow) is observed as a comparably broad, low-extinction “foot” in the absorption spectrum. Adapted with permission from ref. <sup>64</sup>. Copyright 2015 American Chemical Society.

The above discussion raises an interesting unanswered question: why would the PL of CuInS<sub>2</sub> NCs be dominated by exciton self-trapping when the PL of bulk CuInS<sub>2</sub> is dominated by carrier localization at point defects? One hypothesis may be that the stability of the self-trapped exciton relative to the delocalized exciton is size-dependent.<sup>64</sup> According to this hypothesis, as the NC volume increases, the kinetic energy favoring hole delocalization increases, causing the self-trapped exciton to become less stable relative to the delocalized exciton. Eventually, the energies of these two states could cross, causing the material to revert to bulk-like behavior. A related hypothesis is that the self-trapping energies are greater in CuInS<sub>2</sub> NCs than in bulk CuInS<sub>2</sub> because of the greater deformability of the NC lattices relative to bulk, associated with the very large

surface-to-volume ratios of the NCs. Lattice deformability is a key prerequisite of exciton self-trapping.<sup>196-199</sup> DFT calculations of Cu<sup>+</sup>:CdSe NCs do indeed show deeper hole trapping at copper ions located closer to the NC surfaces.<sup>95</sup> Other reasonable hypotheses can also be formulated, and additional experiments are needed to test the viability of the exciton self-trapping mechanism in CuInS<sub>2</sub> and related NCs.

#### 4.4. The Roles of Trap States

Although the copper ions that localize holes to form the luminescent G-Cu-type ML<sub>CBCT</sub> excited states of copper-doped or copper-based semiconductor nanocrystals are essentially well-defined "engineered" hole traps, other electron or hole traps can also affect the PL of these NCs. For example, in addition to the characteristic G-Cu luminescence ( $\lambda_{em} \sim 450-500$  nm) typically observed in copper-doped ZnS nanocrystals,<sup>35,36,38,39</sup> a red luminescence feature ( $\lambda_{em} \sim 600$  nm) has also been observed in some cases (Figure 22A).<sup>37</sup> The PLE spectrum for this red luminescence (Figure 22A) peaks at 345 nm, confirming that it indeed comes from nanocrystal excitation. Figure 22B shows that the red emission becomes more prominent than the green emission at high temperatures (> 220 K). By analogy to bulk, the red emission is assigned to recombination involving an electron localized in a deep trap and a hole localized at copper. Heating apparently increases the concentration of deeply trapped electrons contributing to the red luminescence,<sup>37</sup> which are described in bulk as electrons localized at S<sup>2-</sup> vacancies (V<sub>S</sub>).<sup>146</sup> Similarly, an orange emission observed in copper-doped ZnS nanorods has been assigned to recombination of a deeply trapped electron with a copper-localized hole.<sup>202</sup> The green and red luminescence mechanisms thus differ only in whether the electron originates from the conduction band or a mid-gap trap. The observation of both green and red luminescence illustrates that, as in bulk, more than one

luminescence mechanism involving copper-bound holes may be active within the same ensemble of copper-doped semiconductor NCs.

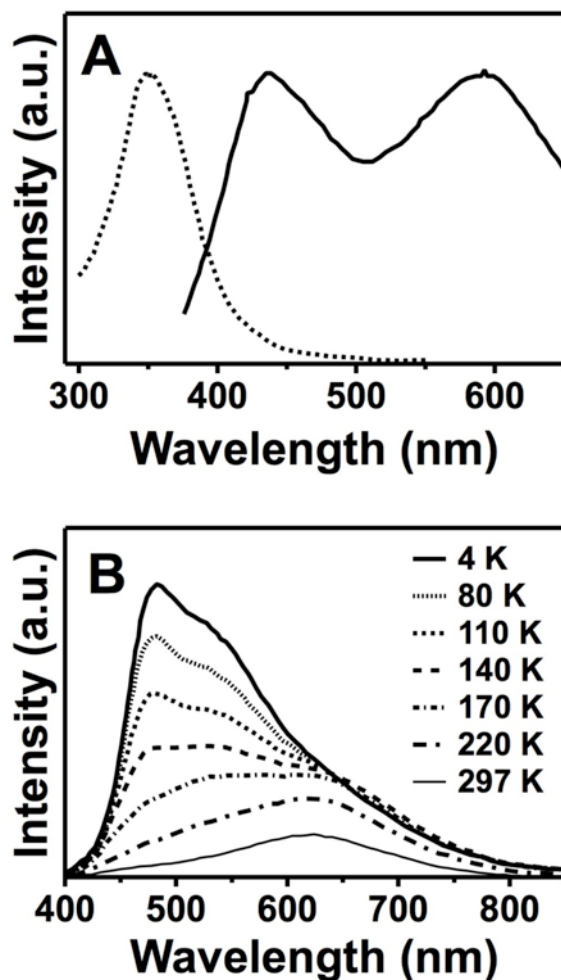


**Figure 22.** (A) Emission (solid) and PL excitation (dashed) spectra of copper-doped ZnS nanocrystals ( $d = 4.1$  nm) at room temperature. The emission spectrum was measured with an excitation wavelength of 345 nm and the excitation spectrum was measured for 600-nm emission. (B) Temperature-dependent emission spectra ( $\lambda_{\text{exc}} = 352$  nm) of heat-treated (10 min at 450 °C in  $\text{N}_2$  atmosphere) copper-doped ZnS nanocrystals ( $d = 7.4$  nm) measured from 4 to 297 K. Adapted with permission from ref. <sup>37</sup>. Copyright 2002 Elsevier.

Although difficult to characterize, the existence of various deep electron traps in copper-doped NCs is known from several observations. For example, using magnetic circular dichroism (MCD) spectroscopy, a photoinduced meta-stable state was detected in copper-doped ZnSe/CdSe core/shell NCs.<sup>203</sup> Band-edge MCD intensities were observed to increase upon illumination of

these NCs with 405-nm light (Figure 23A). This signal decays back to its pre-illumination intensity when the 405-nm source is turned off (Figure 23B). The decay rate depends on the intensity of the probe beam at 578 nm (Figure 23C), with lower fluence resulting in slower decay. Figure 23D illustrates the results of an experiment in which both the probe beam and 405-nm illumination were blocked for 70 min after the initial illumination period, then the probe was unblocked to measure the MCD signal. The photoinduced MCD intensity was still greater than half its initial value after the sample sat in the dark for 70 min. The authors demonstrated that the external magnetic field was not necessary to generate the metastable state by performing the 405-nm illumination and then turning on the field for the MCD measurement (Figure 23E). The authors interpreted the increase in excitonic MCD with 405-nm excitation in terms of photo-conversion of non-magnetic copper dopants to long-lived paramagnetic  $\text{Cu}^{2+}$  ions, which can participate in *sp-d* exchange with excitons and thereby enhance the excitonic MCD signal.<sup>203</sup> Careful measurements did not reveal any associated variations in the PL intensity, which was taken as evidence against  $\text{Cu}^+$  to  $\text{Cu}^{2+}$  conversion by 405-nm excitation. Regardless of interpretation, the data demonstrate the formation of long-lived photogenerated states in copper-doped NCs, presumably associated with carrier localization at deep traps.

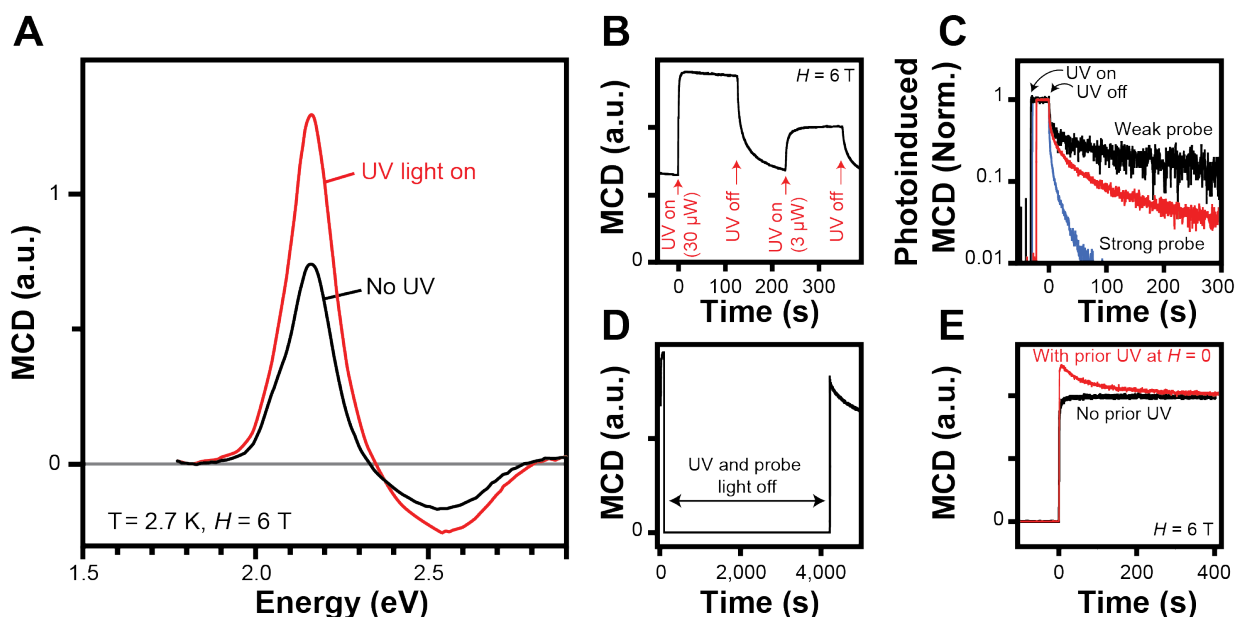


**Figure 23.** A) MCD spectra of copper-doped ZnSe/CdSe core/shell NCs measured at 2.7 K and 6 T. The magnitude of the signal at 2.15 eV, which is associated with the first excitonic transition, increases when illuminated by additional continuous-wave 405-nm excitation. B) Plot of the intensity of the excitonic MCD signal versus time demonstrating that the MCD signal increases when illuminated with 405 nm light, and decays when the extra illumination is turned off. The magnitude of the photoinduced enhancement in the MCD signal is correlated with the intensity of the 405-nm excitation. C) The rate of decay of the photoinduced MCD signal depends on the intensity of the probe light that is used to measure MCD. A low intensity probe (black) shows a slower decay to the new equilibrium than a high intensity probe (blue). D) After excitation at 405 nm, the nanocrystals were kept in complete darkness for about 70 minutes. The magnitude of the MCD signal after this time was still greater than that observed before illumination with the 405-nm source. (E) Copper-doped ZnSe/CdSe NCs that were illuminated at 405 nm and 0 T showed enhanced MCD at 6 T compared with NCs that were not pre-illuminated with 405 nm at 0 T. Adapted with permission from ref. <sup>203</sup>. Copyright 2012 Macmillan Publishers Ltd.

Signatures of metastable charge-separated states have also been observed in Cu<sup>+</sup>:CdSe NCs using PL spectroscopy.<sup>16</sup> Figure 24C shows PL decay traces of Cu<sup>+</sup>:CdSe NCs measured over a 1.6 s window at 20 and 297 K. In addition to the typical prompt PL decay on the single-microsecond timescale, a smaller but pronounced component of the PL decayed with an extremely large time constant (~3.5 ms at room temperature, ~300 ms at 20 K), extending the total PL decay well beyond its radiative lifetime.<sup>16</sup> Similar delayed luminescence has also been observed in undoped CdSe and related nanocrystals,<sup>204-206</sup> but the phenomenon is more pronounced in the Cu<sup>+</sup>:CdSe NCs.

The delayed luminescence was attributed to the formation of metastable charge-separated states involving a copper-bound hole and an electron localized in a surface trap.<sup>16</sup> Slow de-trapping of the electron allows the luminescence to decay on a very slow timescale. This process is a nanoscale analog of the donor-acceptor pair afterglow observed in bulk copper-doped ZnS,<sup>12,207</sup> except nanocrystal surface traps play the role of the bulk lattice co-dopants.

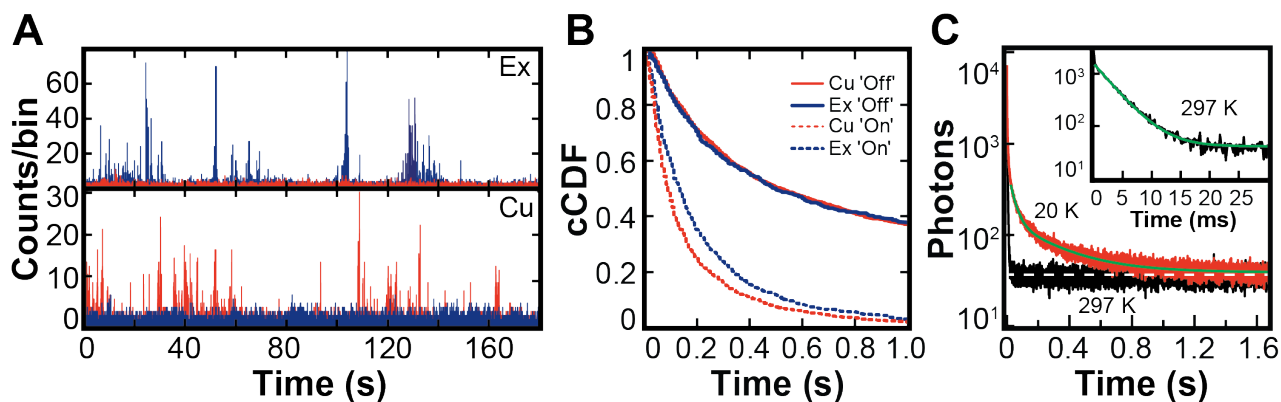


**Figure 24.** **A**) Single-nanocrystal blinking traces documenting emission from 490 - 635 nm (blue) and from 635 nm - 950 nm (red) for a single nanocrystal that exhibits only excitonic emission (Ex), and a single nanocrystal that exhibits only copper-based emission (Cu). **B**) Linear plot of "on" (dashed lines) and "off" (solid lines) complementary cumulative distribution functions (cCDFs) for excitonic (blue) and copper-based (red) emission. **C**) PL decay measured for an ensemble of Cu<sup>+</sup>:CdSe nanocrystals at 20 K (red) and 297 K (black). The inset shows the decay measured at 297 K plotted over a 30 ms time window. In addition to the dominant prompt decay on the single-microsecond time scale, a very slow component is observed that has a time constant of 3.5 ms at 297 K and 300 ms at 20 K. The exponential fits used to extract these time constants are plotted in green. Adapted with permission from ref. <sup>16</sup>. Copyright 2015 American Chemical Society.

This delayed luminescence was related to the nanocrystal luminescence intermittency. Using complementary cumulative distribution functions (cCDFs) to compare single-particle blinking statistics in Cu<sup>+</sup>:CdSe and undoped CdSe NCs within the same sample, the authors concluded that electron (rather than hole) trapping/de-trapping was responsible for the observed blinking dynamics in both types of NCs.<sup>16</sup> Figures 24A and 24B summarize the single-particle blinking data reported in this study. The indistinguishable "off" statistics for the doped and undoped NCs (Figure

24B) imply that both turn back “on” *via* the same carrier-de-trapping processes, but the different “on” statistics implicate different carrier-trapping probabilities. The longer “on” intervals observed in the CdSe NCs compared to the Cu<sup>+</sup>:CdSe NCs are consistent with “off” states arising from electron trapping, because Cu<sup>+</sup>:CdSe MLCBCT luminescence decay is intrinsically approximately an order of magnitude slower than CdSe excitonic luminescence decay ( $\tau_{\text{Cu}} \sim 300 \text{ ns}^{16,64}$  compared to  $\tau_{\text{Exc}} \sim 10\text{-}50 \text{ ns}^{208\text{-}210}$  at room temperature). The alternative scenario of blinking dynamics governed by hole trapping/de-trapping would cause shorter “on” intervals in CdSe compared to Cu<sup>+</sup>:CdSe because hole trapping in CdSe does not have to compete with hole transfer to Cu<sup>+</sup> and is therefore more probable. This interpretation is consistent with the interpretation of the delayed luminescence as involving reversible electron trapping at the NC surfaces. It was thus proposed that the same microscopic trapping/de-trapping processes are responsible for both the delayed luminescence and the PL blinking in these NCs.<sup>16</sup> Delayed luminescence and PL intermittency have been linked in other studies of undoped NCs.<sup>204-206</sup>

## 5. Applications

Due to their tunable absorption and emission spectra, their large effective Stokes shifts, their generally high extinction coefficients, and their moderate to high PL QYs, copper-doped and copper-based semiconductor NCs can be potentially useful as optically active components in applications such as bio-imaging, solid-state lighting, and solar energy conversion.<sup>88,89,93</sup> Some copper-containing nanocrystals, such as copper-doped ZnSe or InP, and CuInS<sub>2</sub>, have the added advantage of containing only nontoxic elements. One of the most promising practical applications for colloidal copper-based NCs such as CuInS<sub>2</sub>,<sup>211,212</sup> CuInSe<sub>2</sub>,<sup>211,213,214</sup> CuIn<sub>1-x</sub>Ga<sub>x</sub>S<sub>2</sub>,<sup>211,215-218</sup> and Cu<sub>2</sub>ZnSn(S<sub>1-x</sub>Se<sub>x</sub>),<sup>81,83,219</sup> is their use as “inks” for the fabrication of solution-processed photovoltaic cells, which has been reviewed extensively elsewhere.<sup>220,221</sup> Here, we focus on applications that rely on the PL

properties of colloidal copper-containing NCs, namely bio-imaging applications, solid-state lighting, and luminescent solar concentration.

### 5.1. Bio-Imaging

One of the most important applications for luminescent nanocrystals is in the imaging of biological systems,<sup>222-224</sup> where they have been used in a variety of ways from tagging specific cells<sup>224</sup> to *in situ* nanothermometry.<sup>225</sup> To be useful as fluorescent probes for *in vitro* or *in vivo* imaging, luminescent nanocrystals need to meet several requirements. Desired properties include non-toxicity, aqueous dispersibility, photostability, large Stokes shifts, and high luminescence QYs.<sup>226</sup> Long luminescence lifetimes (hundreds of nanoseconds) are helpful for biolabeling applications because they facilitate reduction of autofluorescence background signals from the biological sample, which usually cause strong interference in just the first tens of nanoseconds following photoexcitation.<sup>128</sup> CuInS<sub>2</sub> and cadmium-free copper-doped semiconductor NCs fulfill all of these requirements, and there have been several reports of their biomedical and bioimaging applications.<sup>97,128,227-231</sup>

Copper-doped zinc-based NCs have much lower cytotoxicity than cadmium-based NCs.<sup>51,230,231</sup> Figure 25 describes the use of copper-doped ZnSe/ZnS core/shell NCs for imaging HeLa cells.<sup>51</sup> In Figure 25A, the cytotoxicity of copper-doped ZnSe/ZnS NCs is compared to that of CdTe NCs. Both copper-doped ZnSe/ZnS NCs and CdTe NCs were purified to exclude excess ions in solution before the cell viability experiments were performed using HeLa cells. The cell viability decreases with increasing CdTe NC concentration, whereas no obvious alteration of viability is observed for copper-doped ZnSe/ZnS NCs. These results suggest that the cytotoxicity of copper-doped ZnSe/ZnS NCs is much smaller than that of CdTe NCs. The low cytotoxicity of copper-doped ZnSe/ZnS NCs makes them suitable for imaging living cells, as demonstrated in Figures 25B and

25C. The presence of the ZnS shell greatly improves the photostability of the NCs, and no obvious PL decrease is observed even after heating the sample at 60 °C for 170 hours.<sup>51</sup> Alloying copper-doped ZnS NCs with indium provides additional PL tunability throughout the visible region, and in particular allows the PL of these systems to access the far-red region of the visible spectrum, which is more desirable for bio-imaging applications (see below).<sup>230,231</sup> Addition of folic acid or antibodies to the surfaces of Cu:Zn-In-S/ZnS alloyed NCs enabled targeted imaging of HeLa cells, which have large concentrations of folate receptors,<sup>230</sup> and liver cancer cells,<sup>231</sup> respectively.

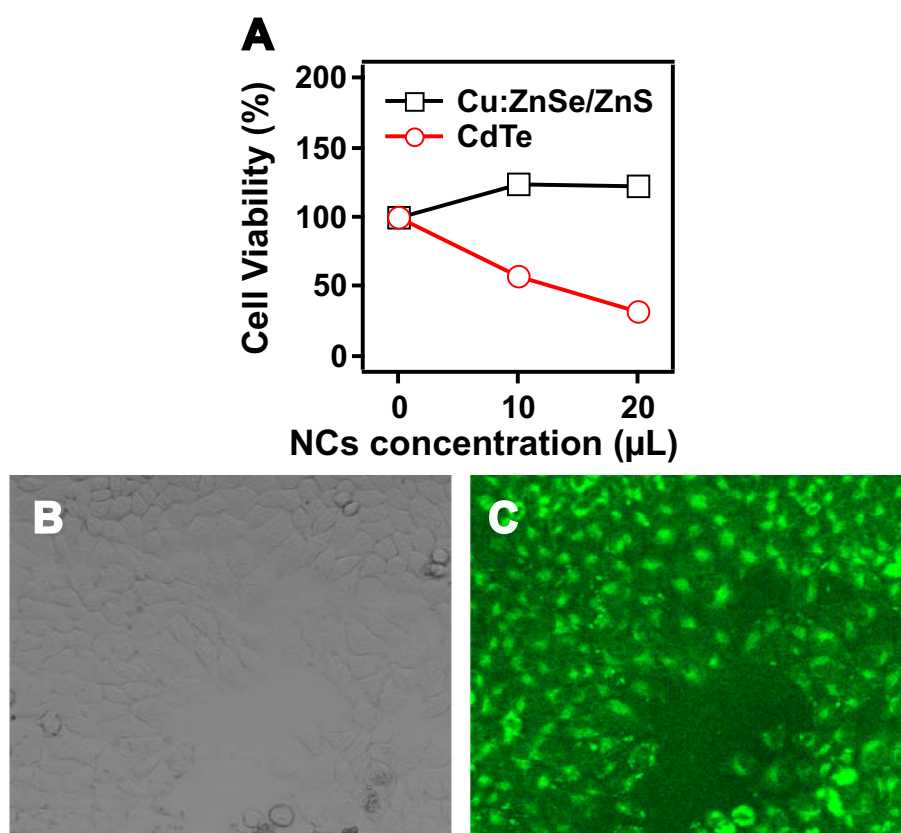


**Figure 25.** **A)** Plot of viability of HeLa cells versus concentration of added copper-doped ZnSe/ZnS NCs (black squares) and CdTe NCs (red circles). **B)** Image of living HeLa cells stained by copper-doped ZnSe/ZnS NCs in an optical microscope. **C)** Corresponding PL image with an excitation wavelength of 458 nm. Adapted with permission from ref. <sup>51</sup>. Copyright 2011 IOP Publishing.

CuInS<sub>2</sub>/ZnS core/shell nanoparticles are also very attractive bio-imaging agents due to their low toxicity and the ability to tune their luminescence throughout the biologically desirable red/near-

infrared window of 650-900 nm.<sup>93,128</sup> Imaging agents that emit at these wavelengths are especially important for *in vivo* imaging because absorption from water, hemoglobin, and other biological molecules is minimal in this spectral window.<sup>232</sup> There are several reports of the use of CuInS<sub>2</sub>/ZnS NCs for both *in vitro* imaging of HeLa and other types of cancer cells,<sup>227,228,233</sup> and *in vivo* imaging of model organisms such as mice<sup>28,234</sup> and *C. elegans*.<sup>233</sup> All of these studies highlight the importance of growing ZnS shells on the CuInS<sub>2</sub> NCs in order to maintain a sufficiently high PL QY throughout the ligand exchange and bio-conjugation procedures used to impart water-solubility and cell-binding or targeting functionality to the NCs. The presence of the ZnS shell also promotes long-term PL stability in *in vivo* imaging experiments, with PL still detectable up to 96 h after injection.<sup>233</sup> As with the Cu<sup>+</sup>-doped NCs, surface functionalization of CuInS<sub>2</sub>/ZnS NCs enables targeting of specific cells. These strategies for targeted imaging have been successfully demonstrated for both *in vitro* imaging of cancer cells<sup>227,228</sup> and *in vivo* imaging of brain glioblastoma tumors in mice.<sup>227</sup> Surface-bound Gd<sup>3+</sup> molecular complexes have also been added to CuInS<sub>2</sub>/ZnS NCs to impart magnetic resonance imaging capabilities that complement their fluorescence imaging functionality.<sup>228</sup> All reported evaluations of the toxicity of CuInS<sub>2</sub>/ZnS NCs have found them to be highly biocompatible. *In vitro* cytotoxicity studies show >90% of various cells remain viable after 24-72 h of exposure to CuInS<sub>2</sub>/ZnS NCs.<sup>228,233</sup> A side-by-side comparison of the *in vivo* toxicity of CdSe<sub>1-x</sub>Te<sub>x</sub>/ZnS and CuInS<sub>2</sub>/ZnS NCs, as measured by the inflammation of lymph nodes in mice upon NC injection, found that a dose of CuInS<sub>2</sub>/ZnS NCs ten times larger than that of CdSe<sub>1-x</sub>Te<sub>x</sub>/ZnS NCs was required to cause the same level of lymph node inflammation.<sup>233</sup> Overall, the low toxicity, large Stokes shifts, and high QYs of many copper-doped and copper-based NCs make them attractive for bio-imaging applications.

## 5.2. Light-Emitting Diodes

The low toxicity, visible PL, and large Stokes shift of cadmium-free copper-doped ZnS, CuInS<sub>2</sub>, and CuInSe<sub>2</sub> NCs also make them attractive as spectral converters for light-emitting diodes (LEDs).<sup>88,89,93</sup> Copper-doped ZnS nanocrystal/polymer composites were first reported as the emissive layer in blue-green-emitting electroluminescent devices in the late 1990s.<sup>235,236</sup> More recently, copper-doped Zn-In-S/ZnS alloyed core/shell,<sup>98</sup> CuInSe<sub>2</sub>/ZnS,<sup>124</sup> CuInS<sub>2</sub>/ZnS,<sup>126</sup> and CuInS<sub>2</sub>/ZnSe/ZnS core/shell NCs<sup>237</sup> have been used to make green, yellow, orange, and red LEDs. Growth of ZnS shells on the Zn-In-S and CuInS<sub>2</sub> NCs can result in PL QYs up to 80%,<sup>98,238-240</sup> and color tunability of the PL in both of these systems is achieved by a combination of NC size and composition tuning, as discussed in Section 2.1. For the Cu:Zn-In-S system, increasing the Zn/In ratio results in higher-energy PL.<sup>98</sup> Similarly, alloying with ZnS during shell growth shifts the luminescence of CuInS<sub>2</sub> NCs to higher energies.<sup>126,237-241</sup> Notably, most of the reports of LEDs based on CuInS<sub>2</sub>/ZnS NCs use copper-deficient CuInS<sub>2</sub> NCs, with Cu:In ratios as small as 1:6,<sup>126,238-240</sup> that emit at higher energies than stoichiometric CuInS<sub>2</sub> NCs of comparable sizes. This copper deficiency combined with alloying during shell growth makes these CuInS<sub>2</sub>/ZnS core/shell NCs very similar in composition to copper-doped Zn-In-S/ZnS alloyed core-shell nanocrystals.

Although LEDs of several different single colors have been made using luminescent copper-based NCs, their broad PL bandwidths make them better suited to play the role of the green or red emitters used in conjunction with blue LEDs to form white LEDs.<sup>67,238-241</sup> To achieve white light of high enough quality to replace conventional white light bulbs, the green and red emissions in a white LED must be broad and their relative intensities carefully tuned. Figure 26C shows the electroluminescence spectrum of a white LED containing a mixture of green- and red-emitting CuInS<sub>2</sub>/ZnS NCs. This device has a color rendering index (CRI) of ~95 and a luminous efficiency of ~69 lm/W.<sup>241</sup> An ideal white-light source, such as the sun, has a CRI value of 100.<sup>242</sup> The

CuInS<sub>2</sub>/ZnS white LED shown in Figure 26 has the highest CRI value reported for any NC-based white LED,<sup>241</sup> and a luminous efficiency that is comparable to that of a commercial prototype white LED based on CdSe NCs.<sup>242</sup> CuInS<sub>2</sub>/ZnS NCs have also achieved a record color conversion efficiency of ~75% in a white LED.<sup>238</sup> Dual-emitting Cu:InP/ZnS/InP/ZnS core/barrier/quantum-well/shell NCs, in which the relative intensities of the copper-based emission of the NC core and the higher-energy emission of the InP quantum well can be tuned by controlling the thicknesses of the ZnS barrier and shell layers, were recently developed for white LED applications.<sup>67</sup> Optimizing the energies of the core copper-based emission and the InP quantum well emission in these heterostructured NCs by controlling the core size and the thickness of the quantum well layer, respectively, enabled fabrication of white LEDs with a CRI of 91.<sup>67</sup>

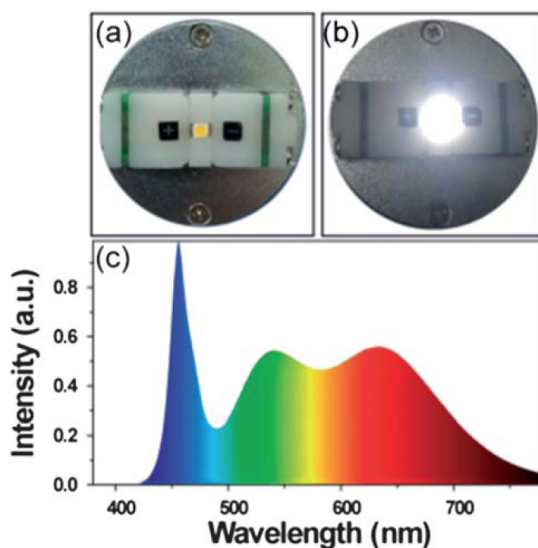


**Figure 26.** Photographs of (A) a white LED comprising a mixture of green- and red-emitting CuInS<sub>2</sub>/ZnS NCs embedded in a silicone resin and deposited on top of an InGaN-based blue LED, and (B) the same white LED under an applied forward bias current of 20 mA. (C) Electroluminescence spectrum of the device shown in (A) and (B) operated at 20 mA. The narrow peak at ~460 nm in the electroluminescence spectrum is from the blue InGaN LED and the two peaks at ~540 nm and ~630 nm correspond to the green- and red-emitting CuInS<sub>2</sub>/ZnS NCs, respectively. Adapted with permission from ref. <sup>241</sup>. Copyright 2013 Royal Society of Chemistry.

### 5.3. Luminescent Solar Concentrators

Several recent reports have recognized that the combination of large Stokes shifts and PL tunability displayed by copper-based semiconductor nanocrystals makes them attractive luminophores for luminescent solar concentrators (LSCs).<sup>174,243-246</sup> LSCs are devices that collect sunlight over a large area and concentrate its energy onto small-area PV cells. This process is achieved by absorption of solar photons followed by emission into a waveguide structure that directs photons onto the appended PVs.<sup>247-250</sup> Figure 27D illustrates a common LSC device architecture comprising a planar waveguide with embedded luminophores that absorb solar photons and re-emit lower-energy photons. LSCs can potentially lower the cost of solar energy,<sup>250,251</sup> but commercially viable LSC technologies have not yet been realized due to the persistence of several loss mechanisms that limit their efficiencies.<sup>248,250</sup> Reabsorption of emitted photons by the luminophores is a particularly detrimental loss pathway because reabsorption compounds other loss mechanisms such as nonradiative decay and emission at angles that do not lead to total internal reflection (*i.e.*, escape-cone losses).<sup>250-252</sup>

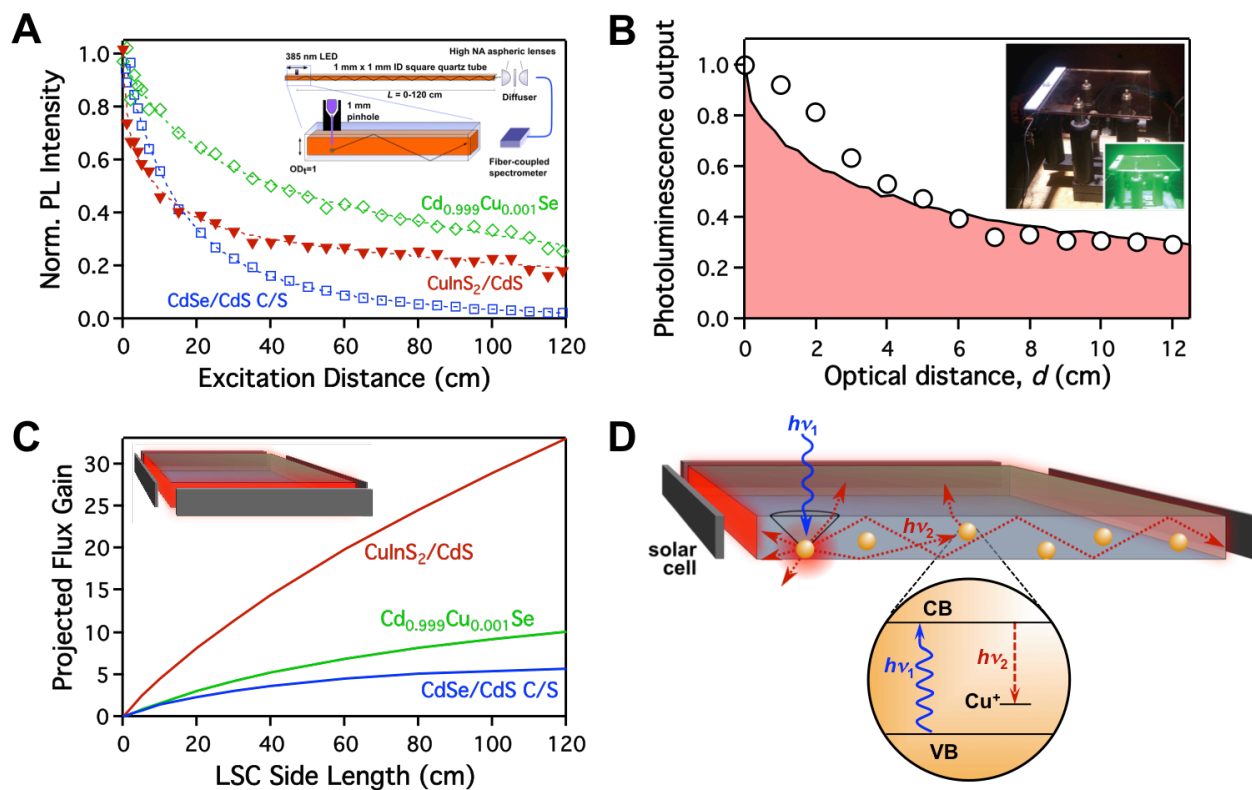


**Figure 27.** **A)** Plot of the normalized PL intensity measured at the end of a 120-cm long liquid waveguide versus excitation distance for solutions of  $\text{Cd}_{0.999}\text{Cu}_{0.001}\text{Se}$  (green diamonds),  $\text{CuInS}_2/\text{CdS}$  (red triangles), and  $\text{CdSe}/\text{CdS}$  core/giant shell (blue squares) NCs with transverse optical densities of  $\text{OD}_t = 1.0$  at the band-edge. Adapted with permission from ref. <sup>244</sup>. Copyright 2015 Royal Society of Chemistry. The inset shows a diagram of the experimental setup for the “1D LSC”. Adapted with permission from ref. <sup>243</sup>. Copyright 2015 American Chemical Society. **B)** Plot of the normalized PL intensity measured from one edge of a 12 cm x 12 cm x 0.3 cm LSC containing a  $\text{CuInSe}_x\text{S}_{2-x}/\text{ZnS}$  nanocrystal/polymer composite (open circles) and calculated from a Monte Carlo ray tracing simulation for the same LSC assuming a quantum yield of 40% (black line with red shading). The inset shows photographs of the experimental setup taken with both conventional and infrared cameras. Adapted with permission from ref. <sup>174</sup>. Copyright 2015 Macmillan Publishers Ltd. **C)** Projected flux gains of two-dimensional square LSCs of various side lengths containing the same nanocrystal samples with the same  $\text{OD}_t$  as shown in (A). Adapted with permission from ref. <sup>244</sup>. Copyright 2015 Royal Society of Chemistry. **D)** Schematic illustrating a typical planar 2D LSC device and the mechanism of luminescence in embedded copper-based NC luminophores. The embedded luminophores (orange spheres) absorb incident photons of wavelength  $h\nu_1$  and re-emit them at wavelength  $h\nu_2$ . The re-emitted photons can be transported *via* total internal reflection to a solar cell attached to an edge of the device, lost through an escape cone, or reabsorbed by the luminophore. The mechanism of luminescence in copper-based NCs produces a large effective Stokes shift that minimizes reabsorption. Adapted with permission from ref. <sup>243</sup>. Copyright 2015 American Chemical Society.

Semiconductor NCs doped with luminescent transition-metal activator ions can almost completely eliminate reabsorption losses in LSCs.<sup>243,252</sup> The earliest demonstration of LSCs based on doped nanocrystals involved Mn<sup>2+</sup>-doped ZnSe/ZnS core/shell NCs as the phosphor.<sup>252</sup> The Mn<sup>2+</sup>-doped ZnSe/ZnS NCs used in this study have a fixed luminescence energy of ~2.1 eV, which is the energy of the Mn<sup>2+</sup> <sup>4</sup>T<sub>2</sub> → <sup>6</sup>A<sub>1</sub> ligand-field transition. This fixed PL energy restricts the bandgap of zero-reabsorption Mn<sup>2+</sup>-doped NC luminophores to ~480 nm, thereby defining the fraction of the solar spectrum such luminophores can absorb.<sup>243</sup> LSCs that almost exclusively absorb UV light are attractive as transparent window layers, for example. For broader spectral coverage, copper-doped and copper-based NCs are attractive because of their tunable electronic spectra that enable them to absorb a significantly greater fraction of the solar spectrum than Mn<sup>2+</sup>-doped NC phosphors, but with smaller reabsorption losses than undoped NC luminophores.<sup>243,244</sup> Critical for the proposed LSC applications is a quantitative description of the absorption, luminescence, reabsorption, and intrinsic losses from such nanocrystals, which can be achieved by spectroscopic analysis and modeling. An important aspect of such analyses is consideration of the relevant length scales: in contrast with PVs, in which the relevant electron-transport dimension is the short axis of the device, LSCs have as their relevant photon-transport dimension the long axes of the device. When photons are required to traverse the length of a standard multi-pane window, for example, the relevant transport distances are much larger than typically explored in the laboratory. For this reason, experimental examination of reabsorption and scattering losses over very long optical path lengths is valuable.

Figure 27A plots the normalized PL intensity collected from one end of a 120-cm long one-dimensional liquid waveguide with a 0.1 cm x 0.1 cm internal cross-section versus the distance between a translatable excitation source and the collection end of the waveguide.<sup>243,244</sup> The inset

contains a diagram of the experimental setup. The data summarize results for solutions of  $\text{Cd}_{0.999}\text{Cu}_{0.001}\text{Se}$ ,  $\text{CuInS}_2/\text{CdS}$ , and  $\text{CdSe}/\text{CdS}$  core/giant-shell NCs, each with a transverse optical density of  $\text{OD}_t = 1.0$  at the semiconductor band-edge. These “1D-LSC” measurements provide a means of directly comparing the reabsorption losses of various luminophores over length scales relevant to many proposed 2D-LSC applications.<sup>243</sup> The data in Figure 27A show that, of these three materials,  $\text{Cd}_{0.999}\text{Cu}_{0.001}\text{Se}$  NCs have the smallest reabsorption losses at all length scales, and the  $\text{CuInS}_2/\text{CdS}$  NCs have smaller reabsorption losses than  $\text{CdSe}/\text{CdS}$  NCs at photon transport distances greater than 20 cm. Recent characterization of reabsorption losses in a 12 cm x 12 cm x 0.3 cm 2D-LSC device comprising a  $\text{CuInSe}_x\text{S}_{2-x}/\text{ZnS}$  nanocrystal/polymer composite with  $\text{OD}_t \sim 0.2$  exhibited similar curvature (Figure 27B).<sup>174</sup> Despite the very large Stokes shifts of these materials, these curvatures are dominated by the existence of residual absorption-PL overlap.<sup>243,244</sup> Even small overlap leads to a high probability of reabsorption over such large photon-transport distances.

The overall performance of an LSC luminophore depends not only on reabsorption probability, but also on its PL QY and the fraction of the incident solar radiation it absorbs. Figure 27C plots projected flux gains for 2D LSCs containing the same NC samples characterized in Figure 27A.<sup>243,244</sup> The flux gain describes the factor by which an LSC increases the photon flux incident on an attached PV cell relative to the same PV cell under solar radiation.<sup>243,244,251,252</sup> The curves in Figure 27C show projected flux gains for square LSC devices of various side lengths. Although the  $\text{Cd}_{0.999}\text{Cu}_{0.001}\text{Se}$  NCs display smaller reabsorption losses than the  $\text{CuInS}_2/\text{CdS}$  NCs, the  $\text{CuInS}_2/\text{CdS}$  NCs have a much larger projected flux gain for all device dimensions due primarily to their much larger PL QY (86% for the  $\text{CuInS}_2/\text{CdS}$  NCs,<sup>244</sup> 27% for the  $\text{Cd}_{0.999}\text{Cu}_{0.001}\text{Se}$  NCs<sup>243</sup>). Both copper-containing NCs have larger predicted flux gains than the  $\text{CdSe}/\text{CdS}$  core/giant-shell

NCs because of the combination of smaller reabsorption losses and larger absorption overlap with the solar spectrum. The data shown in Figure 27 thus indicate that CuInS<sub>2</sub>-based NCs are the best-performing nanocrystal LSC luminophores synthesized to date, but with improved PL QYs, copper-doped semiconductor NCs with small bandgaps, such as Cu<sup>+</sup>:CdSe or Cu<sup>+</sup>:InP, will likely outperform CuInS<sub>2</sub> and related copper-based NCs.

## 6. Outlook

Advances in the synthesis of colloidal nanocrystals over the last 20 years have enabled the doping of copper ions into host nanocrystals of a wide variety of shapes and compositions, and provided access to various ternary and quaternary semiconductor nanocrystals containing copper. These synthetic achievements led to the observation of the broad, red-shifted PL associated with the copper ions. Spectroscopic and computational studies have identified the MLCBCT nature of this PL. Further synthetic developments are needed to improve the PL quantum yields of copper-doped semiconductor nanocrystals while maintaining high concentrations of copper ions. Such improvements in PL QY would not only improve the performance of luminescent copper-doped semiconductor NCs in various applications ranging from bio-imaging to solar concentration, but would also enable further fundamental investigations into the physical and photophysical properties of this important class of luminescent nanomaterials. Likewise, additional spectroscopic and physical characterization of copper-containing semiconductor nanocrystals will yield new fundamental insights into their luminescence mechanisms and redox or photo-redox properties, and ultimately their applicability in future advanced technologies.

## Acknowledgments

Financial support from the U.S. National Science Foundation (Graduate Research Fellowships DGE-1256082 to K.H.H. and H.D.N., and DMR-1505901 to D.R.G.) is gratefully acknowledged. K.E.K. gratefully acknowledges the support of an Energy Efficiency and Renewable Energy (EERE) postdoctoral research award from the Department of Energy. A. M. gratefully acknowledges the support of an Early Postdoc Mobility Fellowship from the Swiss National Science Foundation.

### **Abbreviations**

CB	conduction band
CBM	conduction-band minimum
cCDF	complementary cumulative distribution function
CIS	CuInS <sub>2</sub>
CISE	CuInSe <sub>2</sub>
CRI	color rendering index
CZTS	Cu <sub>2</sub> ZnSnS <sub>4</sub>
CZTSSe	Cu <sub>2</sub> ZnSn(S <sub>1-x</sub> Se <sub>x</sub> ) <sub>4</sub>
DAP	donor-acceptor pair
DFT	density functional theory
EDS	energy-dispersive spectroscopy
EPR	electron paramagnetic resonance
EXAFS	extended X-ray absorption fine structure
fwhm	full-width at half-maximum
HOMO	highest occupied molecular orbital
ICP-AES	inductively coupled plasma atomic emission spectroscopy

KPS	potassium peroxydisulfate ( $K_2S_2O_8$ )
LED	light-emitting diode
$L_{VB}MCT$	ligand (valence band)-to-metal charge transfer
LSC	luminescent solar concentrator
LSPR	localized surface plasmon resonance
LUMO	lowest unoccupied molecular orbital
MCD	magnetic circular dichroism
MCPL	magnetic circularly polarized luminescence
$ML_{CB}CT$	metal-to-ligand (conduction band) charge transfer
NC	nanocrystal
NIR	near-infrared
NTO	natural transition orbital
PL	photoluminescence
PLE	photoluminescence excitation
PV	photovoltaic
QY	quantum yield
TEM	transmission electron microscopy
TOP	trioctylphosphine
VB	valence band
VBM	valence-band maximum
XANES	X-ray absorption near-edge structure
XAS	X-ray absorption spectroscopy
XPS	X-ray photoelectron spectroscopy

## References

- (1) *Phosphor Handbook*; Second ed.; Yen, W. M., Shionoya, S., Yamamoto, H., Eds.; CRC Press: New York, 2007.
- (2) Kröger, F. A.; Dikhoff, J. Trivalent Cations in Fluorescent Zinc Sulphide. *Physica* **1950**, *16*, 297-316.
- (3) van Gool, W. Fluorescence Centres in ZnS. *Philips Res. Rep., Suppl.* **1961**, *3*, 1-119.
- (4) Curie, D.; Prener, J. S. Deep Center Luminescence. In *Physics and Chemistry of II-VI Compounds*; Aven, M., Prener, J. S., Eds.; North-Holland Publishing Company: Amsterdam, 1967; pp 435-485.
- (5) Shionoya, S.; Koda, T.; Era, K.; Fujiwara, H. Nature of Luminescence Transitions in ZnS Crystals. *J. Phys. Soc. Jpn.* **1964**, *19*, 1157-1167.
- (6) Halsted, R. E.; Aven, M.; Coghill, H. D. Fluorescent Emission Spectra in II-VI Compounds. *J. Electrochem. Soc.* **1965**, *112*, 177-181.
- (7) Melamed, N. T. Energy Transfer in ZnS:Cu:Cl Phosphors. *J. Phys. Chem. Solids* **1958**, *7*, 146-152.
- (8) Klasens, H. A. On the Nature of Fluorescent Centers and Traps in Zinc Sulfide. *J. Electrochem. Soc.* **1953**, *100*, 72-80.
- (9) Prener, J. S.; Williams, F. E. Activator Systems in Zinc Sulfide Phosphors. *J. Electrochem. Soc.* **1956**, *103*, 342-346.
- (10) Thomas, D. G.; Hopfield, J. J.; Augustyniak, W. M. Kinetics of Radiative Recombination at Randomly Distributed Donors and Acceptors. *Phys. Rev.* **1965**, *140*, A202-A220.
- (11) Williams, F. E. Theory of the Energy Levels of Donor-Acceptor Pairs. *J. Phys. Chem. Solids* **1960**, *12*, 265-275.
- (12) Suzuki, A.; Shionoya, S. Mechanism of the Green-Copper Luminescence in ZnS Crystals. I. Direct Evidence for the Pair Emission Mechanism. *J. Phys. Soc. Jpn.* **1971**, *31*, 1455-1461.
- (13) Riehl, N. Tunnel Luminescence and Infrared Stimulation. *J. Lumin.* **1970**, *1,2*, 1-16.
- (14) Lehmann, W. Emission Spectra of (Zn,Cd)S Phosphors. *J. Electrochem. Soc.* **1963**, *110*, 754-758.
- (15) Reiss, P.; Couderc, E.; De Girolamo, J.; Pron, A. Conjugated Polymers/Semiconductor Nanocrystals Hybrid Materials - Preparation, Electrical Transport Properties and Applications. *Nanoscale* **2011**, *3*, 446-489.
- (16) Whitham, P. J.; Knowles, K. E.; Reid, P. J.; Gamelin, D. R. Photoluminescence Blinking and Reversible Electron Trapping in Copper-Doped CdSe Nanocrystals. *Nano Lett.* **2015**, *15*, 4045-4051.
- (17) Miller, M. T.; Gantzel, P. K.; Karpishin, T. B. A Highly Emissive Heteroleptic Copper(I) Bis(phenanthroline) Complex: [Cu(dbp)(dmp)]<sup>+</sup> (dbp = 2,9-Di-*tert*-butyl-1,10-phenanthroline; dmp = 2,9-Dimethyl-1,10-phenanthroline). *J. Am. Chem. Soc.* **1999**, *121*, 4292-4293.
- (18) Buckner, M. T.; McMillin, D. R. Photoluminescence from Copper(I) Complexes with Low-Lying Metal-to-Ligand Charge Transfer Excited States. *J. Chem. Soc., Chem. Commun.* **1978**, 759-761.
- (19) Blasse, G.; McMillin, D. R. On the Luminescence of Bis(Triphenylphosphine) Phenanthroline Copper (I). *Chem. Phys. Lett.* **1980**, *70*, 1-3.

- (20) Everly, R. M.; McMillin, D. R. Reinvestigation of the Absorbing and Emitting Charge-Transfer Excited States of  $[\text{Cu}(\text{NN})_2]^+$  Systems. *J. Phys. Chem.* **1991**, *95*, 9071-9075.
- (21) Everly, R. M.; Ziesel, R.; Suffert, J.; McMillin, D. R. Steric Influences on the Photoluminescence from Copper(I) Phenanthrolines in Rigid Media. *Inorg. Chem.* **1991**, *30*, 559-561.
- (22) Felder, D.; Nierengarten, J.-F.; Barigelletti, F.; Ventura, B.; Armaroli, N. Highly Luminescent Cu(I)-Phenanthroline Complexes in Rigid Matrix and Temperature Dependence of the Photophysical Properties. *J. Am. Chem. Soc.* **2001**, *123*, 6291-6299.
- (23) Iwamura, M.; Takeuchi, S.; Tahara, T. Real-Time Observation of the Photoinduced Structural Change of Bis(2,9-dimethyl-1,10-phenanthroline)copper(I) by Femtosecond Fluorescence Spectroscopy: A Realistic Potential Curve of the Jahn-Teller Distortion. *J. Am. Chem. Soc.* **2007**, *129*, 5248-5256.
- (24) Iwamura, M.; Watanabe, H.; Ishii, K.; Takeuchi, S.; Tahara, T. Coherent Nuclear Dynamics in Ultrafast Photoinduced Structural Change of Bis(diimine)copper(I) Complex. *J. Am. Chem. Soc.* **2011**, *133*, 7728-7736.
- (25) Iwamura, M.; Takeuchi, S.; Tahara, T. Ultrafast Excited-State Dynamics of Copper(I) Complexes. *Acc. Chem. Res.* **2015**, *48*, 782-791.
- (26) Waterland, M. R.; Howell, S. L.; Gordon, K. C.; Burrell, A. K. Structural Changes upon Photoexcitation into the Metal-to-Ligand Charge-Transfer State of  $[\text{Cu}(\text{pqx})(\text{PPh}_3)_2]^+$  Probed by Resonance Raman Spectroscopy and Density Functional Theory. *J. Phys. Chem. A* **2005**, *109*, 8826-8833.
- (27) Schimpf, A. M.; Ochsenbein, S. T.; Buonsanti, R.; Milliron, D. J.; Gamelin, D. R. Comparison of Extra Electrons in Colloidal n-Type  $\text{Al}^{3+}$ -Doped and Photochemically Reduced ZnO Nanocrystals. *Chem. Commun.* **2012**, *48*, 9352-9354.
- (28) Schimpf, A. M.; Knowles, K. E.; Carroll, G. M.; Gamelin, D. R. Electronic Doping and Redox-Potential Tuning in Colloidal Semiconductor Nanocrystals. *Acc. Chem. Res.* **2015**, *48*, 1929-1937.
- (29) Wei, W.; Lu, Y.; Chen, W.; Chen, S. One-Pot Synthesis, Photoluminescence, and Electrocatalytic Properties of Subnanometer-Sized Copper Clusters. *J. Am. Chem. Soc.* **2011**, *133*, 2060-2063.
- (30) Yuan, X.; Luo, Z.; Zhang, Q.; Zhang, X.; Zheng, Y.; Lee, J. Y.; Xie, J. Synthesis of Highly Fluorescent Metal (Ag, Au, Pt, and Cu) Nanoclusters by Electrostatically Induced Reversible Phase Transfer. *ACS Nano* **2011**, *5*, 8800-8808.
- (31) Wu, Z.; Liu, J.; Gao, Y.; Liu, H.; Li, T.; Zou, H.; Wang, Z.; Zhang, K.; Wang, Y.; Zhang, H.; Yang, B. Assembly-Induced Enhancement of Cu Nanoclusters Luminescence with Mechanochromic Property. *J. Am. Chem. Soc.* **2015**, *137*, 12906-12913.
- (32) Ling, Y.; Wu, J. J.; Gao, Z. F.; Li, N. B.; Luo, H. Q. Enhanced Emission of Polyethyleneimine-Coated Copper Nanoclusters and Their Solvent Effect. *J. Phys. Chem. C* **2015**, *119*, 27173-27177.
- (33) Barthel, M. J.; Angeloni, I.; Petrelli, A.; Avellini, T.; Scarpellini, A.; Bertoni, G.; Armirotti, A.; Moreels, I.; Pellegrino, T. Synthesis of Highly Fluorescent Copper Clusters Using Living Polymer Chains as Combined Reducing Agents and Ligands. *ACS Nano* **2015**, *9*, 11886-11897.
- (34) Singh, A.; Singh, S.; Levchenko, S.; Unold, T.; Laffir, F.; Ryan, K. M. Compositionally Tunable Photoluminescence Emission in  $\text{Cu}_2\text{ZnSn}(\text{S}_{1-x}\text{Se}_x)_4$  Nanocrystals. *Angew. Chem., Int. Ed.* **2013**, *52*, 9120-9124.

- (35) Khosravi, A. A.; Kundu, M.; Jatwa, L.; Deshpande, S. K.; Bhagwat, U. A.; Sastry, M.; Kulkarni, S. K. Green Luminescence from Copper Doped Zinc Sulphide Quantum Particles. *Appl. Phys. Lett.* **1995**, *67*, 2702-2704.
- (36) Sun, L.; Liu, C.; Liao, C.; Yan, C. ZnS Nanoparticles Doped with Cu(I) by Controlling Coordination and Precipitation in Aqueous Solution. *J. Mater. Chem.* **1999**, *9*, 1655-1657.
- (37) Bol, A. A.; Ferwerda, J.; Bergwerff, J. A.; Meijerink, A. Luminescence of Nanocrystalline ZnS:Cu<sup>2+</sup>. *J. Lumin.* **2002**, *99*, 325-334.
- (38) Peng, W. Q.; Cong, G. W.; Qu, S. C.; Wang, Z. G. Synthesis and photoluminescence of ZnS:Cu nanoparticles. *Opt. Mater.* **2006**, *29*, 313-317.
- (39) Corrado, C.; Jiang, Y.; Oba, F.; Kozina, M.; Bridges, F.; Zhang, J. Z. Synthesis, Structural, and Optical Properties of Stable ZnS:Cu,Cl Nanocrystals. *J. Phys. Chem. A* **2009**, *113*, 3830-3839.
- (40) Begum, R.; Sahoo, A. K.; Ghosh, S. S.; Chattopadhyay, A. Recovering Hidden Quanta of Cu<sup>2+</sup>-doped ZnS Quantum Dots in Reductive Environment. *Nanoscale* **2014**, *6*, 953-961.
- (41) Grandhi, G. K.; Tomar, R.; Viswanatha, R. Study of Surface and Bulk Electronic Structure of II-VI Semiconductor Nanocrystals Using Cu as a Nanosensor. *ACS Nano* **2012**, *6*, 9751-9763.
- (42) Hao, E.; Zhang, H.; Yang, B.; Ren, H.; Shen, J. Preparation of Luminescent Polyelectrolyte/Cu-Doped ZnSe Nanoparticle Multilayer Composite Films. *J. Colloid Interface Sci.* **2001**, *238*, 285-290.
- (43) Suyver, J. F.; van der Beek, T.; Wuister, S. F.; Kelly, J. J.; Meijerink, A. Luminescence of Nanocrystalline ZnSe:Cu. *Appl. Phys. Lett.* **2001**, *79*, 4222-4224.
- (44) Pradhan, N.; Goorskey, D.; Thessing, J.; Peng, X. An Alternative of CdSe Nanocrystal Emitters: Pure and Tunable Impurity Emissions in ZnSe Nanocrystals. *J. Am. Chem. Soc.* **2005**, *127*, 17586-17587.
- (45) Han, J.; Zhang, H.; Tang, Y.; Liu, Y.; Yao, X.; Yang, B. Role of Redox Reaction and Electrostatics in Transition-Metal Impurity-Promoted Photoluminescence Evolution of Water-Soluble ZnSe Nanocrystals. *J. Phys. Chem. C* **2009**, *113*, 7503-7510.
- (46) Chen, D.; Viswanatha, R.; Ong, G. L.; Xie, R.; Balasubramanian, M.; Peng, X. Temperature Dependence of "Elementary Processes" in Doping Semiconductor Nanocrystals. *J. Am. Chem. Soc.* **2009**, *131*, 9333-9339.
- (47) Jana, S.; Srivastava, B. B.; Acharya, S.; Santra, P. K.; Jana, N. R.; Sarma, D. D.; Pradhan, N. Prevention of Photooxidation in Blue-Green Emitting Cu Doped ZnSe Nanocrystals. *Chem. Commun.* **2010**, *46*, 2853-2855.
- (48) Gul, S.; Cooper, J. K.; Corrado, C.; Vollbrecht, B.; Bridges, F.; Guo, J.; Zhang, J. Z. Synthesis, Optical and Structural Properties, and Charge Carrier Dynamics of Cu-Doped ZnSe Nanocrystals. *J. Phys. Chem. C* **2011**, *115*, 20864-20875.
- (49) Jiang, L.-W.; Zhou, J.; Yang, X.-Z.; Peng, X.-N.; Jiang, H.; Zhuo, D.-Q.; Chen, L.-D.; Yu, X.-F. Microwave-Assisted Synthesis of Surface-Passivated Doped ZnSe Quantum Dots with Enhanced Fluorescence. *Chem. Phys. Lett.* **2011**, *510*, 135-138.
- (50) Wang, C.; Xu, S.; Wang, Z.; Cui, Y. Key Roles of Impurities in the Stability of Internally Doped Cu:ZnSe Nanocrystals in Aqueous Solution. *J. Phys. Chem. C* **2011**, *115*, 18486-18493.
- (51) Xu, S.; Wang, C.; Wang, Z.; Zhang, H.; Yang, J.; Xu, Q.; Shao, H.; Li, R.; Lei, W.; Cui, Y. Aqueous Synthesis of Internally Doped Cu:ZnSe/ZnS Core-Shell Nanocrystals with Good Stability. *Nanotechnology* **2011**, *22*, 275605.
- (52) Xue, G.; Chao, W.; Lu, N.; Xingguang, S. Aqueous Synthesis of Cu-Doped ZnSe Quantum Dots. *J. Lumin.* **2011**, *131*, 1300-1304.

- (53) Liang, Q.; Bai, Y.; Han, L.; Deng, X.; Wu, X.; Wang, Z.; Liu, X.; Meng, J. Hydrothermal Synthesis of ZnSe:Cu Quantum Dots and their Luminescent Mechanism Study by First-Principles. *J. Lumin.* **2013**, *143*, 185-192.
- (54) Kou, S.; Yao, T.; Xu, X.; Zhu, R.; Zhao, Q.; Yang, J. Facile Synthesis and Optical Properties of Ultrathin Cu-doped ZnSe Nanorods. *CrystEngComm* **2013**, *15*, 10495.
- (55) Wang, L.; Cao, L.; Su, G.; Liu, W.; Xia, C.; Zhou, H. Preparation and Characterization of Water-Soluble ZnSe:Cu/ZnS Core/Shell Quantum Dots. *Appl. Surf. Sci.* **2013**, *280*, 673-678.
- (56) Sarkar, S.; Patra, B. K.; Guria, A. K.; Pradhan, N. The Redox Chemistry at the Interface for Retrieving and Brightening the Emission of Doped Semiconductor Nanocrystals. *J. Phys. Chem. Lett.* **2013**, *4*, 2084-2090.
- (57) Rajesh, C.; Phadnis, C. V.; Sonawane, K. G.; Mahamuni, S. Synthesis and Optical Properties of Copper-Doped ZnSe Quantum Dots. *Phys. Scr.* **2015**, *90*, 015803.
- (58) Ramsden, J. J.; Gratzel, M. Photoluminescence of Small Cadmium Sulphide Particles. *J. Chem. Soc., Faraday Trans. 1* **1984**, *80*, 919-933.
- (59) Isarov, A. V.; Chrysochoos, J. Optical and Photochemical Properties of Nonstoichiometric Cadmium Sulfide Nanoparticles: Surface Modification with Copper(II) Ions. *Langmuir* **1997**, *13*, 3142-3149.
- (60) Grandhi, G. K.; Viswanatha, R. Tunable Infrared Phosphors Using Cu Doping in Semiconductor Nanocrystals: Surface Electronic Structure Evaluation. *J. Phys. Chem. Lett.* **2013**, *4*, 409-415.
- (61) Meulenberg, R. W.; van Buuren, T.; Hanif, K. M.; Willey, T. M.; Strouse, G. F.; Terminello, L. J. Structure and Composition of Cu-Doped CdSe Nanocrystals Using Soft X-ray Absorption Spectroscopy. *Nano Lett.* **2004**, *4*, 2277-2285.
- (62) Tananaev, P. N.; Dorofeev, S. G.; Vasil'ev, R. B.; Kuznetsova, T. A. Preparation of Copper-Doped CdSe Nanocrystals. *Inorg. Mater.* **2009**, *45*, 347-351.
- (63) Jawaid, A. M.; Chattopadhyay, S.; Wink, D. J.; Page, L. E.; Snee, P. T. Cluster-Seeded Synthesis of Doped CdSe:Cu<sub>4</sub> Quantum Dots. *ACS Nano* **2013**, *7*, 3190-3197.
- (64) Knowles, K. E.; Nelson, H. D.; Kilburn, T. B.; Gamelin, D. R. Singlet-Triplet Splittings in the Luminescent Excited States of Colloidal Cu<sup>+</sup>:CdSe, Cu<sup>+</sup>:InP, and CuInS<sub>2</sub> Nanocrystals: Charge-Transfer Configurations and Self-Trapped Excitons. *J. Am. Chem. Soc.* **2015**, *137*, 13138-13147.
- (65) Xie, R.; Peng, X. Synthesis of Cu-Doped InP Nanocrystals (d-dots) with ZnSe Diffusion Barrier as Efficient and Color-Tunable NIR Emitters. *J. Am. Chem. Soc.* **2009**, *131*, 10645-10651.
- (66) Zhang, Z.; Li, D.; Xie, R.; Yang, W. Insights into the Energy Levels of Semiconductor Nanocrystals by a Dopant Approach. *Angew. Chem., Int. Ed.* **2013**, *52*, 5052-5055.
- (67) Zhang, Z.; Liu, D.; Li, D.; Huang, K.; Zhang, Y.; Shi, Z.; Xie, R.; Han, M.-Y.; Wang, Y.; Yang, W. Dual Emissive Cu:InP/ZnS/InP/ZnS Nanocrystals: Single-Source "Greener" Emitters with Flexibly Tunable Emission from Visible to Near-Infrared and Their Application in White Light-Emitting Diodes. *Chem. Mater.* **2015**, *27*, 1405-1411.
- (68) Castro, S. L.; Bailey, S. G.; Raffaele, R. P.; Banger, K. K.; Hepp, A. F. Synthesis and Characterization of Colloidal CuInS<sub>2</sub> Nanoparticles from a Molecular Single-Source Precursor. *J. Phys. Chem. B* **2004**, *108*, 12429-12435.
- (69) Zhong, H.; Zhou, Y.; Ye, M.; He, Y.; Ye, J.; He, C.; Yang, C.; Li, Y. Controlled Synthesis and Optical Properties of Colloidal Ternary Chalcogenide CuInS<sub>2</sub> Nanocrystals. *Chem. Mater.* **2008**, *20*, 6434-6443.

- (70) Xie, R.; Rutherford, M.; Peng, X. Formation of High-Quality I-III-VI Semiconductor Nanocrystals by Tuning Relative Reactivity of Cationic Precursors. *J. Am. Chem. Soc.* **2009**, *131*, 5691-5697.
- (71) Li, L.; Pandey, A.; Werder, D. J.; Khanal, B. P.; Pietryga, J. M.; Klimov, V. I. Efficient Synthesis Of Highly Luminescent Copper Indium Sulfide-Based Core/Shell Nanocrystals with Surprisingly Long-Lived Emission. *J. Am. Chem. Soc.* **2011**, *133*, 1176-1179.
- (72) Rice, W. D.; McDaniel, H.; Klimov, V. I.; Crooker, S. A. Magneto-Optical Properties of CuInS<sub>2</sub> Nanocrystals. *J. Phys. Chem. Lett.* **2014**, *5*, 4105-4109.
- (73) Sun, J.; Ikezawa, M.; Wang, X.; Jing, P.; Li, H.; Zhao, J.; Masumoto, Y. Photocarrier Recombination Dynamics in Ternary Chalcogenide CuInS<sub>2</sub> Quantum Dots. *Phys. Chem. Chem. Phys.* **2015**, *17*, 11981-11989.
- (74) Kim, Y.-K.; Ahn, S.-H.; Chung, K.; Cho, Y.-S.; Choi, C.-J. The Photoluminescence of CuInS<sub>2</sub> Nanocrystals: Effect of Non-Stoichiometry and Surface Modification. *J. Mater. Chem.* **2012**, *22*, 1516-1520.
- (75) Nakamura, H.; Kato, W.; Uehara, M.; Nose, K.; Omata, T.; Otsuka-Yao-Matsuo, S.; Miyazaki, M.; Maeda, H. Tunable Photoluminescence Wavelength of Chalcopyrite CuInS<sub>2</sub>-Based Semiconductor Nanocrystals Synthesized in a Colloidal System. *Chem. Mater.* **2006**, *18*, 3330-3335.
- (76) Allen, P. M.; Bawendi, M. G. Ternary I-III-VI Quantum Dots Luminescent in the Red to Near-Infrared. *J. Am. Chem. Soc.* **2008**, *130*, 9240-9241.
- (77) Nose, K.; Omata, T.; Otsuka-Yao-Matsuo, S. Colloidal Synthesis of Ternary Copper Indium Diselenide Quantum Dots and Their Optical Properties. *J. Phys. Chem. C* **2009**, *113*, 3455-3460.
- (78) Katahara, J. K.; Hillhouse, H. W. Quasi-Fermi Level Splitting and Sub-Bandgap Absorptivity from Semiconductor Photoluminescence. *J. Appl. Phys.* **2014**, *116*, 173504.
- (79) Xin, H.; Katahara, J. K.; Braly, I. L.; Hillhouse, H. W. 8% Efficient Cu<sub>2</sub>ZnSn(S,Se)<sub>4</sub> Solar Cells from Redox Equilibrated Simple Precursors in DMSO. *Adv. Energy Mater.* **2014**, *4*, 1301823.
- (80) Ehlert, O.; Osvet, A.; Batentschuk, M.; Winnacker, A.; Nann, T. Synthesis and Spectroscopic Investigations of Cu- and Pb-Doped Colloidal ZnS Nanocrystals. *J. Phys. Chem. B* **2006**, *110*, 23175-23178.
- (81) Steinhagen, C.; Panthani, M. G.; Akhavan, V.; Goodfellow, B.; Koo, B.; Korgel, B. A. Synthesis of Cu<sub>2</sub>ZnSnS<sub>4</sub> Nanocrystals for Use in Low-Cost Photovoltaics. *J. Am. Chem. Soc.* **2009**, *131*, 12554-12555.
- (82) Riha, S. C.; Parkinson, B. A.; Prieto, A. L. Solution-Based Synthesis and Characterization of Cu<sub>2</sub>ZnSnS<sub>4</sub> Nanocrystals. *J. Am. Chem. Soc.* **2009**, *131*, 12054-12055.
- (83) Guo, Q.; Hillhouse, H. W.; Agrawal, R. Synthesis of Cu<sub>2</sub>ZnSnS<sub>4</sub> Nanocrystal Ink and Its Use for Solar Cells. *J. Am. Chem. Soc.* **2009**, *131*, 11672-11673.
- (84) Khare, A.; Wills, A. W.; Ammerman, L. M.; Norris, D. J.; Aydil, E. S. Size Control and Quantum Confinement in Cu<sub>2</sub>ZnSnS<sub>4</sub> Nanocrystals. *Chem. Commun.* **2011**, *47*, 11721-11723.
- (85) van der Stam, W.; Berends, A. C.; Rabouw, F. T.; Willhammar, T.; Ke, X.; Meeldijk, J. D.; Bals, S.; de Mello Donegá, C. Luminescent CuInS<sub>2</sub> Quantum Dots by Partial Cation Exchange in Cu<sub>2-x</sub>S Nanocrystals. *Chem. Mater.* **2015**, *27*, 621-628.
- (86) Akkerman, Q. A.; Genovese, A.; George, C.; Prato, M.; Moreels, I.; Casu, A.; Marras, S.; Curcio, A.; Scarpellini, A.; Pellegrino, T.; Manna, L.; Lesnyak, V. From Binary Cu<sub>2</sub>S to Ternary

Cu-In-S and Quaternary Cu-In-Zn-S Nanocrystals with Tunable Composition via Partial Cation Exchange. *ACS Nano* **2015**, *9*, 521-531.

(87) van der Stam, W.; Blatt, E.; Rabouw, F. T.; Bals, S.; de Mello Donega, C. Near-Infrared Emitting CuInSe<sub>2</sub>/CuInS<sub>2</sub> Dot Core/Rod Shell Heteronanorods by Sequential Cation Exchange. *ACS Nano* **2015**, *9*, 11430-11438.

(88) Kolny-Olesiak, J.; Weller, H. Synthesis And Application Of Colloidal CuInS<sub>2</sub> Semiconductor Nanocrystals. *ACS Appl. Mater. Interfaces* **2013**, *5*, 12221-12237.

(89) Aldakov, D.; Léfrançois, A.; Reiss, P. Ternary and Quaternary Metal Chalcogenide Nanocrystals: Synthesis, Properties, and Applications. *J. Mater. Chem. C* **2013**, *1*, 3756-3776.

(90) Buonsanti, R.; Milliron, D. J. Chemistry of Doped Colloidal Nanocrystals. *Chem. Mater.* **2013**, *25*, 1305-1317.

(91) Srivastava, B. B.; Jana, S.; Pradhan, N. Doping Cu in Semiconductor Nanocrystals: Some Old and Some New Physical Insights. *J. Am. Chem. Soc.* **2011**, *133*, 1007-1015.

(92) Leach, A. D. P.; Macdonald, J. E. The Optoelectronic Properties of CuInS<sub>2</sub> Nanocrystals and their Origin. *J. Phys. Chem. Lett.* **2016**, *7*, 572-583.

(93) van der Stam, W.; Berends, A. C.; de Mello Donegá, C. Prospects of Colloidal Copper Chalcogenide Nanocrystals. *ChemPhysChem* **2015**, DOI: 10.1002/cphc.201500976.

(94) Klausch, A.; Althues, H.; Schrage, C.; Simon, P.; Szatkowski, A.; Bredol, M.; Adam, D.; Kaskel, S. Preparation of Luminescent ZnS:Cu Nanoparticles for the Functionalization of Transparent Acrylate Polymers. *J. Lumin.* **2010**, *130*, 692-697.

(95) Nelson, H. D.; Li, X.; Gamelin, D. R. Computational Studies of the Electronic Structures of Copper-Doped CdSe Nanocrystals: Oxidation States, Jahn-Teller Distortions, Vibronic Bandshapes, and Singlet-Triplet Splittings. *J. Phys. Chem. C* **2016**, *120*, 5714-5723.

(96) Acharya, S.; Pradhan, N. Insertion/Ejection of Dopant Ions in Composition Tunable Semiconductor Nanocrystals. *J. Phys. Chem. C* **2011**, *115*, 19513-19519.

(97) Sarkar, S.; Karan, N. S.; Pradhan, N. Ultrasmall Color-Tunable Copper-Doped Ternary Semiconductor Nanocrystal Emitters. *Angew. Chem., Int. Ed.* **2011**, *50*, 6065-6069.

(98) Zhang, W.; Lou, Q.; Ji, W.; Zhao, J.; Zhong, X. Color-Tunable Highly Bright Photoluminescence of Cadmium-Free Cu-Doped Zn-In-S Nanocrystals and Electroluminescence. *Chem. Mater.* **2014**, *26*, 1204-1212.

(99) Varshni, Y. P. Temperature Dependence of the Energy Gap in Semiconductors. *Physica* **1967**, *34*, 149-154.

(100) Viswanatha, R.; Sarma, D. D. Effect of Structural Modification on the Quantum-Size Effect in II-VI Semiconducting Nanocrystals. *Chem. Asian J.* **2009**, *4*, 904-909.

(101) Franceschetti, A.; Fu, H.; Wang, L. W.; Zunger, A. Many-Body Pseudopotential Theory of Excitons in InP and CdSe Quantum Dots. *Phys. Rev. B* **1999**, *60*, 1819-1829.

(102) Lee, J. R. I.; Meulenberg, R. W.; Hanif, K. M.; Mattoussi, H.; Klepeis, J. E.; Terminello, L. J.; van Buuren, T. Experimental Observation of Quantum Confinement in the Conduction Band of CdSe Quantum Dots. *Phys. Rev. Lett.* **2007**, *98*, 146803.

(103) Ishizumi, A.; White, C. W.; Kanemitsu, Y. Photoluminescence Properties of Impurity-Doped ZnS Nanocrystals Fabricated by Sequential Ion Implantation. *Physica E* **2005**, *26*, 24-27.

(104) Corrado, C.; Hawker, M.; Livingston, G.; Medling, S.; Bridges, F.; Zhang, J. Z. Enhanced Cu Emission in ZnS:Cu,Cl/ZnS Core-Shell Nanocrystals. *Nanoscale* **2010**, *2*, 1213-1221.

(105) Corrado, C.; Cooper, J. K.; Hawker, M.; Hensel, J.; Livingston, G.; Gul, S.; Vollbrecht, B.; Bridges, F.; Zhang, J. Z. Synthesis and Characterization of Organically Soluble Cu-Doped ZnS Nanocrystals with Br Co-activator. *J. Phys. Chem. C* **2011**, *115*, 14559-14570.

- (106) Gul, S.; Cooper, J. K.; Glans, P.-A.; Guo, J.; Yachandra, V. K.; Yano, J.; Zhang, J. Z. Effect of Al<sup>3+</sup> Co-doping on the Dopant Local Structure, Optical Properties, and Exciton Dynamics in Cu<sup>+</sup>-Doped ZnSe Nanocrystals. *ACS Nano* **2013**, *7*, 8680-8692.
- (107) Cooper, J. K.; Gul, S.; Lindley, S. A.; Yano, J.; Zhang, J. Z. Tunable Photoluminescent Core/Shell Cu<sup>+</sup>-Doped ZnSe/ZnS Quantum Dots Codoped with Al<sup>3+</sup>, Ga<sup>3+</sup>, or In<sup>3+</sup>. *ACS Appl. Mater. Interfaces* **2015**, *7*, 10055-10066.
- (108) Liu, M.; Yao, W.; Li, C.; Wu, Z.; Li, L. Tuning Emission and Stokes Shift of CdS Quantum Dots *via* Copper and Indium Co-Doping. *RSC Adv.* **2015**, *5*, 628-634.
- (109) Viswanatha, R.; Brovelli, S.; Pandey, A.; Crooker, S. A.; Klimov, V. I. Copper-Doped Inverted Core/Shell Nanocrystals with “Permanent” Optically Active Holes. *Nano Lett.* **2011**, *11*, 4753-4758.
- (110) Xie, R.; Battaglia, D.; Peng, X. Colloidal InP Nanocrystals as Efficient Emitters Covering Blue to Near-Infrared. *J. Am. Chem. Soc.* **2007**, *129*, 15432-15433.
- (111) Dalpian, G. M.; Chelikowsky, J. R. Self-Purification in Semiconductor Nanocrystals. *Phys. Rev. Lett.* **2006**, *96*, 226802.
- (112) Mikulec, F. V.; Kuno, M.; Bennati, M.; Hall, D. A.; Griffin, R. G.; Bawendi, M. G. Organometallic Synthesis and Spectroscopic Characterization of Manganese-Doped CdSe Nanocrystals. *J. Am. Chem. Soc.* **2000**, *122*, 2532-2540.
- (113) Norris, D. J.; Efros, A. L.; Erwin, S. C. Doped Nanocrystals. *Science* **2008**, *319*, 1776-1779.
- (114) Woodbury, H. H. Diffusion and Solubility Studies. In *Physics and Chemistry of II-VI Compounds*; Aven, M., Prener, J. S., Eds.; North-Holland Publishing Company: Amsterdam, 1967; pp 225-264.
- (115) Alonso, M. I.; Wakita, K.; Pascual, J.; Garriga, M.; Yamamoto, N. Optical Functions and Electronic Structure of CuInSe<sub>2</sub>, CuGaSe<sub>2</sub>, CuInS<sub>2</sub>, and CuGaS<sub>2</sub>. *Phys. Rev. B* **2001**, *63*, 075203.
- (116) Binsma, J. J. M.; Giling, L. J.; Bloem, J. Luminescence of CuInS<sub>2</sub>: I. The Broad Band Emission and its Dependence on the Defect Chemistry. *J. Lumin.* **1982**, *27*, 35-53.
- (117) Guillén, C. CuInS<sub>2</sub> Thin Films Grown Sequentially from Binary Sulfides as Compared to Layers Evaporated Directly from the Elements. *Semicond. Sci. Technol.* **2006**, *21*, 709-712.
- (118) Yoshino, K.; Ikari, T.; Shirakata, S.; Miyake, H.; Hiramatsu, K. Sharp Band Edge Photoluminescence of High-Purity CuInS<sub>2</sub> Single Crystals. *Appl. Phys. Lett.* **2001**, *78*, 742-744.
- (119) Omata, T.; Nose, K.; Otsuka-Yao-Matsuo, S. Size Dependent Optical Band Gap of Ternary I-III-VI<sub>2</sub> Semiconductor Nanocrystals. *J. Appl. Phys.* **2009**, *105*, 073106.
- (120) Zhong, H.; Lo, S. S.; Mirkovic, T.; Li, Y.; Ding, Y.; Li, Y.; Scholes, G. D. Noninjection Gram-Scale Synthesis of Monodisperse Pyramidal CuInS<sub>2</sub> Nanocrystals and Their Size-Dependent Properties. *ACS Nano* **2010**, *4*, 5253-5262.
- (121) Murray, C. B.; Norris, D. J.; Bawendi, M. G. Synthesis and Characterization of Nearly Monodisperse CdE (E = S, Se, Te) Semiconductor Nanocrystallites. *J. Am. Chem. Soc.* **1993**, *115*, 8706-8715.
- (122) Murray, C. B.; Kagan, C. R.; Bawendi, M. G. Synthesis and Characterization of Monodisperse Nanocrystals and Close-Packed Nanocrystal Assemblies. *Annu. Rev. Mater. Sci.* **2000**, *30*, 545-610.
- (123) Omata, T.; Tani, Y.; Kobayashi, S.; Otsuka-Yao-Matsuo, S. Quantum Dot Phosphors and their Application to Inorganic Electroluminescent Device. *Thin Solid Films* **2012**, *520*, 3829-3834.

- (124) Zhong, H.; Wang, Z.; Bovero, E.; Lu, Z.; van Veggel, F. C. J. M.; Scholes, G. D. Colloidal CuInSe<sub>2</sub> Nanocrystals in the Quantum Confinement Regime: Synthesis, Optical Properties, and Electroluminescence. *J. Phys. Chem. C* **2011**, *115*, 12396-12402.
- (125) Uehara, M.; Watanabe, K.; Tajiri, Y.; Nakamura, H.; Maeda, H. Synthesis of CuInS<sub>2</sub> Fluorescent Nanocrystals and Enhancement of Fluorescence by Controlling Crystal Defect. *J. Chem. Phys.* **2008**, *129*, 134709.
- (126) Chen, B.; Zhong, H.; Zhang, W.; Tan, Z.; Li, Y.; Yu, C.; Zhai, T.; Bando, Y.; Yang, S.; Zou, B. Highly Emissive and Color-Tunable CuInS<sub>2</sub>-Based Colloidal Semiconductor Nanocrystals: Off-Stoichiometry Effects and Improved Electroluminescence Performance. *Adv. Funct. Mater.* **2012**, *22*, 2081-2088.
- (127) Liu, W.; Zhang, Y.; Zhao, J.; Feng, Y.; Wang, D.; Zhang, T.; Gao, W.; Chu, H.; Yin, J.; Wang, Y.; Zhao, J.; Yu, W. W. Photoluminescence of Indium-Rich Copper Indium Sulfide Quantum Dots. *J. Lumin.* **2015**, *162*, 191-196.
- (128) Li, L.; Daou, T. J.; Texier, I.; Chi, T. T. K.; Liem, N. Q.; Reiss, P. Highly Luminescent CuInS<sub>2</sub>/ZnS Core/Shell Nanocrystals: Cadmium-Free Quantum Dots for In Vivo Imaging. *Chem. Mater.* **2009**, *21*, 2422-2429.
- (129) Liu, W. C.; Guo, B. L.; Wu, X. S.; Zhang, F. M.; Mak, C. L.; Wong, K. H. Facile Hydrothermal Synthesis of Hydrotropic Cu<sub>2</sub>ZnSnS<sub>4</sub> Nanocrystal Quantum Dots: Band-Gap Engineering and Phonon Confinement Effect. *J. Mater. Chem. A* **2013**, *1*, 3182-3186.
- (130) Arul, N. S.; Yun, D. Y.; Lee, D. U.; Kim, T. W. Strong Quantum Confinement Effects in Kesterite Cu<sub>2</sub>ZnSnS<sub>4</sub> Nanospheres for Organic Optoelectronic Cells. *Nanoscale* **2013**, *5*, 11940-11943.
- (131) Arora, L.; Singh, V. N.; Partheepan, G.; Senguttuvan, T. D.; Jain, K. One-Step Synthesis of Size-Controlled CZTS Quantum Dots. *Appl. Nanosci.* **2015**, DOI: 10.1007/s13204-015-0404-z.
- (132) Liu, Y.; Yao, D.; Shen, L.; Zhang, H.; Zhang, X.; Yang, B. Alkylthiol-Enabled Se Powder Dissolution in Oleylamine at Room Temperature for the Phosphine-Free Synthesis of Copper-Based Quaternary Selenide Nanocrystals. *J. Am. Chem. Soc.* **2012**, *134*, 7207-7210.
- (133) Riha, S. C.; Parkinson, B. A.; Prieto, A. L. Compositionally Tunable Cu<sub>2</sub>ZnSn(S<sub>1-x</sub>Se<sub>x</sub>)<sub>4</sub> Nanocrystals: Probing the Effect of Se-Inclusion in Mixed Chalcogenide Thin Films. *J. Am. Chem. Soc.* **2011**, *133*, 15272-15275.
- (134) Ou, K.-L.; Fan, J.-C.; Chen, J.-K.; Huang, C.-C.; Chen, L.-Y.; Ho, J.-H.; Chang, J.-Y. Hot-Injection Synthesis of Monodispersed Cu<sub>2</sub>ZnSn(S<sub>x</sub>Se<sub>1-x</sub>)<sub>4</sub> Nanocrystals: Tunable Composition and Optical Properties. *J. Mater. Chem.* **2012**, *22*, 14667-14673.
- (135) Zaberca, O.; Oftinger, F.; Chane-Ching, J. Y.; Datas, L.; Lafond, A.; Puech, P.; Balocchi, A.; Lagarde, D.; Marie, X. Surfactant-free CZTS Nanoparticles as Building Blocks for Low-Cost Solar Cell Absorbers. *Nanotechnology* **2012**, *23*, 185402.
- (136) Chen, O.; Chen, X.; Yang, Y.; Lynch, J.; Wu, H.; Zhuang, J.; Cao, Y. C. Synthesis of Metal-Selenide Nanocrystals Using Selenium Dioxide as the Selenium Precursor. *Angew. Chem., Int. Ed.* **2008**, *47*, 8638-8641.
- (137) Corrado, C.; Cooper, J. K.; Zhang, J. Z. Cu-Doped ZnS Nanocrystals: Synthesis, Structure, and Optical Properties. *Sci. Adv. Mater.* **2012**, *4*, 254-265.
- (138) Car, B.; Medling, S.; Corrado, C.; Bridges, F.; Zhang, J. Z. Probing the Local Structure of Dilute Cu Dopants in Fluorescent ZnS Nanocrystals Using EXAFS. *Nanoscale* **2011**, *3*, 4182-4189.
- (139) Broser, I.; Maier, H.; Schulz, H.-J. Fine Structure of the Infrared Absorption and Emission Spectra of Cu<sup>2+</sup> in ZnS and CdS Crystals. *Phys. Rev.* **1965**, *140*, A2135-A2138.

- (140) Telahun, T.; Scherz, U.; Thurian, P.; Heitz, R.; Hoffmann, A.; Broser, I. Nonlinear Zeeman Behavior of Cu<sup>2+</sup> Centers in ZnS and CdS Explained by a Jahn-Teller Effect. *Phys. Rev. B* **1996**, *53*, 1274-1286.
- (141) Thurian, P.; Heitz, R.; Kaczmarczyk, G.; Hoffmann, A.; Broser, I.; Telahun, T.; Schrepel, C.; Goebel, C.; Scherz, U. Jahn-Teller Effect of Cu<sup>2+</sup> in II–VI Compounds. *Z. Phys. Chem.* **1997**, *201*, 137-150.
- (142) Maier, H.; Scherz, U. Vibronic Spectra and the Dynamic Jahn-Teller Effect of Cubic ZnS:Cu<sup>2+</sup>. *Phys. Status Solidi B* **1974**, *62*, 153-164.
- (143) Heitz, R.; Hoffmann, A.; Thurian, P.; Broser, I. The Copper Centre: A Transient Shallow Acceptor in ZnS and CdS. *J. Phys.: Condens. Matter* **1992**, *4*, 157-168.
- (144) Robbins, D. J.; Dean, P. J.; Simmonds, P. E.; Tews, H. The Optoelectronic Properties of Copper in Zinc-cation II-VI Compound Semiconductors. In *Deep Centers in Semiconductors: A State-of-the-Art Approach*; 2nd ed.; Pantelides, S. T., Ed.; Gordon and Breach Science Publishers: Philadelphia, 1992; pp 844-898.
- (145) Tang, A.; Yi, L.; Han, W.; Teng, F.; Wang, Y.; Hou, Y.; Gao, M. Synthesis, Optical Properties, and Superlattice Structure of Cu(I)-Doped CdS Nanocrystals. *Appl. Phys. Lett.* **2010**, *97*, 033112.
- (146) Shionoya, S.; Urabe, K.; Koda, T.; Era, K.; Fujiwara, H. Nature of the Red-Copper Luminescence Centre in ZnS Crystals as Elucidated by Polarization Measurements. *J. Phys. Chem. Solids* **1966**, *27*, 865-869.
- (147) Godlewski, M.; Lamb, W. E.; Cavenett, B. C. ODMR Investigations of IR Photoluminescence in ZnS:Cu. *J. Phys. C: Solid State Phys.* **1982**, *15*, 3925-3942.
- (148) Gislason, H. P.; Monemar, B.; Dean, P. J.; Herbert, D. C.; Depinna, S.; Cavenett, B. C.; Killoran, N. Photoluminescence Studies of the 1.911-eV Cu-Related Complex in GaP. *Phys. Rev. B* **1982**, *26*, 827-845.
- (149) Kana-ah, A.; Cavenett, B. C.; Gislason, H. P.; Monemar, B.; Pistol, M. E. An ODMR Investigation of the (Cu-Li)<sub>I</sub> and (Cu-Li)<sub>III</sub> Complex Defects in GaP. *J. Phys. C: Solid State Phys.* **1986**, *19*, 1239-1250.
- (150) Riha, S. C.; Johnson, D. C.; Prieto, A. L. Cu<sub>2</sub>Se Nanoparticles with Tunable Electronic Properties Due to a Controlled Solid-State Phase Transition Driven by Copper Oxidation and Cationic Conduction. *J. Am. Chem. Soc.* **2011**, *133*, 1383-1390.
- (151) Dorfs, D.; Härtling, T.; Miszta, K.; Bigall, N. C.; Kim, M. R.; Genovese, A.; Falqui, A.; Povia, M.; Manna, L. Reversible Tunability of the Near-Infrared Valence Band Plasmon Resonance in Cu<sub>2-x</sub>Se Nanocrystals. *J. Am. Chem. Soc.* **2011**, *133*, 11175-11180.
- (152) Kriegel, I.; Jiang, C.; Rodriguez-Fernandez, J.; Schaller, R. D.; Talapin, D. V.; da Como, E.; Feldmann, J. Tuning the Excitonic and Plasmonic Properties of Copper Chalcogenide Nanocrystals. *J. Am. Chem. Soc.* **2012**, *134*, 1583-1590.
- (153) Zhao, Y.; Pan, H.; Lou, Y.; Qiu, X.; Zhu, J.; Burda, C. Plasmonic Cu<sub>2-x</sub>S Nanocrystals: Optical and Structural Properties of Copper-Deficient Copper(I) Sulfides. *J. Am. Chem. Soc.* **2009**, *131*, 4253-4261.
- (154) Luther, J. M.; Jain, P. K.; Ewers, T.; Alivisatos, A. P. Localized Surface Plasmon Resonances Arising from Free Carriers in Doped Quantum Dots. *Nat. Mater.* **2011**, *10*, 361-366.
- (155) Brovelli, S.; Galland, C.; Viswanatha, R.; Klimov, V. I. Tuning Radiative Recombination in Cu-doped Nanocrystals via Electrochemical Control of Surface Trapping. *Nano Lett.* **2012**, *12*, 4372-4379.

- (156) Weaver, A. L.; Gamelin, D. R. Photoluminescence Brightening via Electrochemical Trap Passivation in ZnSe and Mn<sup>2+</sup>-Doped ZnSe Quantum Dots. *J. Am. Chem. Soc.* **2012**, *134*, 6819-6825.
- (157) Tran, T. K. C.; Le, Q. P.; Nguyen, Q. L.; Li, L.; Reiss, P. Time-Resolved Photoluminescence Study of CuInS<sub>2</sub>/ZnS Nanocrystals. *Adv. Nat. Sci.: Nanosci. Nanotechnol.* **2010**, *1*, 025007.
- (158) Kirchhoff, J. R.; Gamache, J., R. E.; Blaskie, M. W.; Del Paggio, A. A.; Lengel, R. K.; McMillin, D. R. Temperature Dependence of Luminescence from Cu(NN)<sub>2</sub><sup>+</sup> Systems in Fluid Solution. Evidence for the Participation of Two Excited States. *Inorg. Chem.* **1983**, *22*, 2380-2384.
- (159) Bergman, P.; Monemar, B.; Pistol, M.-E. Transient Characteristics of Excitons Bound at Hole-Attractive Isoelectronic Centers in GaP. *Phys. Rev. B* **1989**, *40*, 12280-12289.
- (160) Monemar, B.; Lindelfelt, U.; Chen, W. M. Electronic Structure of Bound Excitons in Semiconductors *Physica B* **1987**, *146*, 256-285.
- (161) Schlegel, G.; Bohnenberger, J.; Potapova, I.; Mews, A. Fluorescence Decay Time of Single Semiconductor Nanocrystals. *Phys. Rev. Lett.* **2002**, *88*, 137401.
- (162) Qu, L.; Peng, X. Control of Photoluminescence Properties of CdSe Nanocrystals in Growth. *J. Am. Chem. Soc.* **2002**, *124*, 2049-2055.
- (163) Chen, O.; Zhao, J.; Chauhan, V. P.; Cui, J.; Wong, C.; Harris, D. K.; Wei, H.; Han, H.-S.; Fukumura, D.; Jain, R. K.; Bawendi, M. G. Compact High-Quality CdSe-CdS Core-Shell Nanocrystals with Narrow Emission Linewidths and Suppressed Blinking. *Nat. Mater.* **2013**, *12*, 445-451.
- (164) Empedocles, S.; Bawendi, M. Spectroscopy of Single CdSe Nanocrystallites. *Acc. Chem. Res.* **1999**, *32*, 389-396.
- (165) Neuhauser, R. G.; Shimizu, K. T.; Woo, W. K.; Empedocles, S. A.; Bawendi, M. G. Correlation between Fluorescence Intermittency and Spectral Diffusion in Single Semiconductor Quantum Dots. *Phys. Rev. Lett.* **2000**, *85*, 3301-3304.
- (166) Gomez, D. E.; van Embden, J.; Mulvaney, P. Spectral Diffusion of Single Semiconductor Nanocrystals: The Influence of the Dielectric Environment. *Appl. Phys. Lett.* **2006**, *88*, 154106.
- (167) van Sark, W. G. J. H. M.; Frederix, P. L. T. M.; Bol, A. A.; Gerritsen, H. C.; Meijerink, A. Blueing, Bleaching, and Blinking of Single CdSe/ZnS Quantum Dots. *ChemPhysChem* **2002**, *3*, 871-879.
- (168) Ishizumi, A.; White, C. W.; Kanemitsu, Y. Space-Resolved Photoluminescence of ZnS:Cu,Al Nanocrystals Fabricated by Sequential Ion Implantation. *Appl. Phys. Lett.* **2004**, *84*, 2397.
- (169) Coppens, P.; Vorontsov, I. I.; Graber, T.; Kovalevsky, A. Y.; Chen, Y.-S.; Wu, G.; Gembicky, M.; Novozhilova, I. V. Geometry Changes of a Cu(I) Phenanthroline Complex on Photoexcitation in a Confining Medium by Time-Resolved X-ray Diffraction. *J. Am. Chem. Soc.* **2004**, *126*, 5980-5981.
- (170) Vorontsov, I. I.; Graber, T.; Kovalevsky, A. Y.; Novozhilova, I. V.; Gembicky, M.; Chen, Y.-S.; Coppens, P. Capturing and Analyzing the Excited-State Structure of a Cu(I) Phenanthroline Complex by Time-Resolved Diffraction and Theoretical Calculations. *J. Am. Chem. Soc.* **2009**, *131*, 6566-6573.
- (171) Ueng, H. Y.; Hwang, H. L. The Defect Structure of CuInS<sub>2</sub>. Part I: Intrinsic Defects. *J. Phys. Chem. Solids* **1989**, *50*, 1297-1305.

- (172) Zhong, H.; Bai, Z.; Zou, B. Tuning the Luminescence Properties of Colloidal I–III–VI Semiconductor Nanocrystals for Optoelectronics and Biotechnology Applications. *J. Phys. Chem. Lett.* **2012**, *3*, 3167-3175.
- (173) Shi, A.; Wang, X.; Meng, X.; Liu, X.; Li, H.; Zhao, J. Temperature-dependent photoluminescence of CuInS<sub>2</sub> quantum dots. *J. Lumin.* **2012**, *132*, 1819-1823.
- (174) Meinardi, F.; McDaniel, H.; Carulli, F.; Colombo, A.; Velizhanin, K. A.; Makarov, N. S.; Simonutti, R.; Klimov, V. I.; Brovelli, S. Highly Efficient Large-Area Colourless Luminescent Solar Concentrators Using Heavy-Metal-Free Colloidal Quantum Dots. *Nat. Nanotechnol.* **2015**, *10*, 878-885.
- (175) Yarema, O.; Bozyigit, D.; Rousseau, I.; Nowack, L.; Yarema, M.; Heiss, W.; Wood, V. Highly Luminescent, Size- and Shape-Tunable Copper Indium Selenide Based Colloidal Nanocrystals. *Chem. Mater.* **2013**, *25*, 3753-3757.
- (176) Komarala, V. K.; Xie, C.; Wang, Y.; Xu, J.; Xiao, M. Time-Resolved Photoluminescence Properties of CuInS<sub>2</sub>/ZnS Nanocrystals: Influence of Intrinsic Defects and External Impurities. *J. Appl. Phys.* **2012**, *111*, 124314.
- (177) Nam, D.-E.; Song, W.-S.; Yang, H. Noninjection, One-Pot Synthesis of Cu-Deficient CuInS<sub>2</sub>/ZnS Core/Shell Quantum Dots and their Fluorescent Properties. *J. Colloid Interface Sci.* **2011**, *361*, 491-496.
- (178) Hamanaka, Y.; Kuzuya, T.; Sofue, T.; Kino, T.; Ito, K.; Sumiyama, K. Defect-Induced Photoluminescence and Third-Order Nonlinear Optical Response of Chemically Synthesized Chalcopyrite CuInS<sub>2</sub> Nanoparticles. *Chem. Phys. Lett.* **2008**, *466*, 176-180.
- (179) Omata, T.; Nose, K.; Kurimoto, K.; Kita, M. Electron Transition Responsible for Size-Dependent Photoluminescence of Colloidal CuInS<sub>2</sub> Quantum Dots. *J. Mater. Chem. C* **2014**, *2*, 6867-6872.
- (180) Sun, J.; Zhu, D.; Zhao, J.; Ikezawa, M.; Wang, X.; Masumoto, Y. Ultrafast Carrier Dynamics in CuInS<sub>2</sub> Quantum Dots. *Appl. Phys. Lett.* **2014**, *104*, 023118.
- (181) Wu, K.; Liang, G.; Kong, D.; Chen, J.; Chen, Z.; Shan, X.; McBride, J. R.; Lian, T. Quasi-Type II CuInS<sub>2</sub>/CdS Core/Shell Quantum Dots. *Chem. Sci.* **2016**, *7*, 1238-1244.
- (182) Leach, A. D. P.; Shen, X.; Faust, A.; Cleveland, M. C.; La Croix, A. D.; Banin, U.; Pantelides, S. T.; Macdonald, J. E. Defect Luminescence from Wurtzite CuInS<sub>2</sub> Nanocrystals: Combined Experimental and Theoretical Analysis. *J. Phys. Chem. C* **2016**, *120*, 5207-5212.
- (183) Kraatz, I. T.; Booth, M.; Whitaker, B. J.; Nix, M. G. D.; Critchley, K. Sub-Bandgap Emission and Intraband Defect-Related Excited-State Dynamics in Colloidal CuInS<sub>2</sub>/ZnS Quantum Dots Revealed by Femtosecond Pump–Dump–Probe Spectroscopy. *J. Phys. Chem. C* **2014**, *118*, 24102-24109.
- (184) Kazmerski, L. L.; Sanborn, G. A. CuInS<sub>2</sub> Thin-Film Homojunction Solar Cells. *J. Appl. Phys.* **1977**, *48*, 3178-3180.
- (185) Tell, B.; Thiel, F. A. Photovoltaic Properties of *p-n* Junctions in CuInS<sub>2</sub>. *J. Appl. Phys.* **1979**, *50*, 5045-5046.
- (186) Zhang, F.; He, X.-W.; Li, W.-Y.; Zhang, Y.-K. One-Pot Aqueous Synthesis of Composition-Tunable Near-Infrared Emitting Cu-Doped CdS Quantum Dots as Fluorescence Imaging Probes in Living Cells. *J. Mater. Chem.* **2012**, *22*, 22250-22257.
- (187) Klaer, J.; Bruns, J.; Henninger, R.; Siemer, K.; Klenk, R.; Ellmer, K.; Bräunig, D. Efficient CuInS<sub>2</sub> Thin-Film Solar Cells Prepared by a Sequential Process. *Semicond. Sci. Technol.* **1998**, *13*, 1456-1458.

- (188) Ortega-Lopez, M.; Morales-Acevedo, A. Characterization of CuInS<sub>2</sub> Thin Films for Solar Cells Prepared by Spray Pyrolysis. *Thin Solid Films* **1998**, *330*, 96-101.
- (189) Wakita, K.; Hirooka, H.; Yasuda, S.; Fujita, F.; Yamamoto, N. Resonant Raman Scattering and Luminescence in CuInS<sub>2</sub> Crystals. *J. Appl. Phys.* **1998**, *83*, 443-447.
- (190) Wakita, K.; Fujita, F.; Yamamoto, N. Photoluminescence Excitation Spectra of CuInS<sub>2</sub> Crystals. *J. Appl. Phys.* **2001**, *90*, 1292-1296.
- (191) Migliorato, P.; Shay, J. L.; Kasper, H. M.; Wagner, S. Analysis of the Electrical and Luminescent Properties of CuInSe<sub>2</sub>. *J. Appl. Phys.* **1975**, *46*, 1777-1782.
- (192) Yu, P. W. Radiative Recombination in Melt-Grown and Cd-Implanted CuInSe<sub>2</sub>. *J. Appl. Phys.* **1976**, *47*, 677-684.
- (193) Yu, P. Y.; Cardona, M. *Fundamentals of Semiconductors*; 3rd ed.; Springer-Verlag: New York, 2003.
- (194) Cadirci, M.; Masala, O.; Pickett, N.; Binks, D. Ultrafast Charge Dynamics in CuInS<sub>2</sub> Nanocrystal Quantum Dots. *Chem. Phys.* **2014**, *438*, 60-65.
- (195) Shabaev, A.; Mehl, M. J.; Efros, A. L. Energy Band Structure of CuInS<sub>2</sub> and Optical Spectra of CuInS<sub>2</sub> Nanocrystals. *Phys. Rev. B* **2015**, *92*, 035431.
- (196) Mott, N. F.; Stoneham, A. M. The Lifetime of Electrons, Holes, and Excitons Before Self-Trapping. *J. Phys. C: Solid State Phys.* **1977**, *10*, 3391-3398.
- (197) Toyozawa, Y. Dynamics of Excitons in Deformable Lattice. *J. Lumin.* **1981**, *24*, 23-30.
- (198) Vogelsang, H.; Husberg, O.; Köhler, U.; von der Osten, W. Exciton Self-Trapping in AgCl Nanocrystals. *Phys. Rev. B* **2000**, *61*, 1847-1852.
- (199) Song, K. S.; Williams, R. T. *Self-Trapped Excitons*; 2nd ed.; Springer-Verlag: New York, 1996.
- (200) Höhne, M.; Stasiw, M. ESR Detection of Self-Trapped Holes in AgCl. *Phys. Status Solidi* **1968**, *28*, 247-253.
- (201) Williams, R. T.; Song, K. S. The Self-Trapped Exciton. *J. Phys. Chem. Solids* **1990**, *51*, 679-716.
- (202) Datta, A.; Panda, S. K.; Chaudhuri, S. Phase Transformation and Optical Properties of Copper-Doped ZnS Nanorods. *J. Solid State Chem.* **2008**, *181*, 2332-2337.
- (203) Pandey, A.; Brovelli, S.; Viswanatha, R.; Li, L.; Pietryga, J. M.; Klimov, V. I.; Crooker, S. A. Long-Lived Photoinduced Magnetization in Copper-Doped ZnSe-CdSe Core-Shell Nanocrystals. *Nat. Nanotechnol.* **2012**, *7*, 792-797.
- (204) Sher, P. H.; Smith, J. M.; Dalgarno, P. A.; Warburton, R. J.; Chen, X.; Dobson, P. J.; Daniels, S. M.; Pickett, N. L.; O'Brien, P. Power Law Carrier Dynamics in Semiconductor Nanocrystals at Nanosecond Timescales. *Appl. Phys. Lett.* **2008**, *92*, 101111.
- (205) Jones, M.; Lo, S. S.; Scholes, G. D. Quantitative Modeling of the Role of Surface Traps in CdSe/CdS/ZnS Nanocrystal Photoluminescence Decay Dynamics. *Proc. Natl. Acad. Sci.* **2009**, *106*, 3011-3016.
- (206) Rabouw, F. T.; Kamp, M.; van Dijk-Moes, R. J. A.; Gamelin, D. R.; Koenderink, A. F.; Meijerink, A.; Vanmaekelbergh, D. Delayed Exciton Emission and Its Relation to Blinking in CdSe Quantum Dots. *Nano Lett.* **2015**, *15*, 7718-7725.
- (207) Allen, J. W. Kinetics of Long-Wavelength Infrared Stimulation of Donor-Acceptor Pair Luminescence in ZnS. *Phys. Rev. B* **1974**, *9*, 1564-1577.
- (208) Wang, H.; de Mello Donegá, C.; Meijerink, A.; Glasbeek, M. Ultrafast Exciton Dynamics in CdSe Quantum Dots Studied from Bleaching Recovery and Fluorescent Transients. *J. Phys. Chem. B* **2006**, *110*, 733-737.

- (209) de Mello Donegá, C.; Koole, R. Size Dependence of the Spontaneous Emission Rate and Absorption Cross Section of CdSe and CdTe Quantum Dots. *J. Phys. Chem. C* **2009**, *113*, 6511-6520.
- (210) Zhang, J.; Zhang, X.; Zhang, J. Y. Size-Dependent Time-Resolved Photoluminescence of Colloidal CdSe Nanocrystals. *J. Phys. Chem. C* **2009**, *113*, 9512-9515.
- (211) Panthani, M. G.; Akhavan, V.; Goodfellow, B.; Schmidtke, J. P.; Dunn, L.; Dodabalapur, A.; Barbara, P. F.; Korgel, B. A. Synthesis of CuInS<sub>2</sub>, CuInSe<sub>2</sub>, and Cu(In<sub>x</sub>Ga<sub>1-x</sub>)Se<sub>2</sub> (CIGS) Nanocrystal "Inks" for Printable Photovoltaics. *J. Am. Chem. Soc.* **2008**, *130*, 16770-16777.
- (212) Halpert, J. E.; Morgenstern, F. S. F.; Ehrler, B.; Vaynzof, Y.; Credgington, D.; Greenham, N. C. Charge Dynamics in Solution-Processed Nanocrystalline CuInS<sub>2</sub> Solar Cells. *ACS Nano* **2015**, *9*, 5857-5867.
- (213) Akhavan, V.; Panthani, M. G.; Goodfellow, B. W.; Reid, D. K.; Korgel, B. A. Thickness-Limited Performance of CuInSe<sub>2</sub> Nanocrystal Photovoltaic Devices. *Opt. Express* **2010**, *18*, A411-A420.
- (214) Guo, Q.; Kim, S. J.; Kar, M.; Shafarman, W. N.; Birkmire, R. W.; Stach, E. A.; Agrawal, R.; Hillhouse, H. W. Development of CuInSe<sub>2</sub> Nanocrystal and Nanoring Inks for Low-Cost Solar Cells. *Nano Lett.* **2008**, *8*, 2982-2987.
- (215) Lee, J. H.; Chang, J.; Cha, J.-H.; Lee, Y.; Han, J. E.; Jung, D.-Y.; Choi, E. C.; Hong, B. Large-Scale, Surfactant-Free Solution Syntheses of Cu(In,Ga)(S,Se)<sub>2</sub> Nanocrystals for Thin Film Solar Cells. *Eur. J. Inorg. Chem.* **2011**, *2011*, 647-651.
- (216) Guo, Q.; Ford, G. M.; Hillhouse, H. W.; Agrawal, R. Sulfide Nanocrystal Inks for Dense Cu(In<sub>1-x</sub>Ga<sub>x</sub>)(S<sub>1-y</sub>Se<sub>y</sub>)<sub>2</sub> Absorber Films and Their Photovoltaic Performance. *Nano Lett.* **2009**, *9*, 3060-3065.
- (217) Guo, Q.; Ford, G. M.; Agrawal, R.; Hillhouse, H. W. Ink Formulation and Low-Temperature Incorporation of Sodium to Yield 12% Efficient Cu(In,Ga)(S,Se)<sub>2</sub> Solar Cells from Sulfide Nanocrystal Inks. *Prog. Photovolt: Res. Appl.* **2013**, *21*, 64-71.
- (218) Harvey, T. B.; Mori, I.; Stolle, C. J.; Bogart, T. D.; Ostrowski, D. P.; Glaz, M. S.; Du, J.; Pernik, D. R.; Akhavan, V. A.; Kesrouani, H.; Vanden Bout, D. A.; Korgel, B. A. Copper Indium Gallium Selenide (CIGS) Photovoltaic Devices Made Using Multistep Selenization of Nanocrystal Films. *ACS Appl. Mater. Interfaces* **2013**, *5*, 9134-9140.
- (219) Guo, Q.; Ford, G. M.; Yang, W.-C.; Walker, B. C.; Stach, E. A.; Hillhouse, H. W.; Agrawal, R. Fabrication of 7.2% Efficient CZTSSe Solar Cells Using CZTS Nanocrystals. *J. Am. Chem. Soc.* **2010**, *132*, 17384-17386.
- (220) Akhavan, V. A.; Goodfellow, B. W.; Panthani, M. G.; Steinhagen, C.; Harvey, T. B.; Stolle, C. J.; Korgel, B. A. Colloidal CIGS and CZTS Nanocrystals: A Precursor Route to Printed Photovoltaics. *J. Sol. State Chem.* **2012**, *189*, 2-12.
- (221) Zhou, H.; Hsu, W.-C.; Duan, H.-S.; Bob, B.; Yang, W.; Song, T.-B.; Hsu, C.-J.; Yang, Y. CZTS Nanocrystals: A Promising Approach for Next Generation Thin Film Photovoltaics. *Energy Environ. Sci.* **2013**, *6*, 2822-2838.
- (222) Bruchez, J., M.; Moronne, M.; Gin, P.; Weiss, S.; Alivisatos, A. P. Semiconductor Nanocrystals as Fluorescent Biological Labels. *Science* **1998**, *281*, 2013-2016.
- (223) Wu, P.; Yan, X.-P. Doped Quantum Dots for Chemo/Biosensing and Bioimaging. *Chem. Soc. Rev.* **2013**, *42*, 5489-5521.
- (224) Wegner, K. D.; Hildebrandt, N. Quantum Dots: Bright and Versatile *in Vitro* and *in Vivo* Fluorescence Imaging Biosensors. *Chem. Soc. Rev.* **2015**, *44*, 4792-4834.

- (225) McLaurin, E. J.; Bradshaw, L. R.; Gamelin, D. R. Dual-Emitting Nanoscale Temperature Sensors. *Chem. Mater.* **2013**, *25*, 1283-1292.
- (226) Michalet, X.; Pinaud, F. F.; Bentolila, L. A.; Tsay, J. M.; Doose, S.; Li, J. J.; Sundaresan, G.; Wu, A. M.; Gambhir, S. S.; Weiss, S. Quantum Dots for Live Cells, in Vivo Imaging, and Diagnostics. *Science* **2005**, *307*, 538-544.
- (227) Yu, K.; Ng, P.; Ouyang, J.; Zaman, M. B.; Abulrob, A.; Baral, T. N.; Fatehi, D.; Jakubek, Z. J.; Kingston, D.; Wu, X.; Liu, X.; Hebert, C.; Leek, D. M.; Whitfield, D. M. Low-Temperature Approach to Highly Emissive Copper Indium Sulfide Colloidal Nanocrystals and Their Bioimaging Applications. *ACS Appl. Mater. Interfaces* **2013**, *5*, 2870-2880.
- (228) Cheng, C.-Y.; Ou, K.-L.; Huang, W.-T.; Chen, J.-K.; Chang, J.-Y.; Yang, C.-H. Gadolinium-Based CuInS<sub>2</sub>/ZnS Nanoprobe for Dual-Modality Magnetic Resonance/Optical Imaging. *ACS Appl. Mater. Interfaces* **2013**, *5*, 4389-4400.
- (229) Geszke-Moritz, M.; Clavier, G.; Lulek, J.; Schneider, R. Copper- or Manganese-Doped ZnS Quantum Dots as Fluorescent Probes for Detecting Folic Acid in Aqueous Media. *J. Lumin.* **2012**, *132*, 987-991.
- (230) Maity, A. R.; Palmal, S.; Basiruddin, S.; Karan, N. S.; Sarkar, S.; Pradhan, N.; Jana, N. R. Doped Semiconductor Nanocrystal Based Fluorescent Cellular Imaging Probes. *Nanoscale* **2013**, *5*, 5506-5513.
- (231) Jiang, T.; Song, J.; Wang, H.; Ye, X.; Wang, H.; Zhang, W.; Yang, M.; Xia, R.; Zhu, L.; Xu, X. Aqueous Synthesis of Color Tunable Cu Doped Zn-In-S/ZnS Nanoparticles in the Whole Visible Region for Cellular Imaging. *J. Mater. Chem. B* **2015**, *3*, 2402-2410.
- (232) Weissleder, R. A Clearer Vision for *in Vivo* Imaging. *Nat. Biotechnol.* **2001**, *19*, 316-317.
- (233) Chen, C.-W.; Wu, D.-Y.; Chan, Y.-C.; Lin, C. C.; Chung, P.-H.; Hsiao, M.; Liu, R.-S. Evaluations of the Chemical Stability and Cytotoxicity of CuInS<sub>2</sub> and CuInS<sub>2</sub>/ZnS Core/Shell Quantum Dots. *J. Phys. Chem. C* **2015**, *119*, 2852-2860.
- (234) Pons, T.; Pic, E.; Lequeux, N.; Cassette, E.; Bezdetsnaya, L.; Guillemin, F.; Marchal, F.; Dubertret, B. Cadmium-Free CuInS<sub>2</sub>/ZnS Quantum Dots for Sentinel Lymph Node Imaging with Reduced Toxicity. *ACS Nano* **2010**, *5*, 2531-2538.
- (235) Huang, J.; Yang, Y.; Xue, S.; Yang, B.; Liu, S.; Shen, J. Photoluminescence and Electroluminescence of ZnS:Cu Nanocrystals in Polymeric Networks. *Appl. Phys. Lett.* **1997**, *70*, 2335-2337.
- (236) Que, W.; Zhou, Y.; Lam, Y. L.; Chan, Y. C.; Kam, C. H.; Liu, B.; Gan, L. M.; Chew, C. H.; Xu, G. Q.; Chua, S. J.; Xu, S. J.; Mendis, F. V. C. Photoluminescence and Electroluminescence from Copper Doped Zinc Sulphide Nanocrystals/Polymer Composite. *Appl. Phys. Lett.* **1998**, *73*, 2727-2729.
- (237) Tan, Z.; Zhang, Y.; Xie, C.; Su, H.; Liu, J.; Zhang, C.; Dellas, N.; Mohny, S. E.; Wang, Y.; Wang, J.; Xu, J. Near-Band-Edge Electroluminescence from Heavy-Metal-Free Colloidal Quantum Dots. *Adv. Mater.* **2011**, *23*, 3553-3558.
- (238) Song, W.-S.; Yang, H. Efficient White-Light-Emitting Diodes Fabricated from Highly Fluorescent Copper Indium Sulfide Core/Shell Quantum Dots. *Chem. Mater.* **2012**, *24*, 1961-1967.
- (239) Chuang, P.-H.; Lin, C. C.; Liu, R.-S. Emission-Tunable CuInS<sub>2</sub>/ZnS Quantum Dots: Structure, Optical Properties, and Application in White Light-Emitting Diodes with High Color Rendering Index. *ACS Appl. Mater. Interfaces* **2014**, *6*, 15379-15387.
- (240) Park, S. H.; Hong, A.; Kim, J.-H.; Yang, H.; Lee, K.; Jang, H. S. Highly Bright Yellow-Green-Emitting CuInS<sub>2</sub> Colloidal Quantum dots with Core/Shell/Shell Architecture for White Light-Emitting Diodes. *ACS Appl. Mater. Interfaces* **2015**, *7*, 6764-6771.

- (241) Chen, B.; Zhong, H.; Wang, M.; Liu, R.; Zou, B. Integration of CuInS<sub>2</sub>-Based Nanocrystals for High Efficiency and High Colour Rendering White Light-Emitting Diodes. *Nanoscale* **2013**, *5*, 3514-3519.
- (242) Shirasaki, Y.; Supran, G. J.; Bawendi, M. G.; Bulovic, V. Emergence of Colloidal Quantum-Dot Light-Emitting Technologies. *Nat. Photonics* **2013**, *7*, 13-23.
- (243) Bradshaw, L. R.; Knowles, K. E.; McDowall, S.; Gamelin, D. R. Nanocrystals for Luminescent Solar Concentrators. *Nano Lett.* **2015**, *15*, 1315-1323.
- (244) Knowles, K. E.; Kilburn, T. B.; Alzate, D. G.; McDowall, S.; Gamelin, D. R. Bright CuInS<sub>2</sub>/CdS nanocrystal phosphors for high-gain full-spectrum luminescent solar concentrators. *Chem. Commun.* **2015**, *51*, 9129-9132.
- (245) Hu, X.; Kang, R.; Zhang, Y.; Deng, L.; Zhong, H.; Zou, B.; Shi, L.-J. Ray-Trace Simulation of CuInS(Se)<sub>2</sub> Quantum Dot Based Luminescent Solar Concentrators. *Opt. Express* **2015**, *23*, A858-A867.
- (246) Li, C.; Chen, W.; Wu, D.; Quan, D.; Zhou, Z.; Hao, J.; Qin, J.; Li, Y.; He, Z.; Wang, K. Large Stokes Shift and High Efficiency Luminescent Solar Concentrator Incorporated with CuInS<sub>2</sub>/ZnS Quantum Dots. *Sci. Rep.* **2015**, *5*, 17777.
- (247) Weber, W. H.; Lambe, J. Luminescent Greenhouse Collector for Solar Radiation. *Appl. Opt.* **1976**, *15*, 2299-2300.
- (248) Batchelder, J. S.; Zewail, A. H.; Cole, T. Luminescent Solar Concentrators. 1: Theory of Operation and Techniques for Performance Evaluation. *Appl. Opt.* **1979**, *18*, 3090-3110.
- (249) Reisfeld, R.; Shamrakov, D.; Jorgensen, C. Photostable Solar Concentrators Based on Fluorescent Glass Films. *Sol. Energy Mater. Sol. Cells* **1994**, *33*, 417-427.
- (250) Debije, M. G.; Verbunt, P. P. C. Thirty Years of Luminescent Solar Concentrator Research: Solar Energy for the Built Environment. *Adv. Energy Mater.* **2012**, *2*, 12-35.
- (251) Currie, M. J.; Mapel, J. K.; Heidel, T. D.; Goffri, S.; Baldo, M. A. High-Efficiency Organic Solar Concentrators for Photovoltaics. *Science* **2008**, *321*, 226-228.
- (252) Erickson, C. S.; Bradshaw, L. R.; McDowall, S.; Gilbertson, J. D.; Gamelin, D. R.; Patrick, D. L. Zero-Reabsorption Doped-Nanocrystal Luminescent Solar Concentrators. *ACS Nano* **2014**, *8*, 3461-3467.

## Biographies

Kathryn E. Knowles completed her Ph.D. in chemistry at Northwestern University in 2013 as a Department of Energy Office of Science Graduate Research Fellow studying the effects of surface chemistry on the optical and electronic properties of colloidal nanocrystals under the guidance of Prof. Emily Weiss. She is now a postdoc in Prof. Daniel Gamelin's group at the University of Washington studying copper-doped colloidal nanocrystals with the support of a Department of Energy, Energy Efficiency and Renewable Energy (EERE) Postdoctoral Research Award. She will begin her independent career as an assistant professor of chemistry at the University of Rochester in July 2016.

Kimberly H. Hartstein received her B.A. in chemistry from Washington University in St. Louis in 2011. Before beginning her graduate studies, she spent a year studying at Westfälische-Wilhelms Universität Münster as a Fulbright Research Fellow. She is currently a National Science Foundation Graduate Research Fellow and is pursuing her Ph.D. in chemistry in Prof. Daniel

Gamelin's group at the University of Washington. Her research focuses on elucidating the electronic structures of electronically doped semiconductor nanomaterials.

Troy B. Kilburn received his B.S. in chemistry and B.A. in physics from Central Washington University in 2013. As an undergraduate, he studied the synthesis of europium-doped strontium borates under Dr. Anthony Diaz. Troy is currently pursuing his Ph.D. in chemistry at the University of Washington in Prof. Daniel Gamelin's group, where he is working on understanding the photophysics of colloidal nanocrystals.

Arianna Marchioro obtained her B.S. in chemistry (2008) and M.S. in molecular and biological chemistry (2010) at the École Polytechnique Fédérale de Lausanne (EPFL). She received her Ph.D. in photonics in 2014 at EPFL under the supervision of Prof. Jacques-E. Moser and Prof. Michael Grätzel. Her dissertation work focused on interfacial charge-transfer dynamics in hybrid organic-inorganic solid-state solar cells. She was awarded the Swiss National Science Foundation Fellowship for Early Postdoctoral Research in 2014 and is currently working at the University of Washington with Prof. Daniel Gamelin, where she is investigating the photophysical properties of copper-containing semiconductor nanocrystals.

Heidi D. Nelson received her B.S. in chemistry from the University of Minnesota-Twin Cities in 2012. She received a National Science Foundation Graduate Research Fellowship in 2013 and is currently pursuing her Ph.D. in chemistry in Prof. Daniel Gamelin's group at the University of Washington. Her research focuses on spectroscopic and computational studies of the optical and magnetic properties of doped semiconductor nanocrystals.

Patrick J. Whitham obtained his B.S. (2009) and M.S. (2010) degrees in the Department of Chemistry at Idaho State University under the supervision of Prof. René Rodriguez. During his undergraduate and masters study, he investigated the formation of germanium chalcogenide thin films by plasma enhanced chemical vapor deposition. He is currently pursuing his Ph.D. in chemistry with Professors Philip Reid and Daniel Gamelin at the University of Washington. His current work focuses on fluorescence microscopy of semiconductor nanomaterials.

Daniel R. Gamelin received his B.A. in chemistry from Reed College, spent a year as a visiting scientist at the Max-Planck-Institut für Strahlenchemie, and earned his Ph.D. in chemistry from Stanford University working with Edward I. Solomon in the fields of inorganic and bioinorganic spectroscopies. Following a postdoctoral appointment working with Hans U. Güdel (University of Bern) studying luminescent inorganic materials, he joined the chemistry faculty at the University of Washington, Seattle (2000), where he presently holds the Harry and Catherine Jayne Board Endowed Professorship in Chemistry. His research involves the development of new inorganic materials with unusual electronic structures that give rise to desirable photophysical, photochemical, magnetic, or magneto-optical properties. He spent 2007–2008 as a visiting professor at the University of Konstanz Center for Applied Photonics and the École Polytechnique Fédérale de Lausanne (EPFL), 2014–2015 as a visiting professor at the University of Melbourne, and 2013 as the Debye Chair Professor at Utrecht University. Prof. Gamelin has received numerous honors for his work including most recently the 2015 ACS DIC Inorganic Lectureship Award, the Dunne Lectureship (Reed), the Sessler Distinguished Alumni Lectureship (Stanford), and the ACS DIC Inorganic Nanoscience Award. He is a Senior Fellow of the Zukunftskolleg at

the University of Konstanz, a Fellow of the American Association for the Advancement of Science (AAAS), a Scialog Fellow of Research Corporation, and a member of the Washington State Academy of Sciences. He is presently an Associate Editor for the Royal Society of Chemistry journal *Chemical Communications*.

## TOC Graphic

